UNIVERSITY OF SOUTHAMPTON

Experimental Study of Restrictor Noise in Ventilation Duct Systems

by

Fuyang Tao

A thesis submitted in partial fulfillment for the
degree of Doctor of Philosophy

in the
Faculty of Engineering and the Environment

July 2016

UNIVERSITY OF SOUTHAMPTON

ABSTRACT

FACULTY OF ENGINEERING AND THE ENVIRONMENT
Airbus Noise Technology Centre

Doctor of Philosophy

EXPERIMENTAL STUDY OF RESTRICTOR NOISE IN VENTILATION DUCT SYSTEMS

by Fuyang Tao

Single-hole restrictors are widely used in the aircraft air distribution system (ADS). The noise generated due to the flow passing over the restrictor is a main interior noise source of the cabin. Prediction of the restrictor noise generation is important for a quite ADS design.

This work experimentally and analytically studies the noise generation mechanisms of the single-hole restrictor. An experimental rig to investigate the restrictor self-noise and interaction noise generated by the turbulent wake produced by in-duct elements installed in the duct and impinging on the restrictor has been developed and constructed. Aeroacoustic measurements of the restrictor self-noise have been made both inside and in the far field of the duct. Two models have been developed to understand the restrictor noise generation mechanisms and predict the sound power level (PWL). One model is based on the surface pressure cross spectrum to compute the effective axial dipole distribution. The other is an extension of previous work and based on the static pressure drop across the restrictor. The restrictor dimension is shown to have a large effects on the restrictor noise generation.

For the interaction noise generation, the important parameters including mean flow speed, restrictor dimension, turbulence level and characteristic length, that determine the sound power radiation spectrum are studied. A semi-empirical model has been developed to predict the sound power spectrum due to interaction noise. The link between the interaction noise generation and the restrictor surface pressure has been investigated.

In addition to the investigation of the restrictor noise generation, this work conducted a short study into the use of surface roughness on the upstream side of the restrictor to reduce the noise generation whilst maintaining the pressure drop across it. It is shown that the noise generation can be reduced above the first cut-on frequency of the duct by increasing the upstream surface roughness.

Contents

List of Figures

List of Tables

Nomenclature

Roman

A	Cross-sectional area of the duct	$[m^2]$
a	Radius of circular duct	$[m]$
A_c	Correlation area	$[m^2]$
A_j	Open area of restrictor	$[m^2]$
A_r	Surface area restrictor	$[m^2]$
A_{fm}	Cross-sectional area of flare mouth	$[m^2]$
A_{ft}	Cross-sectional area of flare throat	$[m^2]$
A_{mn}	Amplitude of (m, n) mode in circular duct	$[Pa]$
A_m	Amplitude of m^{th} spinning mode	$[Pa]$
b_1, b_2	Side length of rectangular duct	$[m]$
B_n	Complex constant, n is a random number	
c_0	Sound speed in the air	[m/s]
C_d	Drag coefficient	
C_n	Constant	
C_{dis}	Restrictor discharge coefficient	
D	Duct internal diameter	$[m]$
d	Internal diameter of restrictor	$[m]$
F	Steady hydrodynamic force	$[N]$
f	Frequency	$[Hz]$
$\bar{f}$	Characteristic frequency of unsteady force	$[Hz]$

$\mathbf{f}$	Unsteady hydrodynamic force	$[N]$
F'	Perturbation of hydrodynamic force	$[N]$
f_τ	Constant	
f_{fc}	Cut-off frequency of flare	$[Hz]$
f_{mn}	Cut-off frequency of $(m,n)^{th}$ mode	$[Hz]$
G	Geometry factor of the noise generation due to restrictor	
h	Height of the restrictor	$[m]$
H_{xx}	Transfer function	
I	Sound intensity	$[W/m^2]$
J_m	Bessel function of order m	
j_{mn}	Root of Equation 3.11	
k	Wave number	$[m^{-1}]$
$K_m(f)$	Frequency dependent constant in the new model	
$K_G(f)$	Frequency dependent constant in Gordon's model	
$K_K(f)$	Frequency dependent constant in Karekulll's model	
$K_{mf}(f)$	Frequency dependent constant in momentum flux model	
$K_{NM}(St)$	Frequency dependent constant in Nelson and Morfey's model	
L	Separation distance between ring and restrictor	$[m]$
l	Separation distance between microphone	$[m]$
L_c	Characteristic length solid body	$[m]$
L_d	Length of entrance region of the duct	$[m]$
L_f	Length of flare	$[m]$
l_j	j^{th} Component of vector normal to fluid surface	
M	Mach number	
m	m^{th} spinning mode	
n	n^{th} radial mode	
N_{mn}	Normalization factor of the eigenfunctions of the duct	

P	Complex pressure	$[Pa]$
p	Pressure	$[Pa]$
P_i	Strength of dipole source	$[Pa]$
p_0	Amplitude of plane wave	$[Pa]$
p_{ij}	Compressive stress tensor	$[Pa]$
q	Dynamic pressure	$[Pa]$
q_c	Dynamic pressure corresponding to u_c	$[Pa]$
R_c	Complex reflection coefficient	
Re	Reynolds number	
S	Source surface area	$[m^2]$
S_{xx}	Auto spectrum	
S_{xy}	Cross spectrum	
St	Strouhal number	
St_c	Strouhal number correspoding to u_c	
T	Averaging time	$[s]$
t	Time	$[s]$
T_{ij}	Lighthill's stress tensor	$[Pa]$
Tu	Turbulence intensity	
U	Mean flow velocity in a duct	$[m/s]$
u	Velocity	$[m/s]$
u_c	Flow velocity at the centre of the duct	$[m/s]$
u_i	Flow velocity components	$[m/s]$
U_{vc}	Mean flow velocity in vena contracta	$[m/s]$
V	Volume of source	$[m^3]$
W	Acoustic power	$[N \cdot m/s]$
X	Streamwise distance from the restrictor	$[m]$
x_i	Observer Cartesian coordinate	$[m]$

X_R	Position of reattachment point	$[m]$
Y	Radial distance in cylindrical coordinate	$[m]$
y_i	Observer Cartesian coordinate	$[m]$

Greek

β	Restrictor diameter ratio	
θ	Azimuth in cylindrical coordinate	$[rad]$
ν	Kinematic viscosity	$[m^2/s]$
ρ	Density	$[kg/m^3]$
ρ_0	Ambient density	$[kg/m^3]$
σ	Vena contracta ration	
σ_{ij}	Viscous stress tensor	$[N \cdot m^{-2}]$
τ	Retarded time	$[s]$
ϕ_{uu}	Velocity spectrum of turbulence flow	$[m^2 s^{-1}]$
$\phi_{uu}^{A_r}$	Area-weighted velocity spectrum of turbulence flow	$[m^2 s^{-1}]$
Ψ_{mn}	Normalized eigenfunction of the duct	
ψ_{mn}	Eigenfunctions of duct	
ω	Angular frequency	$[rad/s]$

Subscripts

$_\theta$	Circumferential direction in cylindrical coordinate
$_m$	m^{th} spinning mode
$_n$	n^{th} radial mode
$_r$	Radial direction in cylindrical coordinate
$_z$	Axial direction in cylindrical coordinate
i	i^{th} Component in coordinate
j	j^{th} Component in coordinate

Superscripts

*	Complex conjugate

$+$	Downstream direction of the duct	
$-$	Upstream direction of the duct	

Acronyms

ADS	**A**ir **D**istribution **S**ystem	
CFD	**C**omputational **F**luid **D**ynamics	
CPSD	**C**ross **P**ower **S**pectral **D**ensity	
CTA	**C**onstant **T**emperature **A**nemometer	
OAPWL	**O**ver**A**ll sound **P**o**W**er **L**evel	[dB, ref:10^{-12}]
PIV	**P**article **I**mage **V**elocimetry	
PSD	**P**ower **S**pectral **D**ensity	
PWL	Sound **P**o**W**er **L**evel	[dB, ref:10^{-12}]

Declaration of authorship

I, FUYANG TAO, declare that the thesis entitled "Experimental Study of Restrictor Noise in Ventilation Duct Systems ", and the work presented in the thesis are both my own, and have been generated by me as the result of my own original research. I confirm that:

- This work was done wholly or mainly while in candidature for a research degree at this University;
- Where any part of this thesis has previously been submitted for a degree or any other qualification at this University or any other institution, this has been clearly stated;
- Where I have consulted the published work of others, this is always clearly attributed;
- Where I have quoted the work of others, the source is always given. With the exception of such quotations, this thesis is entirely my own work;
- I have acknowledged all main sources of help;
- Where the thesis is based on work done by myself jointly with others, I have made clear what was done by others and what I have contributed myself;
- Parts of this work have been published by the author in a conference paper [58].

Signed: ....
Date: ....

Acknowledgements

I would like to thank my supervisors Professor Phil Joseph and Professor Xin Zhang. Thank Professor Phil Joseph for his invaluable support and availability which were important for the completion of this work. His enthusiasm, encouragement and cheerful nature were greatly appreciated. It is a pleasure to run with him who is a good 'last-minute runner' and discuss 'EastEnders' with him. Thank Professor Xin Zhang for providing me this opportunity of study and the support in this project.

I would also like to thank Matthias Siercke for his support for this project. He also taught me a lot about the aircraft air distribution system. Thank support from Airbus.

I would like to thank Oksana Stalnov for her help in this project and teaching me to do experiments. I would also like to thank my colleagues in ANTC, Michael, Antoni, Meng, Jie, Fernando, Shuming, Yu, Ryu, James, Tim, Utsav, for all the nice times.

Thanks must also go to technicians, Chris Oliver, Simon Klitz, Steve White, Phil Oxborrow and Antony for their help on experimental facilities. Thank Chris and Steve for singing 'Fuyang' every time when they met me.

Finally, I would like to thank my parents and family, who give me endless support during all my studies.

Chapter 1

Introduction

1.1 Noise generation in an air distribution system

Passengers' growing demand for a comfortable aircraft cabin environment has become a major issue for many airlines. Continuous exposure to noise can make passengers uncomfortable [51], and even damage their health [55]. *The Control of Noise at Work Regulations 2005* [20] specifies a daily or weekly personal noise exposure limit of 87 dB (A-weighted). Thus, the acoustic performance of interior cabin is of significant concern.

The sources of aircraft cabin noise can be roughly divided into two parts: the noise transmitted from outside of the fuselage and the noise generated inside the cabin. The external noise sources includes the power plant and the turbulent boundary layer generated on the surface of the fuselage. External noise sources contribute most of the noise within the cabin [62]. However, internal noise sources within the cabin also contribute significantly and mainly includes flow-induced noise from the Air Distribution System (ADS). A part of the ADS is shown schematically in Figure 1.1. The air temperature and humidity is mixed in the mixing unit and is then transmitted through the ADS to reach the cabin through the air outlets. The ADS contains many in-duct elements. When the air passes through the in-duct elements, noise is generated. Though the noise from the ADS is smaller compared with the noise from the engine and the fuselage turbulent boundary layer, the noise from the ADS reaches the interior cabin through the air outlets directly and can also have impact on customer comfort. The sound pressure level due to the ADS alone at the passenger's chair position is about 63 dB (A-weighted) prior to take-off [50]. To produce a low noise ADS design, the engineer should include a noise analysis at the design stage. Thus, a fundamental understanding of the mechanism of the flow induced noise in the ADS is important for a quiet ADS design.

The ADS is composed of many in-duct elements. Noise is generated when flow passes through these in-duct elements. The restrictor is one of these in-duct elements widely used to control the flow rate at the different air outlets. A single hole restrictor is shown schematically in Figure 1.2. The noise generated by the restrictor is one of the main

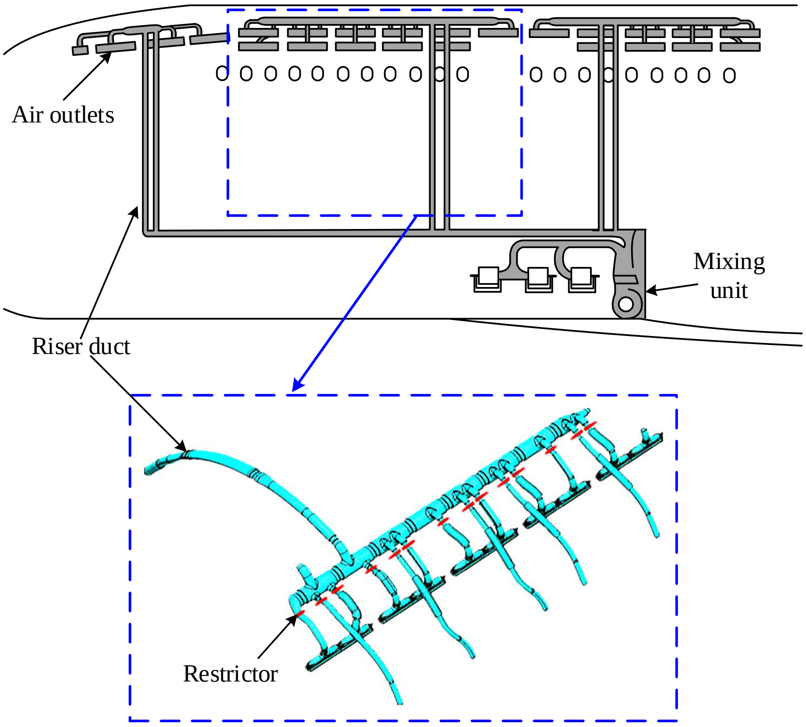

FIGURE 1.1: A schematic of a part of the air distribution system [24].

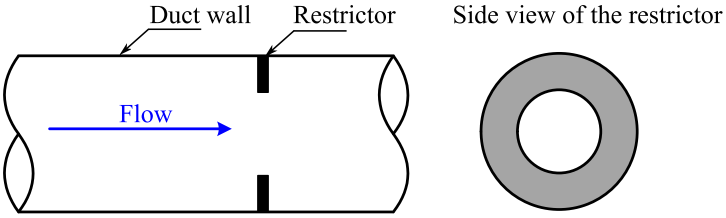

FIGURE 1.2: A schematic of a single-hole restrictor.

noise source in the ADS. Quite often another in-duct element is introduced upstream of the restrictor, such as a measuring device or a curved duct section. The turbulent wakes from these upstream elements will interact with the downstream restrictor to generate broadband interaction noise. Whilst restrictors are widely used in the duct system, the noise generation mechanisms of the restrictor is not well understood, particularly interaction noise generation. To realize a quiet ADS design, therefore, the interaction noise generation mechanisms by the restrictor should also be investigated.

1.2 Aims of the current work

This work aims to improve the current understanding of restrictor noise and provide simple models to predict it. The work focuses on both the self-noise from the restrictor and the noise due to interaction between the restrictor and the turbulent wake from an upstream in-duct element.

To understand the restrictor self-noise, aerodynamic and aeroacoustic measurements were performed to determine the characteristics of the restrictor self-noise. This information is then used to determine the mechanisms of noise generation by the restrictor. Insight into the generation mechanisms then lead to the development of a simple model for self-noise prediction for use in industry.

Similarly, noise due to the interaction between an upstream turbulent wake and the restrictor was studied by making detailed aerodynamic and aeroacoustic measurements in the duct. Based on these measurements a model for the prediction of the interaction noise was developed by making a comprehensive and fundamental parameter study of the effects of turbulence wake intensity and restrictor dimensions.

In addition to the investigation of both self-noise and interaction noise generation, a brief study into methods to reduce the noise but maintain pressure loss was conducted. Suggestions for restrictor noise reductions are proposed and verified experimentally.

1.3 Original contributions

The original contributions of this thesis are listed below:

- An experimental facility has been developed to investigate the restrictor noise. This facility was used to obtain detailed aerodynamic and aeroacoutic properties of the restrictor. Restrictor self-noise and the noise due to the interaction with incoming turbulence has been investigated in detail using this rig.

- The effects of the restrictor on the flow field in the duct have been investigated. The aerodynamic properties of the restrictor have been obtained, which provide useful information for the design of low-noise aircraft ADS.

- A general analytic model has been developed that is valid for the prediction of both restrictor self-noise and interaction noise based on measurements of the restrictor surface pressure distribution. This model demonstrates that the noise in the duct due to the restrictor originates from fluctuations of the restrictor surface pressure. Based on these surface pressure measurements, the noise source distribution over the restrictor surface has been determined.

- It has been shown experimentally that the surface pressure follows a U^4 velocity scaling law. Together with the U^6 velocity scaling law for the radiated noise power, it is inferred that the area over which the surface pressure is correlated scales with U^2.

- Several existing models for the prediction of the sound power of in-duct elements based on static pressure drop were reviewed and their predictions compared against measurements. The assumptions in these models have been investigated.

- Based on the review above, a semi-empirical model for the prediction of the restrictor self-noise sound power has been developed. All the parameters in this model can be easily measured. This model has been used to deduce the effects on the noise generation due to the dimensions of the restrictor.
- A semi-empirical model for the prediction of the sound power generated by the interaction between a turbulent wake and a single hole restrictor has been developed based on a comprehensive parameter study. The parameter study has allowed the effects of the important parameters on interaction noise generation to be investigated.
- A noise reduction method for the restrictor noise has been developed and investigated and shown to provide noise reductions of a few decibels whilst maintaining pressure drop.

1.4 Thesis structure

The remainder of this chapter provides a literature review of the work relating to restrictor noise. The review includes analytical, experimental and numerical studies for the prediction of the self-noise due to various in-duct elements, including bluff bodies and spoilers, of which a restrictor is an example. This also includes an investigation into the properties of restrictor noise deduced in previous work.

Chapter 2 presents the design and evaluation of the experimental duct rig. A general description about the basic experimental setup is provided. The acoustic and aerodynamic properties of the test section have been measured to ensure it meet the requirements necessary for restrictor noise measurements.

Chapter 3 presents the in-duct measurements of the aerodynamic and aeroacoustic fields within the duct when a single-hole restrictor is introduced. First, the wall pressure spectrum in the empty duct is presented. The results show that the noise levels are generally very low. The effects of the single-hole restrictor on the flow field in the duct are then investigated. The aerodynamic properties of the flow field near the restrictor are obtained from static pressure measurements, mean flow velocity measurements and turbulence intensity measurements. The sound field measurements in the duct include the wall pressure spectrum, analysis of the modal pressure amplitudes and the transmitted and radiated acoustic powers. The effects of the restrictor dimensions and the mean flow speed on the sound field are investigated. A model of the in-duct sound field is developed based on the surface pressure cross spectral density.

Chapter 4 presents the semi-empirical model for the prediction of the restrictor self-noise sound power. Current models for restrictor self-noise sound power prediction are reviewed and tested against our experimental results. The important parameters in these models are discussed. Based on this model, the impact of the restrictor dimensions on the noise is assessed. In the last section of this chapter, a simple model for the prediction of the sound power in the plane wave frequency range is developed based on the experimental noise data.

Chapter 5 presents a study into the characteristics and behaviour of the noise due to the interaction between the restrictor and the turbulent flow induced by an upstream in-duct element. In this study we restrict the measurements to the turbulent wake produced by a ring, which has the advantage of producing axi-symmetric flow. Modal analysis and surface pressure measurements are performed to investigate the interaction noise generation mechanisms. A parameter study is conducted to assess the impact of the mean flow speed, restrictor dimensions, turbulence intensity on the interaction noise generation. Based on this parameter study, a semi-empirical model is developed to predict the interaction noise generation.

Chapter 6 builds upon the knowledge gained in previous chapters in order to reduce the restrictor noise. The surface pressure of the restrictor is changed by increasing the surface roughness of the restrictor. The mechanisms of the noise reduction are investigated through the surface pressure measurements.

Chapter 7 discusses key conclusions and suggests future areas of research.

1.5 Literature Review

Restrictors are widely used in the ADS of aircraft, as well as the ADS in building ventilation systems. In addition, orifice-plate flow meters [25] and valves [52] are other examples of bluff bodies and have similar noise generation characteristics to restrictors. Considerable effort has therefore been dedicated to investigate the aerodynamic and aeroacoustic properties of the restrictor, including analytical, experimental and numerical approaches. These approaches are discussed in this section.

1.5.1 Acoustic analogy

The fundamental theory of sound generation by unsteady flows is the acoustic analogy based on the theory due to Lighthill. Lighthill [36] re-arranged the exact equations of conservation of mass and momentum to produce a forced wave equation whose right hand side is the aerodynamic source terms. In a medium with negligible flow speed and without boundaries,

$$\frac{\partial^2 \rho}{\partial t^2} - c_0^2 \nabla^2 \rho = \frac{\partial^2 T_{ij}}{\partial x_i \partial x_j}, \tag{1.1}$$

where ρ is the density, c_0 is the velocity of sound in fluid at rest, $T_{ij} = \rho u_i u_j + (p - c_0^2 \rho) - \sigma_{ij}$ is the Lighthill stress tensor. The left hand side of Equation 1.1 represents the sound propagation in an idealised medium and the right hand side represents the equivalent sound sources. Using the free field Green's function of the wave equation, the solution of the inhomogeneous wave equation 1.1 for the unsteady density is

$$(\rho - \rho_0)(\mathbf{x}, t) = \frac{1}{4\pi c_0^2} \frac{\partial^2}{\partial x_i \partial x_j} \int_V \frac{T_{ij}(\mathbf{y}, t - |\mathbf{x} - \mathbf{y}|/c_0)}{|\mathbf{x} - \mathbf{y}|} d\mathbf{y}. \tag{1.2}$$

Lighthill's analogy is exact for the generation and propagation of aerodynamic sound in a free field. However, it neglects absorption, reflection, diffraction and scattering due to solid boundaries. It is therefore suitable for subsonic flows and ignores the presence of solid boundaries.

Curle [10] extended Lighthill's theory of aerodynamic sound to account for the influence of solid boundaries. His main conclusions were:

- The sound generated by the quadrupoles in Lighthill's theory is reflected and diffracted by the solid boundaries.
- The quadrupoles are no longer distributed over the whole space, but only throughout the region external to the solid boundaries. The boundaries introduce a distribution of dipoles.

It is therefore necessary to determine the influence of these solid boundaries on noise generation. As turbulence is generated as flow passing over the solid boundaries, unsteady surface forces are likely to make a significant contribution to the sound generation. Curle considered the sound produced by turbulence in the vicinity of a fixed surface. The resultant modification to the Lighthill's theory for the density fluctuations is as follows:

$$(\rho - \rho_0)(\mathbf{x}, t) = \frac{1}{4\pi c_0^2} \frac{\partial^2}{\partial x_i \partial x_j} \int\limits_V \frac{T_{ij}\left(\mathbf{y}, t - \frac{|\mathbf{x}-\mathbf{y}|}{c_0}\right)}{|\mathbf{x} - \mathbf{y}|} d\mathbf{y} - \frac{1}{4\pi c_0^2} \frac{\partial}{\partial x_i} \int\limits_S \frac{P_i\left(\mathbf{y}, t - \frac{|\mathbf{x}-\mathbf{y}|}{c_0}\right)}{|\mathbf{x} - \mathbf{y}|} dS(\mathbf{y}), \tag{1.3}$$

where $P_i = -l_j p_{ij}$, l_j is the j^{th} component of the vector normal to the fluid surface.

On the right-hand side of this equation, the first term represents a volume distribution of quadrupole sources and the second term represents a surface distribution of dipole sources. Solid boundary effects such as reflection and diffraction are accounted for by the surface dipole field distribution P_i. The sound field is therefore exactly that which would be generated in a hypothetical unbounded uniform medium at rest, acted on by quadrupole and dipoles. The quadrupole sources of strength T_{ij} has a volume distribution throughout the region external to the solid bodies. The dipoles whose strength is P_i has a surface distribution acting on the surfaces of the solid bodies.

Through dimensional analysis, Curle showed that the intensity of the radiated sound generated by the dipole source distribution at large distance x is of the form, $I \propto \rho U^6 c_0^{-3} L^2 x^{-2}$. Here U is the mean flow velocity, and L is the typical dimension of the solid body. Sound intensity is therefore predicted to be proportional to the sixth power of the flow velocity. Many researchers have observed this scaling law experimentally for industrial application and often forms the basis for approximately estimating the flow induced noise generated by various in-duct elements.

If the acoustic wavelength is much larger than the size of the source region, the source region is said to be acoustically compact. The retarded time variations within the source region can be neglected,

$$t - \frac{|\mathbf{x} - \mathbf{y}|}{c_0} \approx t - \frac{|\mathbf{x}|}{c_0}. \tag{1.4}$$

In the case of a compact rigid body immersed in a high Reynolds number flow, the dipole term in the far field approximation of Curle's equation is equivalent to an unsteady force that the body exerts on the surrounding fluid and therefore

$$(\rho - \rho_0)(\mathbf{x}, t) = \frac{1}{4\pi c_0^3} \frac{x_i}{|\mathbf{x}|^2} \frac{d\mathbf{f}}{dt}(t - \frac{|\mathbf{x}|}{c_0}), \tag{1.5}$$

where F_i is the instantaneous total force that the solid body exerts on the fluid.

Based on the acoustic analogy, many researchers have derived useful prediction methods for the flow induced noise in the ADS by making appropriate approximations. For example, Nelson and Morfey [47] modelled the acoustic source distribution due to an in-duct element by a distribution of dipole sources over the surface, following Curle's theory. This extension allowed the restrictor noise power to be predicted without the need to derive P_{ij} exactly. This approach will be discussed below in further detail.

1.5.2 Flow induced noise in a straight duct

The main noise source in a straight duct with fully developed flow is the turbulence induced on the duct wall. The noise forms the background noise in the duct with flow. The level of the noise is generally low compared to that produced by in-duct elements, and for this reason, there is only a small amount of literature dealing with this noise source in a hard-walled duct.

According to the author's knowledge, only one empirical model has been derived [26] based on experimental data to predict the overall overall sound power level (OAPWL) generated due to turbulent flow in a straight hard walled duct, which is of the form,

$$OAPWL = 7 + 50 \log_{10} U + 10 \log_{10} A, \tag{1.6}$$

where U is the mean flow velocity in m/s , and A is the cross-sectional area of the duct in m^2.

According to this equation, the flow induced noise is independent of the duct length since it is derived for fully developed flows, but only dependent on the cross-sectional area of the duct and the flow speed. This equation shows that the sound power level in an empty duct follows the U^5 power law. This empirical equation is simple with only two parameters and could be applied to obtain a rough estimate of sound generation in a straight duct.

1.5.3 Restrictor self-noise

This section discusses previous work aimed at predicting restrictor self-noise, including analytical, experimental and numerical approaches.

1.5.3.1 Analytical method

Based on the theory due to Lighthill, Davies and Ffowcs-Williams [11] estimated the sound generation due to a finite volume of turbulence in a straight, infinitely long, hard-walled duct with a square cross-section. They concluded that the sound field generated by large-scale turbulence, which is highly correlated across the cross section of the duct, was in the form of a plane wave since the contribution from higher order modes averaged to zero over the source region. Furthermore, they showed that the noise level varied with the sixth power of the flow velocity. For the sound field generated by small-scale turbulence, the noise level was shown to still increase with the sixth power of the flow velocity below the first cut-on frequency. This is because only the plane wave is present in this frequency range with all other modes being cut-off and hence decay exponentially with distance from the source region. Above the cut-on frequency, small-scale turbulence excites an increasing number of modes until in the high frequency limit where the number of modes excited is sufficiently high that the turbulence radiates in precisely the same way as it would in free space and hence the noise radiates sound power as the eighth power of the flow velocity. The velocity power law therefore differs below and above the first cut-on frequency of the duct. Davies and Ffowcs-Williams suggests that the confinement of the duct on the radiation of the quadrupole sound source only exists in the plane wave frequency range. It is shown in this thesis that, since the diameter of typical ADS ducts is small, the plane wave region corresponds to most of the important frequency range.

Based on the work of Davies and Ffowcs-Williams, Herpe and Crighton [22] derived the following equation for the acoustic power radiated in the plane wave frequency range by a region of turbulence with volume $V = L_c^3$,

$$W \propto \rho U^3 L_c^2 \left(\frac{UL_c}{\nu}\right)\left(\frac{U}{c_0}\right)^3,$$

This result predicts a U^7 scaling law for the variation of the acoustic power with mean flow speed. In this formula, $\rho U^3 L_c^2$ is related to the 'flow power' which is the mechanical power required to maintain the given flow, and $(U/c_0)^3$ is the acoustic efficiency factor found for this problem by Davies and Ffowcs-Williams [11], and UL_c/ν is the Reynolds number. The work of Davies and Ffowcs-Williams [11] and Herpe and Crighton [22] predicted different velocity scaling laws for sound power radiation due to turbulence in a duct. In Chapter 4 it is shown that for the case where an in-duct element is introduced into the duct, the velocity scaling law is lower than that predicted by a region of turbulence alone due to contribution of surface dipoles.

The effects of the duct on the sound power radiation by different in-duct sound source have also been investigated. As the sound propagates in the duct as a series of modes, the total sound power can be obtained from the summation of sound powers in each mode. Some researchers have investigated the sound power in individual mode. Morfey [42, 43] has investigated theoretically the sound generation in hard-walled ducts with flow. He studied the effects of different source types on noise generation. He concluded that the sound power radiated from a monopole source distribution is proportional to $(1 + M)^2$ for frequencies well above the first cut-off frequency. The corresponding factors for axial-dipole and axial-quadrupole source distributions are 1 and $(1 + M)^2$ respectively. Rice [54] has also studied the far-field sound radiation for a circular duct due to single mode and multi-mode sound field. He developed a method of determining the acoustic power produced by turbofan engines as a function of the mode cut-off ratio. By assuming an 'equal energy density per mode' and 'equal energy per mode' sound field, Joseph *et al.* [27] developed an approach to estimate the sound power from in-duct acoustic pressure measurements. A non-dimensional parameter was derived and computed that related the total sound power propagating towards the open end of a duct containing a uniform flow to the mean-squared pressure averaged over a duct cross-section. The dipole source was shown to be most affected by the flow speed in the duct. However, the Mach number of interest in the present work is sufficiently low that convection effects can be ignored ($M < 0.1$).

1.5.3.2 Previous models based on pressure drop across the restrictor

Early experimental work by Gordon [17, 18] was used by him to derive a semi-empirical model to predict the radiated sound power from an in-duct element installed within the duct. In Gordon's experiments the in-duct elements were installed close to, or at the end, of the duct. The effects of the duct on the sound power radiation were ignored. Different types of in-duct elements of different shapes, including a restrictor and spoiler,

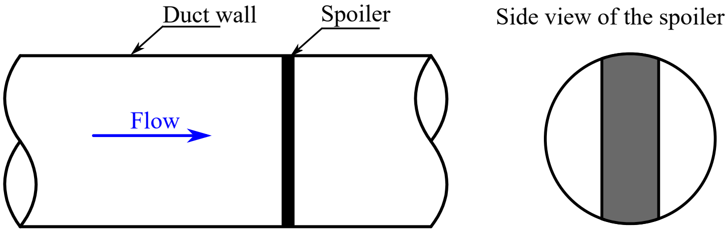

FIGURE 1.3: A schematic of a spoiler in the duct.

were investigated. The spoiler investigated by Gordon is shown schematically in Figure 1.3. In developing the prediction model Gordon assumed that the noise is generated by the pressure fluctuations on the surface of the in-duct elements. As it is difficult to measure the fluctuating forces acting on the in-duct element, Gordon assumed that these fluctuating forces were proportional to the steady force acting on the in-duct element. This assumption has been experimentally validated by Heller and Widnall [21]. Gordon based his theory on the expression derived by Ribner [53] for the sound power radiated by a compact dipole sound source in free field. This model was shown to predict the sound power to within 5 dB at frequencies corresponding to Strouhal numbers smaller than about 7. Above 7, the error is about 10 dB. In the calculation of the force acting on the in-duct element, the pressure downstream of the element was assumed to be the same as the atmospheric pressure due to the limited distance between the element and the end of the duct. However, this assumption is not sufficiently accurate for the current work in which the restrictor is always installed far away from the end of the duct.

By adopting a similar approach to Gordon, Nelson and Morfey [47] developed a model based on the acoustic analogy for the noise generation by the spoiler installed in a rectangular duct. The unsteady force distribution acting on the spoiler due to the turbulence induced by the spoiler was treated as a distribution of dipole sources, whose strength was assumed to be proportional to the unsteady state drag force acting on the spoiler. Unlike Gordon's work, the spoiler in Nelson and Morfey's work was installed in the duct far away from the end and so the effect of the duct on the noise radiation was therefore taken into consideration. They found that below the first cut-on frequency of the duct, only plane waves propagate and the radiated sound power follows a U^4 power law. Above the first cut-on frequency when higher order modes are excited, the radiated sound power follows a U^6 scaling law, suggesting that the dipole source in a duct radiated the same sound power as that in the free field. Nelson and Morfey also conducted measurements to verify their model. Measurements and predictions were shown to agree to within about 10 dB.

Nelson and Morfey's work has been widely extended by others to investigate the sound generation due to other types of in-duct elements with different geometries. Olaham and Ukpoho [48, 49, 61] attempted to extend the theory of Nelson and Morfey to obtain

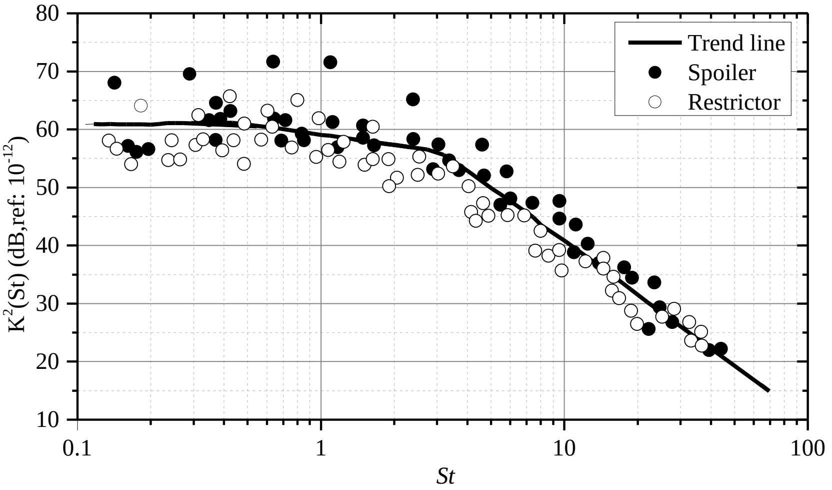

FIGURE 1.4: The ratio of fluctuating and steady state drag forces $K_{NM}(St)$ for the spoiler and the restrictor from measurements by Oldman and Ukpoho [48].

a general model for the prediction of the noise induced by difference in-duct elements. Olaham and Ukpoho assumed that the ratio between the fluctuating force and the steady force acting on the in-duct elements is the same for all in-duct elements, unlike Gordon who allowed this ratio to vary between different elements. Therefore, the aim of their work was to obtain this ratio by the proper selection of the open area ratio and the characteristic dimensions of the in-duct elements. The ratio of the fluctuating force and the steady force as a function of Strouhal number for a spoiler and a restrictor obtained experimentally by Olaham and Ukpoho is shown in Figure 1.4. It shows that the general behaviour of the ratio between the fluctuating and the steady state drag forces for the restrictor and the spoiler versus Strouhal number are similar. In the low Strouhal number range, the force ratio spectrum is flat. At Strouhal numbers higher than about 3, the frequency dependence follows a St^{-3} scaling law. However, the collapse is relatively poor. The difference between the data is about 15 dB. Figure 1.4 also shows that the spectra of the spoiler noise is generally 5 dB higher than that for the restrictor.

Similar to Oldham and Ukpoho, Mak [38] also attempted to obtain a generalized spectrum for different in-duct elements using numerical prediction methods. They numerically calculated the static pressure drop across the in-duct elements in Oldham and Ukpoho's prediction model. The spectra of the ratio between the fluctuating force and the steady force for a spoiler and a restrictor obtained numerically as shown in Figure 1.5 differs from the spectra shown in Figure 1.4. For Strouhal numbers below about 10, the results agree to within about 12 dB. As Strouhal numbers of about 10, the discrepancy is about 20 dB. In Mak and Au's results, the spectrum of the restrictor noise is generally higher than the spoiler noise which contradicts Oldham and Ukpoho's assumption. In addition, Mak's collapsed data is about 30 dB higher than the Oldham and Ukpoho's collapsed data. However, Mak did not provide the reason for this difference, but he concluded that it is not sufficient to predict the noise generation for different in-duct elements using a single normalized spectrum.

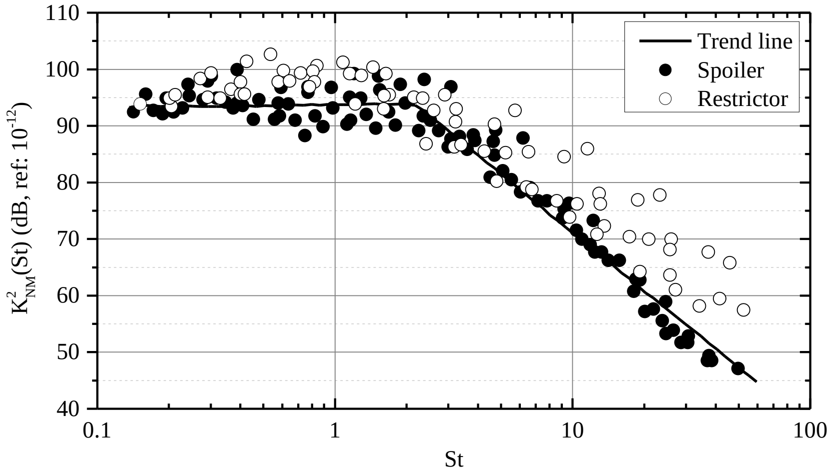

Figure 1.5: The ratio of fluctuating and steady state drag forces $K_{NM}(St)$ for the spoiler and the restrictor from numerical simulation by Mak [38].

Nelson and Morfey's model was revised by Kårekell *et al.* [33] to make it applicable to in-duct elements with more complex geometries. They provided a general definition of the Strouhal number in terms of the hydraulic diameter and pressure drop across the in-duct elements with complex geometries, so that the input parameters in Nelson and Morfey's model can be measured easily. The revised model was tested based on input parameters obtained from numerical predictions. The normalized spectra was found to collapse for different in-duct elements to within about 20 dB for Strouhal numbers below about 5. Above 5 the normalized spectra exhibits a variation of about 10 dB.

Kårekell *et al.* also revised Nelson and Morfey's model by calculating the steady force across the in-duct elements using the momentum flux [34]. The revised model was applied to the sound power prediction of a restrictor with small internal diameter. The smallest ratio of the internal diameter of the restrictor to the duct diameter in Karekell's experiments was 0.032. The normalized spectra was found to vary to within about 15 dB at low Strouhal numbers (<0.5) and to within 8 dB at higher Strouhal numbers (>0.5).

The models based on the pressure drop across the in-duct elements only contain parameters which can be measured easily. However, the accuracy of the models are not very satisfactory when compared against experimental noise data obtained in some previous work. It also shows that for different in-duct elements, a general normalized spectrum for the sound power prediction is not sufficient. Some of the models discussed above are used to try to collapse the measured data for the restrictor generated noise measured in our study presented in Chapter 4.

1.5.3.3 Wall-pressure measurements

For a fully developed duct flow with in-duct elements, the flow is highly turbulent downstream of the elements. In the vicinity of the in-duct element, the wall pressure is

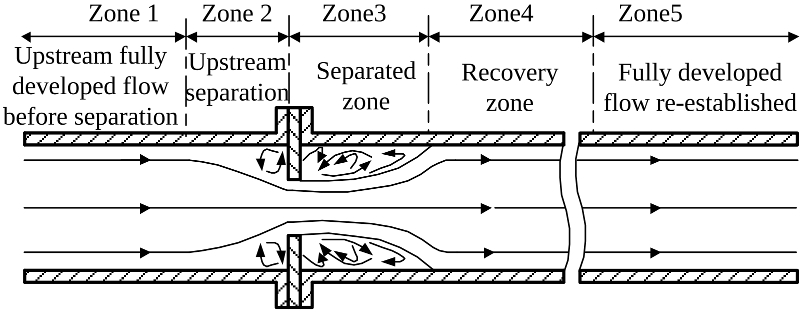

FIGURE 1.6: Different zones of flow in a duct with a single restrictor by Agarwal[5].

dominated by hydrodynamic fluctuations. Far enough downstream of the element the wall pressure is dominated by the acoustic pressure. The characteristics of the sound source can be obtained based on the measurements of the wall pressure spectra. Some of the previous work attempted to investigate the noise generation mechanisms of the in-duct elements by the variation in the measured wall pressure spectra.

Agarwal [2, 3, 4, 5, 6, 7] performed a series of studies to investigate the sound generation of a restrictor by analysis of the measured wall pressure spectra. Based on the different levels of the wall pressure fluctuations for a duct with a single hole restrictor, Agarwal [4, 5] divided the duct into 5 different flow regions, as shown in Figure 1.6. Due to its highest turbulence level, Agarwal concluded that the sound sources occur due to high levels of turbulence in the separation zone. To obtain the length of the separation zone, he measured the shear stress on the duct wall using a surface fence gauge to estimate the reattachment point in the duct[3, 6]. He concluded that the length of the source region is about ten times the height of the restrictor. This conclusion is similar to the work of other researchers [13, 14, 46]. These works also concluded that, as the Reynolds number increases, the length of the separation region and hence the size of the source region, decreases. In the separation region, Agarwal found that the wall pressure is dominated by hydrodynamic pressure fluctuations which are determined by the dynamic pressure of the flow in the centre of the restrictor. Through measurements of the wall pressure in the different zones, he concluded that in the separated flow region, pressure fluctuations were dominated by turbulent flow or non-propagating acoustic modes, or both.

Agarwal argued that in the recovering region, the acoustic pressure dominates. He also argued that both radial modes and circumferential modes are excited above the cut-on frequencies [2, 7] and not just axi-symmetric modes that would be excited by purely axi-symmetric excitation. Agarwal gave detailed results of the wall pressure measurements, which showed both broadband and narrow band characteristics. He also studied mode attenuation in the duct. However, as his work was mainly to investigate wall vibrations induced by the flow passing the restrictor, measurements and analysis of the sound power prediction by the restrictor noise was outside of the scope of his work.

Kerschen and Johnston investigated experimentally the properties of restrictor noise generation based on modal analysis of the sound field in the duct. According to the theoretical mode shape functions the amplitudes of the circumferential modes were determined from weighted combinations of the instantaneous outputs of the microphones spaced around the circumference of the duct [29, 30]. The sound power carried by each mode was also calculated [31]. They found the modal pressure spectra was determined by the ratio between the Helmholtz number (ka based on duct radius a, k is the wave number) and the Strouhal number (fL_c/U based on the characteristic dimension L_c of the restrictor), which govern acoustic modal propagation and the velocity spectral shape, respectively. When this ratio is small, the modal pressure spectra fall off rapidly with increasing frequency. When the ratio is large, the amplitude of each mode is approximately equal. Kerschen and Johnston [31] also concluded that the restrictor noise is generated by the jet flow. The higher order modes were assumed to be excited by the coherent flow structures near the jet flow.

1.5.3.4 Semi-empirical method

The radiated sound power from the restrictor follows velocity scaling law. The overall sound power level (OAPWL) of the restrictor noise can be calculated from [24]

$$OAPWL = C_2 \cdot \log_{10} U + C_3, \tag{1.7}$$

where U is the mean flow velocity in the duct and C_2 and C_3 are constants that need to be obtained from noise measurements.

The sound power in a frequency band also follows the velocity scaling law, Equation 1.7 therefore can also be applied for the prediction of the sound power in a frequency band, where now the constants are frequency dependent.

The semi-empirical method allows a quick estimation of flow induced noise by restrictors. However, this method cannot explain the mechanisms of sound generation by the restrictor.

1.5.3.5 Numerical methods

The growth in computer power has allowed computational aeroacoustics methods to be used to predict restrictor noise generation. Compared with experimental methods, numerical methods are more economical, and can provide detailed information about the flow field. The basic difficulties for aeroacoustic calculations are the huge disparities between the energy in the flow field and in the sound field, as well as the large length scale differences between the turbulent eddy scale and the wave length of the generated noise. Therefore, hybrid methods are often applied to aeroacoustic calculations, which do not directly compute the radiated noise in a simulation. Instead, the flow field is initially simulated and then used as an input into a second calculation to obtain the noise prediction. Compared to the direct numerical simulation, hybrid methods provide a compromise between the accuracy and the computational expense in the aeroacoustic calculation. Both hybrid methods and direct numerical simulations have been applied to the investigation of restrictor noise generation. In this section, previous numerical work on the noise generation by single in-duct element is reviewed. Much numerical work focuses on the validation of the numerical scheme. As the numerical work is out of the scope of the current work, this review of numerical methods will only focus on the physical explanation of restrictor noise provided by the previous numerical work.

Compared to experimental and analytical studies, there are fewer numerical studies which aim to investigate the noise generation by single in-duct element. Furthermore, these studies have often concentrated on the validation of the numerical scheme, other than the noise generation mechanisms. Gloerfelt and Lafon [15] simulated the noise generation by a restrictor installed in a rectangular duct. To take sound-flow interaction into consideration, the direct numerical simulation was adopted in their work. They concluded that the noise source arises from the turbulence flow downstream of the restrictor. The breakdown of the coherent jet-column structure was found to contribute the most energy to the sound field. The smaller scales of turbulence were found to be responsible for the broadband noise generation.

Spangenberg [57] also investigated numerically the noise generation by a single-hole restrictor. The wall pressure spectra from his simulation results match the experimental results within about 3 dB, but the difference in the static pressure drop between the experimental results and the simulation results differed by about 16.5%. For the flow field downstream of the restrictor, Spangenberg observed that the velocity fluctuations are similar in each direction. Another numerical study into noise generation from single restrictors was conducted by Mak [38] which has been discussed in Section 1.5.3.2.

1.5.3.6 Whistling due to the single-hole restrictor

Under certain flow regimes, when a sharp edge restrictor is installed in a duct, whistling occurs due to the instability of the shear flow downstream of the restrictor and the hydrodynamic or acoustic feedback from the end of the duct. The whistling phenomenon has been studied by previous researchers [32, 35, 59]. The occurrence of whistling is quite occasional [59], and in this thesis, focus was on the prediction of the broadband noise. Therefore, no work has been done on restrictor whistling in this thesis.

1.5.3.7 Summary of previous work on single restrictor noise generation

All the previous work described above shows that restrictor self-noise follows a velocity scaling law but do not agree on the exponent of this velocity power law. The previous work disagrees about the origin of the noise source for an in-duct restrictor. Some of the previous work concluded that the restrictor surface pressure fluctuations are the dominant noise source while the rest concluded that the noise source occurs in the turbulence flow downstream of the restrictor. A few semi-empirical models were developed for the prediction of the sound power due to restrictors based on the pressure drop across it. The accuracy of these models is tested in Chapter 4 by comparing against carefully conducted noise measurements presented in this thesis.

1.5.4 Interaction noise generation

1.5.4.1 Previous studies on interaction noise generation

When an in-duct element is introduced upstream of the restrictor, such as a measuring device or a duct bend, the turbulent wake from the upstream element will interact with the restrictor to generate broadband interaction noise. Quite often the interaction noise is dominant. In this section, the previous work on interaction noise generation between upstream turbulence and the restrictor is reviewed.

There have been some attempts to extend Nelson and Morfey's [47] work to predict interaction noise generation. Mak [39] developed a model based on the work of Nelson and Morfey [47] for the prediction of sound generated by two tandem elements, taking interaction noise generation into account, in a low speed duct. To account for interaction noise they introduced an additional term to Nelson and Morfey's model in which the sound source is assumed to be the surface pressure fluctuations acting on the in-duct element. Mak formulated the interaction noise in terms of the cross spectra between the surface pressure fluctuations on the two elements. The model proposed by Mak was tested against the measured data [37]. The separation distances between the two spoilers were 1.5 m and 3 m. The sound power level of total noise is about 6 dB higher than the self-noise due to the interaction noise when the separation distance was 3 m. When the separation distance was reduced to 1.5 mm, the interaction noise generation is about 2 dB lower than that for the 3 m separation distance. Mak's model was found to underestimate the interaction noise generation by about 3 dB. The problem in Mak's model is that the phase difference between the assumed sound sources is difficult to obtain. Note that in the work presented in this thesis interaction noise was shown to reduce quite quickly as separation distance was increased.

Similar to Mak's work, Han *et al.* [19] developed a model to predict the noise generation by two tandem in-duct elements by adding an additional term to Nelson and Morfey's model [47]. Han assumed that interaction noise generation is determined by the effective volume of the turbulence region generated by each in-duct element and the velocity correlation between the two effective areas. These two parameters were estimated from Ukpoho and Oldham's experimental results [60] as it is difficult to measure these two parameters. Han's model was shown to match the experimental results of Ukpoho and Oldham [60] to within 1 dB. The effective volume of the turbulence region generated by each in-duct element and the velocity correlation between the two effective areas required for the calculation of the interaction noise is also difficult to measure and may depend on the geometry of the in-duct elements.

Belanger *et al.* [8], Mendonca *et al.* [41], Mathey *et al.* [40], Sengissen *et al.* [56] and Karban *et al.* [28] all investigated numerically interaction noise generation by two tandem restrictors using different numerical schemes. The duct setup were the same in all these studies. The separation distances between the two restrictors were either one duct diameter or two duct diameters. The wall pressure spectra obtained from the simulation near the restrictor were all compared with that from the experimental results to verify the validity of the numerical schemes. Belanger *et al.* and Mathey *et al.* and Karban *et al.* suggested that restrictor self-noise is mainly generated by the vortices formed when the flow passes through the restrictor, and they concluded that interaction noise is generated due to the vortices from the upstream restrictor impinging on the downstream restrictor. In Mendonca *et al.*'s work, the sound source is assumed to be located in the shear layer downstream of the restrictor. Sengissen *et al.* concluded that the properties of the interaction noise is related to the length scale of the eddies impinging on the downstream restrictor.

1.5.4.2 Summary of previous studies on interaction noise generation

Some work has been done on the mechanisms and prediction of interaction noise generation. However, not too many conclusions were drawn about the characteristics and mechanisms of noise generation. It is clear that the interaction noise is generated by the turbulence flow from the upstream in-duct element impinging on the downstream in-duct element, but the link between the characteristics of the flow and the interaction noise generation has not been made clear, which is one of the objectives of this thesis. There is a lack of systematic experimental data relating to in-duct interaction noise generation. The effect on the interaction noise generation due to the mean flow speed, separation distance, element dimension has so far not been carefully studied.

Chapter 2

Fabrication and evaluation of the experimental facility

2.1 Introduction

This chapter describes the design, fabrication and calibration of the experimental rig for the measurements of the noise from single-hole restrictors. An overview of the experimental facility is presented. The chapter describes the measurements of the important acoustic and aerodynamic parameters. All measurements presented in this thesis, which are described in detail in subsequent chapters, are performed using this rig.

2.2 Overview of the experimental facility

The experimental rig is designed to study the aerodynamic and aeroacoustic properties of single-hole restrictors installed in the ADS. Figure 2.1(a) and (b) are a schematic and photograph of the experimental rig. The basic rig comprises a long acrylic duct with a centrifugal fan located at one end to deliver flow speeds typical of that in the ADS. The other end is located within a small anechoic room for the purpose of measuring the radiated acoustic pressure.

The rig was designed with three basic acoustic criteria in mind. The first requirement is standing waves in the working section should be eliminated to simulate an infinitely long duct. To this end, a silencer was installed at the upstream end and an exponential flare was installed at the downstream end of the duct to avoid the reflection from both ends. The second requirement is that the noise and vibration induced by the centrifugal fan and flow meter upstream of the test section should be prevented from reaching the working section. A flexible tube was therefore installed downstream of the fan to isolate the vibration due to the operation of the fan. The effectiveness of the silencer installed downstream of the flow meter was tested to ensure that the noise generated

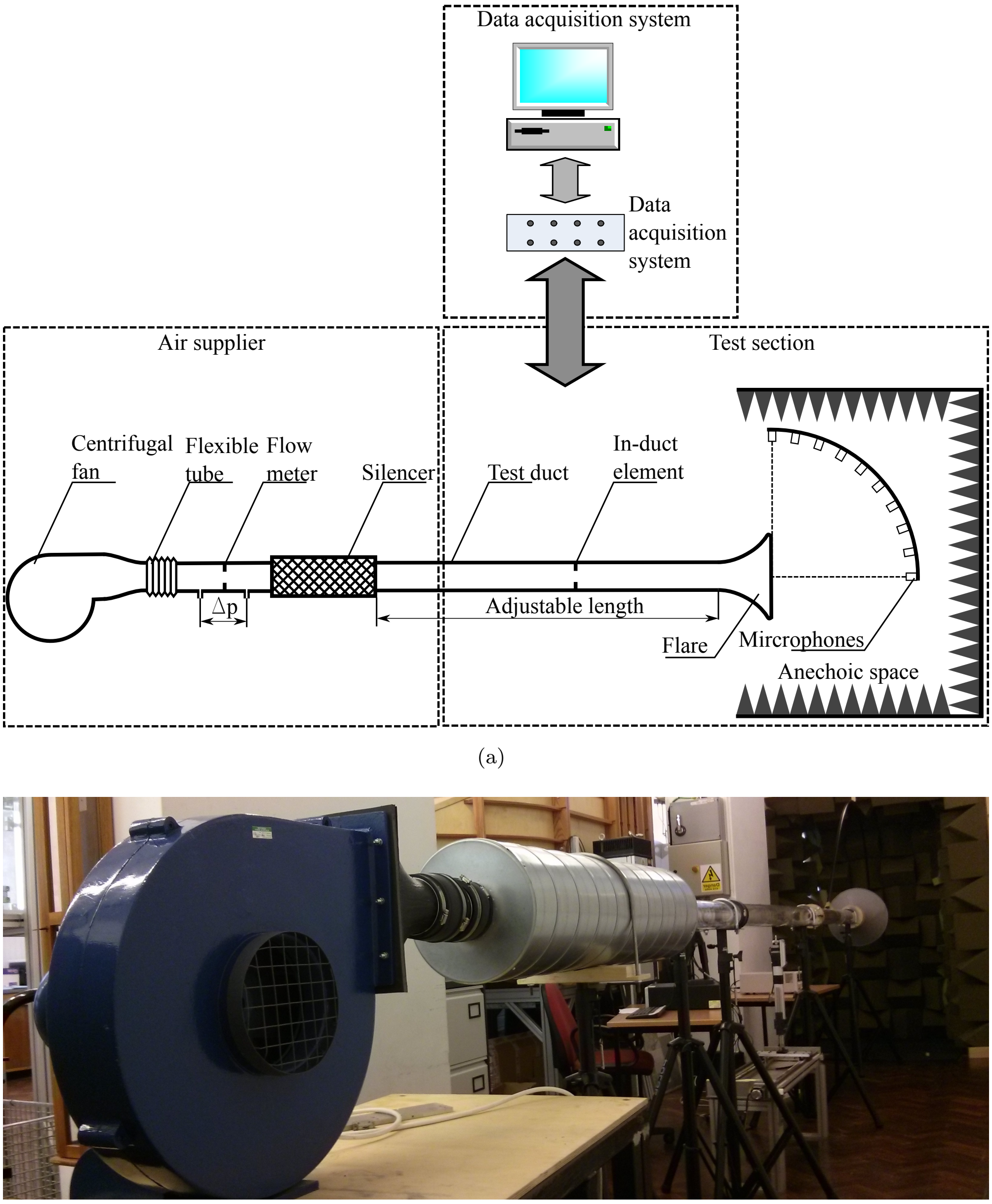

(a)

(b)

FIGURE 2.1: (a)A schematic of the experimental rig, (b)photograph of the experimental rig.

by the fan and the flow meter is sufficiently well absorbed. The last requirement is that the reflections from the end of the duct should be minimised so that the sound power transmitted along the duct equals the sound power radiated to the far field. This was achieved by the use of an exponential flare installed at the end of the duct to smooth the transition between the in-duct geometry and the far field.

In the ADS, the diameters of commonly used duct ranges between 70 mm and 225 mm [24] and the maximum mean flow speed is 25 m/s. The duct diameter selected in previous work by other researchers was 100 mm which is typically used in the ADS[57]. For the convenience of the comparison with the results in previous work, the internal

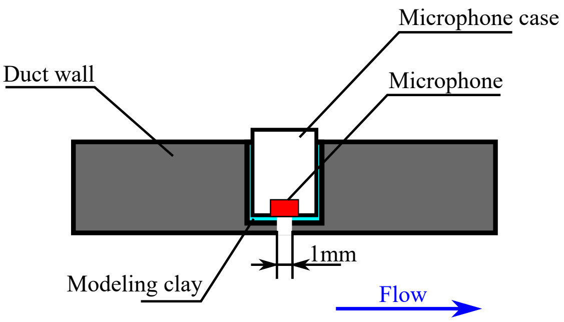

Figure 2.2: A schematic of the microphone flush-mounted on the duct for the wall pressure measurements.

diameter of experimental rig was set to 100 mm. The cylindrical duct was constructed from acrylic, and a wall thickness of 5.14 mm. The length of duct was constructed from a number of smaller sections of varying length connected together with flanges. This arrangement allows the overall length of the duct to be adjusted. The mean flow speed in the duct is determined by the fan speed and the in-duct elements. In the current work the range of mean flow speeds in the duct was between 10 m/s and 25 m/s. An orifice plate flow meter was installed upstream of the silencer for the measurement of the mean flow speed in the duct. The noise generated by the flow meter is absorbed by the silencer whose performance is presented below. The distance between the flow meter and the test section was arranged to be long enough to ensure that the flow in the test section was fully developed in the test section. The properties of the flow in the test section are reported below.

Acoustic measurements were performed both inside and outside of the duct. For the in-duct acoustic measurements, the microphones were mounted at the duct wall as shown in Figure 2.2 for the wall pressure measurements. A small hole with a diameter of 1 mm was drilled on the duct wall for the wall pressure measurement to reduce the effects of the hole on the flow in the duct. To ensure there is no leak between the microphone and the duct wall, the modeling clay was used to seal the gap between the microphone case and the duct wall. The sound power generated by the restrictor from the open end of the duct was measured by integrating the far field intensity over a hemi-sphere enclosing the duct opening, which is assumed to be axi-symmetric. Free-field conditions were obtained by constructing a small anechoic room from foam wedges at the end of the rig, as seen in Figure 2.1(a). From the length of the wedges the cut-off frequency of the anechoic room was estimated to about 250 Hz. The radiated noise, and hence sound power, was measured using a total of 10 microphones installed over an arc with 1 m diameter. The centre of the arc was located at the centre of the flare outlet.

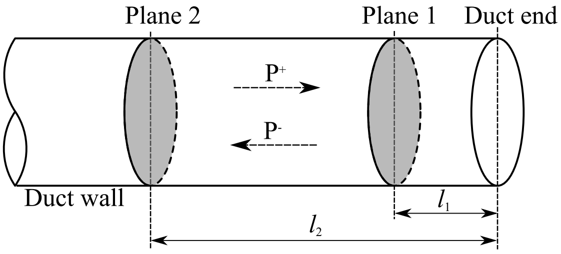

FIGURE 2.3: Duct end with flush mounted microphones for the reflection coefficient measurement using two microphone method.

2.3 Evaluation of experimental facility

2.3.1 Evaluation of the flare

Without a flare, sound from the restrictor would be reflected from the open end of the duct. To minimize this effect an exponential flare with a throat of 100 mm, a mouth of 500 mm and a length of 475 mm was installed at the end of the duct. In this section, the reflection coefficient of the flare installed at the end of the duct is evaluated using a two microphone method [23]. The theoretical cut-off frequency of the flare is first calculated above which the flare is effective in reducing reflections.

The theoretical cut-off frequency of the flare can be calculated from [12]

$$f_{fc} = \frac{c_0}{4\pi L_f} \ln \frac{A_{fm}}{A_{ft}}, \tag{2.1}$$

where c_0 is the speed of the sound, L_f is the length of the flare, A_{fm} is the area of the mouth, A_{ft} is the area of the throat. From Equation 2.1, the cut-off frequency of the flare used in current work is 186 Hz.

2.3.1.1 Background theory of complex reflection coefficient

A schematic of a duct termination for the complex reflection coefficient measurement is shown in Figure 2.3. The acoustic pressure was measured at two reference planes with the separation distance from the duct end of being l_1 and l_2 respectively. The complex amplitudes of the incident and reflected sound waves at the end of the duct are expressed as P^+ and P^- respectively from which the reflection coefficient at the duct end is given by

$$R_c = \frac{P^-}{P^+}, \tag{2.2}$$

where R_c is complex reflection coefficient which can be easily determined from the classical two-microphone method.

At a single frequency the acoustic pressure at any point in the duct may be expressed as the sum of the forward (to the outlet of the duct) and backward propagating wave components. The sound pressure at each measurement position p_1 and p_2 can be expressed in frequency domain as

$$p_1(\omega) = P^+ e^{-jkl_1} + P^- e^{jkl_1} \tag{2.3}$$

and

$$p_2(\omega) = P^+ e^{-jkl_2} + P^- e^{jkl_2}, \tag{2.4}$$

where k is the acoustic wave number. As there is no flow in the duct for the complex reflection coefficient measurement, the wave numbers in the forward and backward direction are the same.

The transfer function of the pressures at the two measurement positions can be calculated from

$$H_{12} = \frac{S_{p_1p_2}}{S_{p_2p_2}}, \tag{2.5}$$

where $S_{p_2p_2}$ is the auto-spectrum of the measured pressure at position 2

$$S_{p_2p_2} = \frac{\pi}{T} E\{(P^+ e^{-jkl_2} + P^- e^{jkl_2})(P^+ e^{-jkl_2} + P^- e^{jkl_2})^*\}, \tag{2.6}$$

and

$$S_{p_1p_2} = \frac{\pi}{T} E\{(P^+ e^{-jkl_1} + P^- e^{jkl_1})(P^+ e^{-jkl_2} + P^- e^{jkl_2})^*\} \tag{2.7}$$

is the cross-spectrum between the pressures at positions 1 and 2, and $E\{\}$ denotes expectation.

Substituting Equations 2.2, 2.6 and 2.7 into Equation 2.5 yields

$$H_{12} = \frac{e^{-jkl_1} + R_c e^{jkl_1}}{e^{-jkl_2} + R_c e^{jkl_2}}. \tag{2.8}$$

The complex reflection coefficient can therefore be expressed as

$$R_c = -\left\{ \frac{H_{12} e^{-jkl_2} - e^{-jkl_1}}{H_{12} e^{-jkl_2} - e^{jkl_1}} \right\}. \tag{2.9}$$

Hence, the complex reflection coefficient can be obtained based on the measurements of transfer function between the pressures at positions 1 and 2.

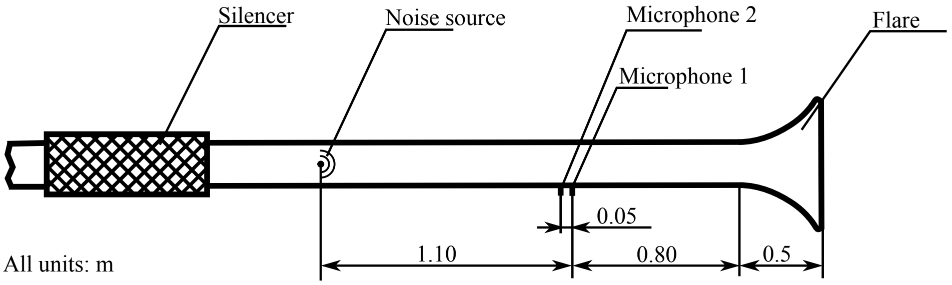

FIGURE 2.4: A schematic of the experimental arrangement for the reflection coefficient measurement.

According to the derivation of Equation 2.9, it is clear that this equation is only valid for the plane wave frequency range. If propagation losses are ignored, the two pressures are identical when $k(l_2 - l_1) = n\pi$, with n being an integer and hence poor results will be obtained if the separation distance between two measurement positions is close to multiples of half an acoustic wavelength. The separation distance between the measurement positions was therefore kept to less than a half wavelength at the highest frequency for which only plane waves can propagate, which is about 2010Hz.

2.3.1.2 Measurement of the complex reflection coefficient

In this section the measured reflection coefficient derived from Equation 2.9 is presented. The locations of the sound source and microphones positions within the duct rig for the reflection coefficient measurement is shown in Figure 2.4. The silencer was installed at one end of the duct to avoid reflections from this end. The flare was installed on the other end of the duct. A white noise sound source was installed near the silencer end at a distance of 1.2 m away from microphone 1. The distance between microphone 1 and the open end of the flare was 1.28 m. In the current rig, the first higher order mode is cut-on at 2010 Hz and the corresponding wavelength is 0.17 m. According to the discussion above the separation distance between the two microphones should be smaller than half of this distance, which is 0.085 m. The two microphones were flush mounted to the duct using the arrangement discussed above at a separation distance of 0.05 m. In order to investigate the effectiveness of the flare, the reflection coefficient is also measured without the flare.

The measured reflection coefficient magnitude is shown in Figure 2.5. Periodic humps appear on the curves due to the interference between the incident sound wave from the loudspeaker and the reflected sound wave from the duct end. Below the cut-off frequency of the flare, 186 Hz, the measured reflection coefficients with and without flare are similar. Above this frequency the reflection coefficient of the flare drops to below 0.1 but without the flare the reflection coefficient is greater than 0.5 up to about 1200 Hz. The flare is therefore very effective in reducing reflections from the open end at frequencies greater than 200 Hz.

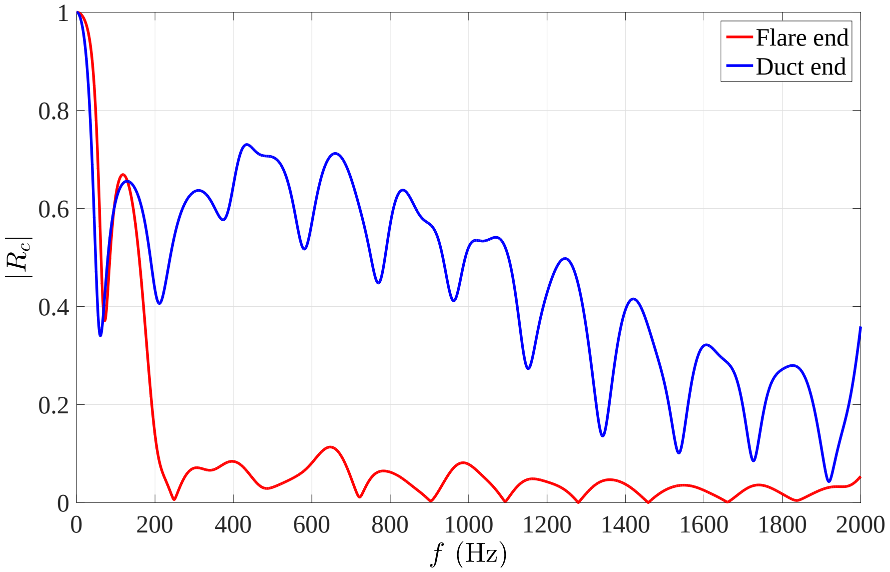

FIGURE 2.5: Comparison of the measured reflection coefficient magnitude $|R_c|$ with and without the flare at the duct end.

TABLE 2.1: Attenuation for centre frequency for SLGU 150 silencer[9]

Centre frequency, Hz	63	125	250	500	1000	2000	4000	8000
Attenuation, dB	10	26	36	48	50	50	45	24

2.3.2 Background noise measurement

In the absence of the restrictor, broadband noise is generated due to the operation of the fan. Noise is also generated when the flow passes over the flexible tube and through the orifice flow meter. To eliminate these noise sources, a silencer is installed upstream of the test section. The silencer used in this rig was made commercially by the company Lindab (model number SLGU 150). A table of the sound attenuation provided by the company in octave centre frequencies is shown in Table 2.1[9]. This section presents the measured acoustic performance of the silencer.

The power spectral density (PSD) and the coherence of the wall pressure in the test section with and without the silencer is measured to evaluate the silencer performance. When airflow is present in the duct, the pressure measured at the duct wall contains both aerodynamic and acoustic pressure fluctuations. If the aerodynamic pressure fluctuations exceed the acoustic contribution to overall pressure, there will be small difference between the two measured wall pressure PSD with and without the silencer since the noise originates from boundary layer fluctuations that are not affected by the silencer. It is therefore difficult to evaluate the performance of the silencer only by the measurement of the wall pressure PSD in this situation. Acoustic pressure fluctuations are coherent over a much larger distance than the turbulent pressure fluctuations, the coherence of the background noise with and without silencer is therefore also measured to evaluate

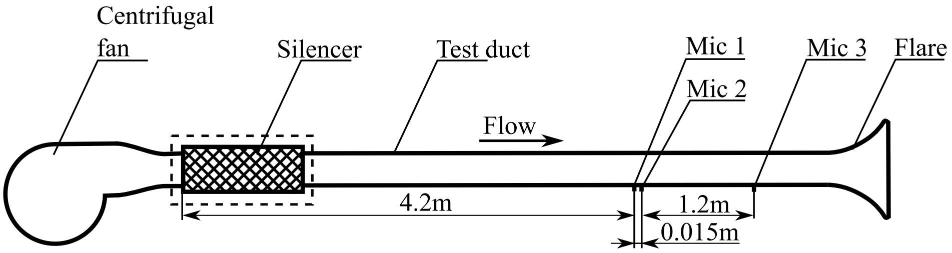

FIGURE 2.6: Experimental arrangement for the evaluation of the silencer (The silencer marked in dashed line was replaced by a duct with the same length for the measurement without the silencer).

the performance of the silencer.

The arrangement of microphones in the duct rig for the assessment of the silencer performance is shown in Figure 2.6. To ensure the same flow state in the test section for the noise measurement without silencer, the silencer (marked in the dashed line in Figure 2.6) was replaced by a duct of the same length. Three microphones are flush mounted on the duct wall. The separation distance between microphone 1 and the inlet of the silencer was 4.2 m. The separation distance between microphone 1 and microphone 2 was 1.5 cm, and the distance between microphone 2 and microphone 3 was 1.2 m. Two extreme test cases at the minimum mean flow speed of 10 m/s and maximum mean flow speed of 25 m/s were selected to make the background noise measurements.

A comparison of the wall pressure PSD in the test section measured by microphone 1 at the minimum and the maximum mean flow speed, with and without silencer, is shown in Figure 2.7. The window size of the Fourier transform is 1024 samples, and the number of the Fourier transform is also 1024 samples, leading to the frequency resolution of 19.5 Hz. The settings of Fourier transform are the same in this thesis. At the mean flow speed of 10 m/s, the wall pressure without silencer is higher than that with silencer in the frequency range below 1000 Hz and above 4000 Hz. In the frequency range between 1000 Hz and 4000 Hz, the wall pressure without silencer is only slightly higher than that with silencer. More information can be obtained from the corresponding coherence measurement which is shown in Figures 2.8. For the case without silencer, the wall pressure is highly coherent in the frequency range below 1000 Hz and above 4000 Hz, even for the measured positions at 1.2 m separation distance. For the case with the silencer, the wall pressure is only coherent below 1000 Hz when the two measured positions are separated by 1.5 cm. The wall pressure coherence is poor at all frequencies when the two measurement positions are separated by 1.2 m. The results of the PSD and coherence measurements suggest that the noise generated by the fan, flexible tube and flow meter is dominant below 1000 Hz and above 4000 Hz at the mean flow speed of 10 m/s, and this noise can be effectively eliminated by the silencer.

At the maximum mean flow speed the wall pressure without silencer is higher than the case with the silencer in the frequency range below 2000 Hz. Above 2000 Hz, the wall pressure is the same for the two cases. Considering the coherence shown in Figure 2.9,

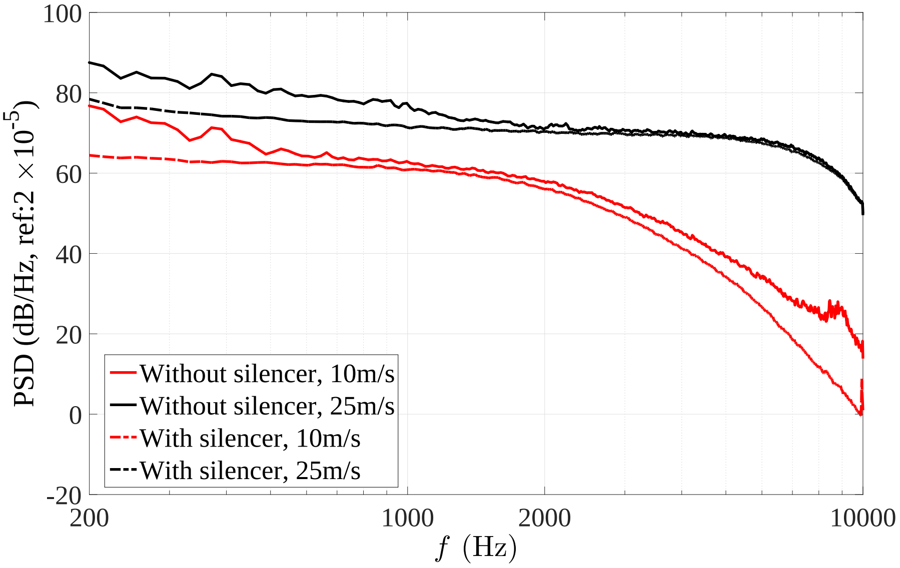

FIGURE 2.7: Comparison of the wall pressure PSD in the test section with and without the silencer installation under mean flow speeds of 10 m/s and 25 m/s.

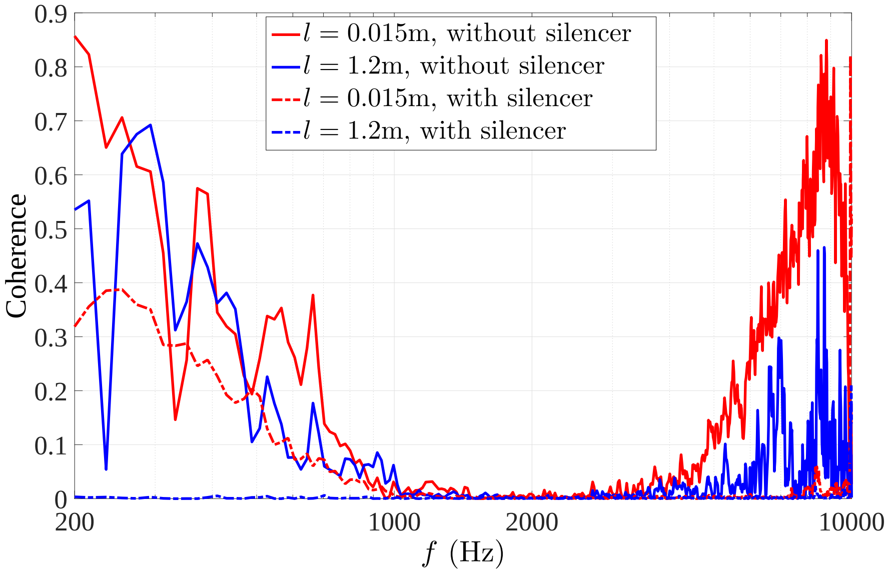

FIGURE 2.8: Comparison of the wall pressure coherence in the test section with and without the silencer installation under a mean flow speed of 10 m/s. The axial separation distances of the microphones l are 0.015 m and 1.2 m

it can be concluded that the acoustic field dominates below 2000 Hz, and hydrodynamic pressure fluctuations dominate above 2000 Hz. The acoustic noise can also be eliminated by the silencer.

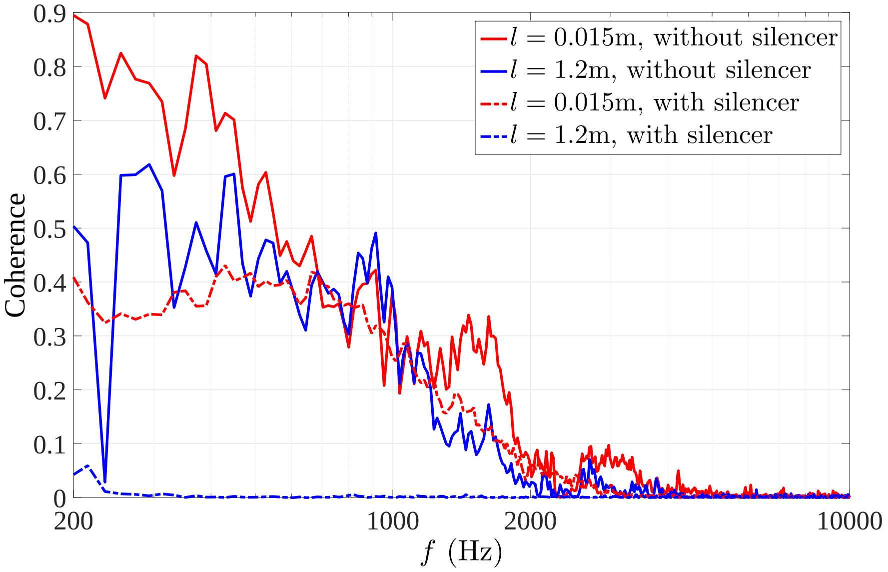

FIGURE 2.9: Comparison of the wall pressure coherence in the test section with and without the silencer installation under a mean flow speed of 25 m/s. The axial separation distances of the microphones l are 0.015 m and 1.2 m

2.3.3 Properties of the flow in the test section

Different flow states in the test section may have an effect on the noise generation of in-duct elements. To ensure the same flow state in the test section, the flow in this region should be fully developed. In this section, the mean flow velocity profiles in the test section at different streamwise locations are measured to confirm that the flow in the test section is fully developed.

2.3.3.1 Mean flow velocity profile measurement

The region near the inlet where the flow enters the pipe is defined as the entrance region, shown in Figure 2.10 [45]. As the flow moves through the pipe, viscous effects cause a boundary layer to form on the duct wall. Thus, in the entrance region, the velocity profile of the flow changes with streamwise location as the boundary layer develops along the duct wall. The point at which the boundary layer grows in thickness such that it ‘completely fills the pipe’, the flow is regarded as fully developed. When a flow is fully developed, all mean flow quantities are independent of the streamwise location. Typical entrance lengths L_d for turbulent flow in a pipe are roughly given by [45]

$$\frac{L_d}{D} = 4.4Re^{1/6}, \tag{2.10}$$

where D is the internal diameter of the duct and Re is the Reynolds number based on the duct diameter. According to Equation 2.10, the length of the entrance region for different mean flow speeds in this duct rig at 20^oC is shown in Table 2.2.

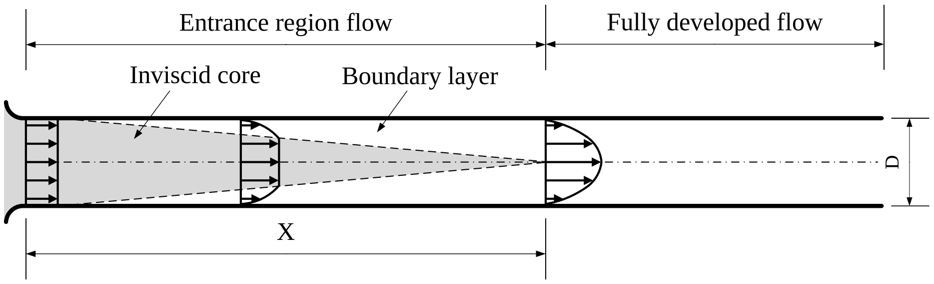

FIGURE 2.10: Development of turbulent flow in a duct[45].

TABLE 2.2: Length of entrance region calculation for the duct in this work

Flow speed (m/s)	Reynolds number	L_d/D
10	72102	28.39
15	108153	30.37
20	144204	31.86
25	180254	33.07

The experimental arrangement for the measurement of the mean flow velocity profile is shown in Figure 2.11. The flow speeds at different positions in the radial direction were measured using a Pitot tube, which was traversed automatically. The total length of the duct section was 6 m, which is 60 times the internal diameter of the duct. According to Table 2.2, two extreme positions, $l = 15D$ and $l = 59D$ were selected for the measurement, where l is the streamwise separation distance from the duct inlet to the measurement position of the pitot tube. According to theory, the flow at $l = 15D$ represents the developing flow and the flow at $l = 59D$ represents the developed flow. For measurement convenience the streamwise location $l = 39D$ was selected for the installation of the in-duct elements. The mean flow velocity profile was therefore measured at this location. In the radial direction the pitot tube was traversed for 75 steps with a step size of 1.25 mm starting from 2.5 mm from the wall of the duct. The total traverse distance along the radial direction was 93.75 mm. Due to the size of the pitot tube, the flow velocity near the wall cannot be measured. Measurements of the mean flow velocity profiles at a mean flow speed of 25 m/s are shown in Figure 2.12. All velocities are normalized using the streamwise velocity at the centre line. The profile at $39D$ is similar to that at $59D$, suggesting that the flow at $39D$ is fully developed. Thus, the test section will be placed a distance of $39D$ downstream of the inlet of the duct to ensure a fully developed flow in the test section.

2.3.3.2 Turbulence intensity measurement

In this section the velocity spectra and the turbulence intensity in the test section is measured using constant temperature anemometry (CTA). The streamwise location of the hot-wire probe for the measurement of the turbulence intensity is similar to that for

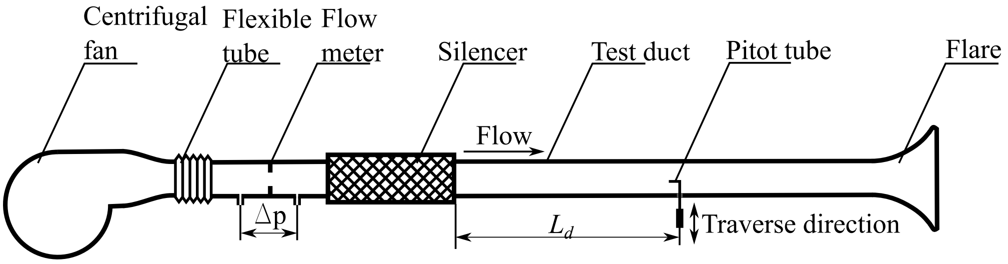

FIGURE 2.11: Experimental arrangement for the mean flow velocity profile measurement in the test section.

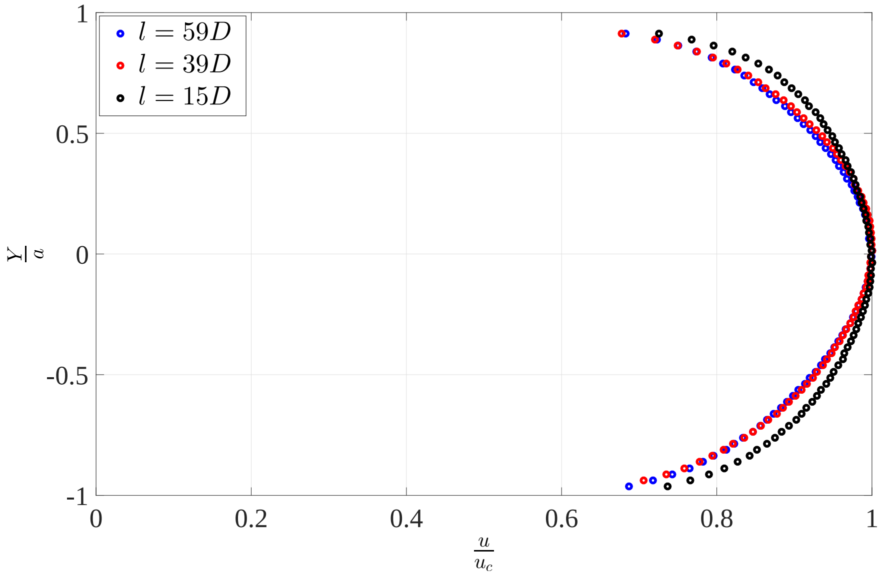

FIGURE 2.12: Mean flow velocity profile at $l = 15D$, $39D$ and $59D$ under a mean flow speed of 25 m/s. The velocity u has been normalized by the centre velocity u_c and the radial position Y has been normalized by the duct radius a.

the measure flow profile measurement as shown in Figure 2.11, in which the pitot tube was replaced by a single wire hot-wire probe. The hot-wire probe in this test was also traversed automatically along the radial direction in 16 equal steps of 6.25 mm. The distance covered was 96 mm starting at 2.5mm, stopping at a distance 1.5 mm from the wall on the other side. The mean flow speed in the duct was 10.0 m/s.

The measured velocity spectra at different radial positions are plotted in Figure 2.13. The highest velocity fluctuations are observed to occur near the duct wall due to the boundary layer. The highest velocity PSD near the duct wall is about 7 dB higher than the lowest PSD at the centre line.

The variation of the turbulence intensity Tu along the radial direction is show in Figure 2.14. The turbulence intensity is defined as

$$Tu(r) = \frac{u_{rms}(r)}{u(r)}, \tag{2.11}$$

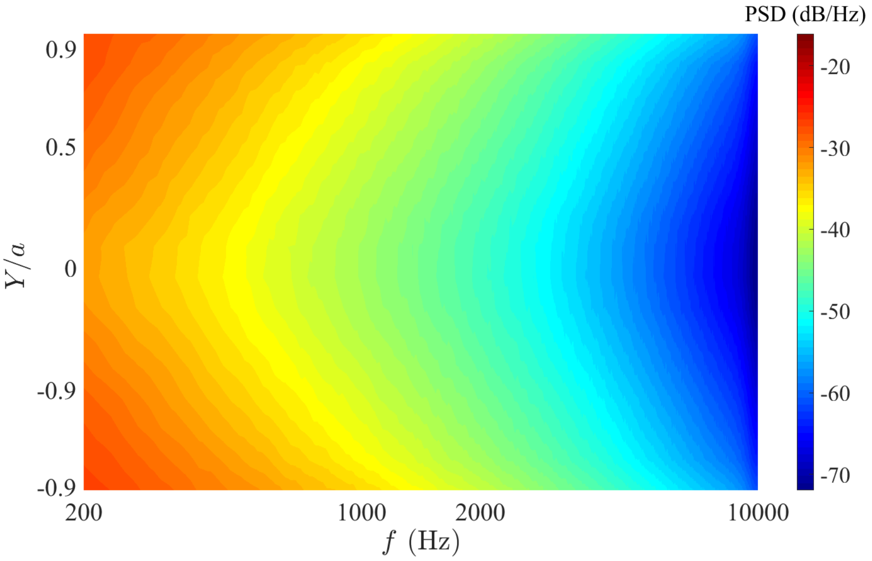

Figure 2.13: Velocity spectra in the test section with an mean flow speed of 10.0 m/s.

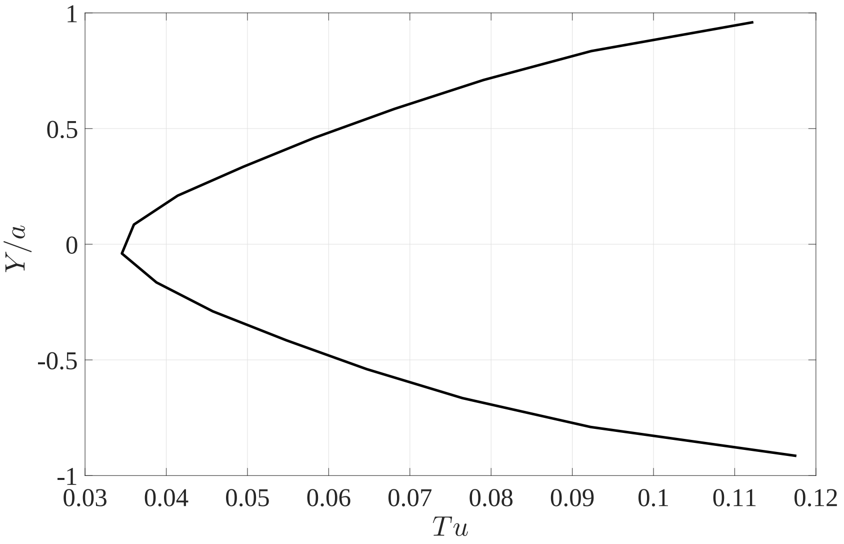

Figure 2.14: Turbulence intensity Tu in the test section with an mean flow speed of 10.0 m/s.

where u_{rms} is the root mean square velocity, $u(r)$ is the time averaged flow velocity at the measured point, and r is radius measured from the duct axis. The highest turbulence intensity is about 0.12 occurring near the duct wall. The lowest turbulence intensity is about 0.035 occurring at the duct centre line.

2.4 Summary

This chapter describes the construction and evaluation of the experimental duct rig for the investigation of the noise generation by single hole restrictors. The rig can be used to measure the restrictor sound field in the duct and the far field radiated sound power. This rig can also be used to make the aerodynamic measurements. The properties of the experimental rig can be summarized as:

- The internal diameter of the test section is 100 mm. The range of the mean flow speeds in the duct is from 10.0 m/s to 25.0 m/s.
- The flare installed at the end of the duct can minimise reflections above about 200 Hz. The measured reflection coefficient using the two microphone method is below 0.1 above this frequency.
- The silencer installed upstream of the test section can effectively absorb the noise generated by the fan and the orifice flow meter and reduce backgrounds sufficiently far below the restrictor noise levels.
- In the test section, the flow is fully developed. The highest velocity fluctuations in the test section are near the duct wall induced by the boundary layer, corresponding to the turbulence intensity of about 0.12.

Chapter 3

Sound field prediction of restrictor self-noise based on surface pressure

3.1 Introduction

Restrictors are widely used in the ADS to control the air distribution in different parts of the aircraft. The turbulent flow induced by a restrictor is a main noise source in the ADS. As the restrictor is often positioned close to an air outlet, the noise induced by it may not be sufficiently reduced by the silencer installed in the ADS. It is therefore important to understand and predict the acoustic properties of the restrictor for a quiet ADS design. In this chapter, the characteristics of the sound field and the flow field in a duct with a single-hole restrictor installed is investigated experimentally.

When a single-hole restrictor is installed in a duct, internal flow disturbances will be introduced. The flow field in the duct can be roughly divided into three parts: the sound generation, the sound propagation along the duct and the sound radiation from the end of the duct, as shown in Figure 3.1. The sound generation region is in the vicinity of the restrictor. In this region, high turbulence occurs due to the disturbance of flow by the restrictor. In the sound propagation region, as the turbulence dissipates along the duct, the acoustic field dominates well away from the restrictor and the sound generated in the sound generation region propagates almost without attenuation along the duct. Finally, at the end of the duct, the sound radiate to the far field. Based on the different characteristics of the different regions, different measurements were conducted to understand the sound generation mechanism by the restrictor in the duct. To investigate the mechanism of the restrictor self-noise, and identify the main sound sources, aerodynamic measurements were conducted in the sound generation region. Wall pressure measurements and in-duct sound power measurements were carried out along the duct to investigate the modal characteristics and transmitted sound power of

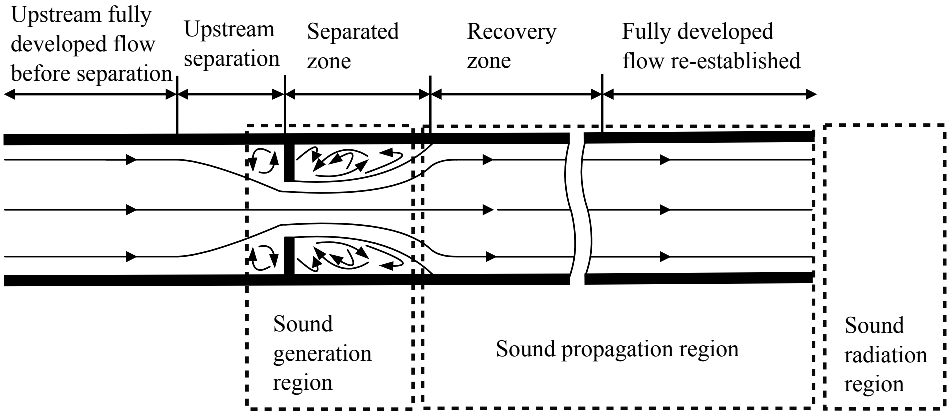

FIGURE 3.1: Problem description of single-hole restrictor self-noise generation.

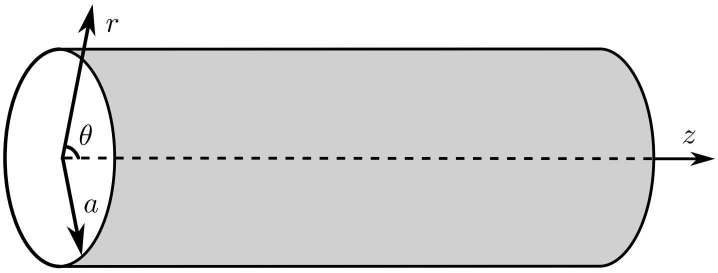

FIGURE 3.2: Cylindrical duct and cylindrical coordinates system.

the ducted sound field. Free-field sound power measurements were also conducted in the sound radiation region to provide an additional estimate for the sound power generated by the restrictor.

3.2 Sound field in a cylindrical duct

The sound field inside the duct can be expressed in terms of acoustic modes, identified by their azimuthal and radial order (m, n) respectively. This section describes the sound field in a cylindrical hard-walled duct.

Considering a straight, hard walled circular duct of radius a, in the absence of flow, we consider a cylindrical coordinate system (r, θ, z) aligned with the $z-$axis, as shown in Figure 3.2. In a source-free region of the duct, the acoustic pressure field satisfies the homogeneous wave equation

$$\nabla^2 p(\mathbf{x}, t) - \frac{1}{c_0^2}\frac{\partial^2 p(\mathbf{x}, t)}{\partial t^2} = 0, \tag{3.1}$$

We first consider a pressure field $p(\mathbf{x}, t)$ that is harmonic in time

$$p(\mathbf{x}, t) = \mathbf{Re}\{p(\mathbf{x})e^{i\omega t}\}, \tag{3.2}$$

where ω is the angular frequency.

The acoustic pressure $p(\mathbf{x})$ of a single frequency at point $\mathbf{x}(r, \theta, z)$ satisfies the Helmholtz equation in a cylindrical coordinate system,

$$\frac{\partial^2 p}{\partial r^2} + \frac{1}{r}\frac{\partial p}{\partial r} + \frac{1}{r^2}\frac{\partial^2 p}{\partial \theta^2} + \frac{\partial^2 p}{\partial z^2} + k^2 p = 0, \tag{3.3}$$

where $k = \omega / c_0$ is the acoustic wavenumber.

It is assumed that the time-harmonic solutions of the sound pressure are separable in the r, θ, z directions, thus

$$p(r, \theta, z, t) = p_r(r) p_\theta(\theta) p_z(z) e^{i\omega t}. \tag{3.4}$$

Substituting Equation 3.4 into Equation 3.3 and separating variables, the following equations are obtained.

$$\frac{d^2 p_z(z)}{dz^2} + k_z^2 p_z(z) = 0, \tag{3.5}$$

$$\frac{d^2 p_\theta(\theta)}{d\theta^2} + m^2 p_\theta(\theta) = 0, \tag{3.6}$$

$$\frac{d^2 p_r(r)}{dr^2} + \frac{1}{r}\frac{dp_r(r)}{dr} + p_r(r)\left(k - k_z^2 - \frac{m^2}{r^2}\right) = 0. \tag{3.7}$$

In the axial direction, the general solution is given by

$$p_z(z) = e^{\mp i k_z z}, \tag{3.8}$$

where k_z is the wave number in the z direction. The wave travels along the positive or negative axial direction. If only the wave travelling in the positive $z-$direction is considered,

$$p_z(z) = e^{-i k_z z}. \tag{3.9}$$

In the azimuthal direction, the general solution is given by

$$p_\theta(\theta) = e^{\mp i m \theta}. \tag{3.10}$$

Since $p_\theta(\theta)$ must be periodic with period of 2π, m is an integer.

In the radial direction, the general solution which satisfies the hard-walled boundary condition is given by

$$p_r(r) = \mathrm{J}_m{}'(k_r a) = 0, \tag{3.11}$$

where J_m is the Bessel functions of the first kind of order m, the prime denotes differentiation with respect to argument, and k_r is related to k and k_z by the dispersion relationship,

$$k_r^2 = k^2 - k_z^2. \tag{3.12}$$

Equation 3.11 can be satisfied only for certain discrete values of $k_{rmn}a$ which are listed in table 3.1. Therefore, for a given integer m, two following solutions for Equation 3.3 can be obtained.

$$p_{mn}(r,\theta,z) = A_{mn}\mathrm{J}_m(k_{rmn}r)e^{-im\theta}e^{-ik_{zmn}z}, \tag{3.13}$$

The general solution to Equation 3.3 with the hard-walled boundary condition of Equation 3.11 can therefore be written as follows:

$$p(r,\theta,z,t) = \sum_{m=-\infty}^{\infty}\sum_{n=0}^{\infty} A_{mn}\Psi_{mn}(r,\theta)e^{-i(k_{zmn}z-\omega t)}, \tag{3.14}$$

where Ψ_{mn} represents the normalised mode shape function,

$$\Psi_{mn}(r,\theta) = \frac{\mathrm{J}(k_{rmn}r)}{N_{mn}}e^{im\theta} \tag{3.15}$$

where N_{mn} is the normalisation constant, the derivation of which is shown in Appendix A,

$$N_{mn} = \sqrt{\mathrm{J}(k_{rmn}a)^2[1-(\frac{m}{k_{rmn}a})]}. \tag{3.16}$$

Each term in Equation 3.14 represents an acoustic mode, where m represents the spinning mode order, n represents the radial mode order. The modes corresponding to $m = 0$ are axisymmetric. An important mode in our problem is the plane wave mode, $m = n = 0$, which we will show contains most of the energy generated by the restrictor. For each (m, n) mode, there are m nodal lines, and n the number of concentric nodal lines. The nodal lines of lower order modes are shown in Figure 3.3. At the position of the nodal line, the sound pressure is zero. The signs + and − represent the phase relation.

The cut-off frequency for each mode can be calculated from

Table 3.1: Roots of Equation 3.11

n\m	0	1	2	3	4	5
0	0	1.8412	3.0542	4.2012	5.3176	6.4156
1	3.8317	5.3314	6.7061	8.0152	9.2824	10.5199
2	7.0156	8.5363	9.9695	11.345	12.681	13.987
3	10.1735	11.706	13.1704	14.5858	15.9641	17.3128

Table 3.2: Cut-off frequencies of lower modes for the duct rig in this work in Hz

n\m	0	1	2	3	4	5
0	0	2010	3335	4587	5806	7005
1	4183	5821	7322	8751	10135	11486
2	7660	9320	10885	12387	13845	15271
3	11107	12781	14379	15925	17430	18902

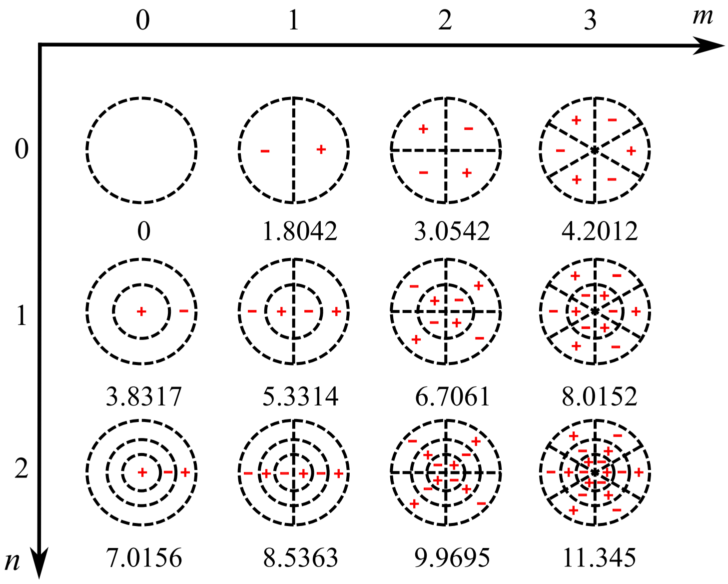

Figure 3.3: Nodal lines of lower order (m, n) modes.

$$f_{mn} = \frac{j_{mn}c_0}{2\pi a}, \tag{3.17}$$

where $j_{mn} = k_{rmn}a$ are the roots of Equation 3.11, listed in Table 3.1. In the current work, the internal radius a of the duct is 0.05 m, thus the cut-off frequencies can be calculated through Equation 3.17. The cut-off frequencies in the duct used in the current duct are listed in Table 3.2. At frequencies greater than the cut-off frequencies, the mode can propagate without attenuation. If the frequency is lower than the cut-off frequency, the mode, referred to as an evanescent mode, will attenuate exponentially down the duct. Below the lowest cut-off frequency in a circular duct, only the plane wave can propagate. This frequency will be shown to be important in the current work.

3.3 Flow induced noise in an empty duct

To investigate the noise generation by in-duct elements, it is important to know the aerodynamic and aeroacoustic properties in an empty duct.

3.3.1 Wall pressure measurement in an empty duct

For an empty hard-walled duct with fully developed turbulent flow, the sound is generated by turbulence induced by the boundary layer along the wall. In general, the sound radiation from the boundary layer will be weak for subsonic flow speeds, such as in the case of the ADS. For a fully developed flow in a duct, the aerodynamic pressure fluctuations are statistically uniform both circumferentially and axially, and extends over the entire duct and cannot be removed from the flow. It represents the minimum background acoustic field in the duct. To characterize this background noise level spectra, the wall pressure fluctuations were measured in the empty duct using a microphone mounted flush to the duct wall.

The experimental facility for the wall pressure measurement in the empty duct is the same as that for the background noise measurement, as shown in Section 2.3.2. The PSD of the wall pressure is shown in Figure 3.4. Similar to Agarwal's work [3], the PSD of the wall pressure under different flow speeds are scaled using the dynamic pressure q_c at the centre line of the duct, which is defined as

$$q_c = \frac{1}{2}\rho u_c^2, \tag{3.18}$$

where u_c is the flow velocity at the duct centre. In Figure 3.4, $St_c = \frac{fD}{u_c}$ is the Strouhal number based on the internal diameter of the duct D and the flow velocity at the duct centre. No narrow band peaks are present at the duct mode cut-off frequencies shown in Figure 3.4. The wall pressure spectra collapse reasonably well when plotted against Strouhal number, which suggests that the pressure field in the empty duct is dominated by the turbulence induced by the boundary layer and is therefore not acoustic in origin. The presence of hydrodynamic pressure fluctuations along the duct wall is the reason for the low measured coherence shown in Figure 2.9.

When the in-duct element is installed in the duct, the radiated sound power from the end of the duct is much higher than in the empty duct. Background noise levels in the duct due to turbulent wall pressure fluctuations are therefore negligible and do not need to be considered further in this work.

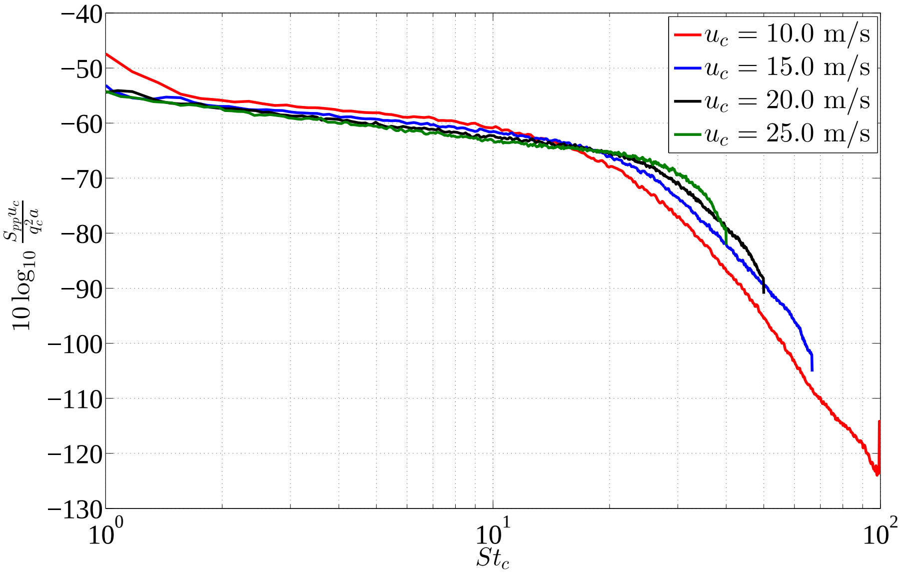

FIGURE 3.4: Wall pressure of the empty duct under different mean flow speeds scaled using the dynamic pressure at the duct centre q_c.

3.4 Aerodynamic properties near the restrictor

A schematic of the typical flow around a single-hole restrictor is shown in Figure 3.5. When air passes through the restrictor, it is forced to pass through the hole of the restrictor. Due to the blockage of the restrictor, separation occurs at the upstream corner between the duct wall and the restrictor. The upstream pressure increases slightly due to the blockage. As the air passes through the restrictor, the flow speed increases and the static pressure decreases. The flow speed keeps increasing until it reaches the vena contracta where the flow speed reaches its maximum and the static pressure reaches its minimum. The flow expands downstream of the vena contracta. The flow speed decreases and the pressure increases. However, due to energy losses, the pressure cannot fully recover. A larger primary recirculation occurs downstream of the restrictor. A much smaller secondary recirculation also occurs at the downstream corner of the restrictor. The primary recirculation occurs between the restrictor and the mean reattachment point. At the reattachment point the wall shear stress is zero. The flow in the separated zone is highly turbulent causing unsteady pressures over the surface of the restrictor. This mechanism will be investigated in this thesis as the main source of noise by the restrictor.

For the upstream separation, according to the experimental results of Agarwal [5], occurs at about 0.8 duct diameters upstream of the restrictor. In this work, the duct diameter of the experimental rig is 0.1 m. The upstream separation is assumed to occur within 80 mm upstream of the restrictor.

For the downstream separation, some researchers [13, 14, 44, 46] have investigated the

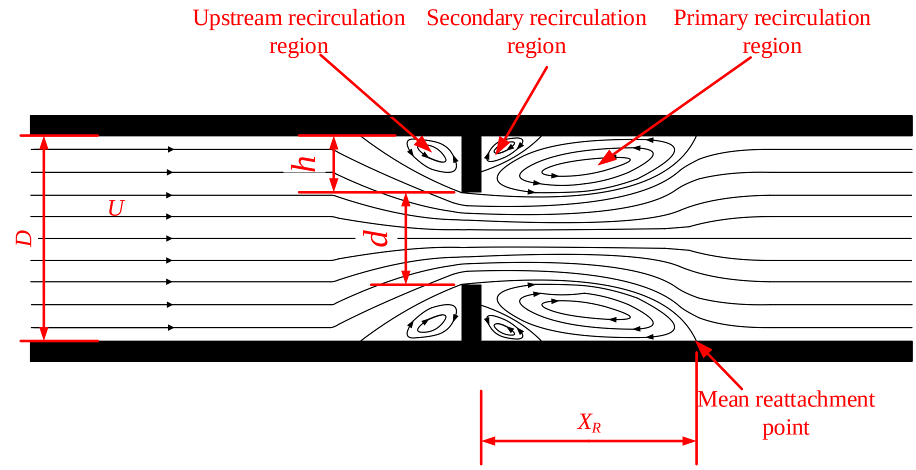

FIGURE 3.5: A schematic of flow state near the restrictor.

distance between the restrictor and the reattachment point. According to their experimental results, the length of recirculation zone is about 10 times the height h of the restrictor. The height of the single-hole restrictor h can be calculated from

$$h = \frac{1}{2}(D - d), \tag{3.19}$$

where D is the internal diameter of the duct which is the same as the external diameter of the restrictor, d is the internal diameter of the restrictor. The measurements by [13, 14, 44, 46] were obtained at the Reynolds number smaller than 72000. Agarwal [5] found that as the Reynolds number becomes larger, the ratio between the distance and the height of the restrictor becomes smaller. In this thesis, the smallest Reynolds number based on the experimental rig is about 72000. The mean reattachment point is assumed to be located within $10h$ downstream of the restrictor.

3.4.1 Static pressure measurements near the restrictor

In this section, static pressure measurements near the restrictor were made to observe the flow state around the restrictor. As discussed before, the static pressure measurement must cover the 0.8 duct diameters upstream of the restrictor and $10h$ downstream of the restrictor.

3.4.1.1 Experimental arrangement of static pressure measurement

The experimental arrangement for the static pressure measurement is shown schematically in Figure 3.6. The pressure transducer used in this measurement was a ZOC33 miniature pressure scanner with 64 pressure inputs manufactured by Scanivalve. A total of 10 pressure taps were mounted in the duct wall upstream of the restrictor. The distance between two adjacent pressure taps was 10 mm. As a flange was installed to

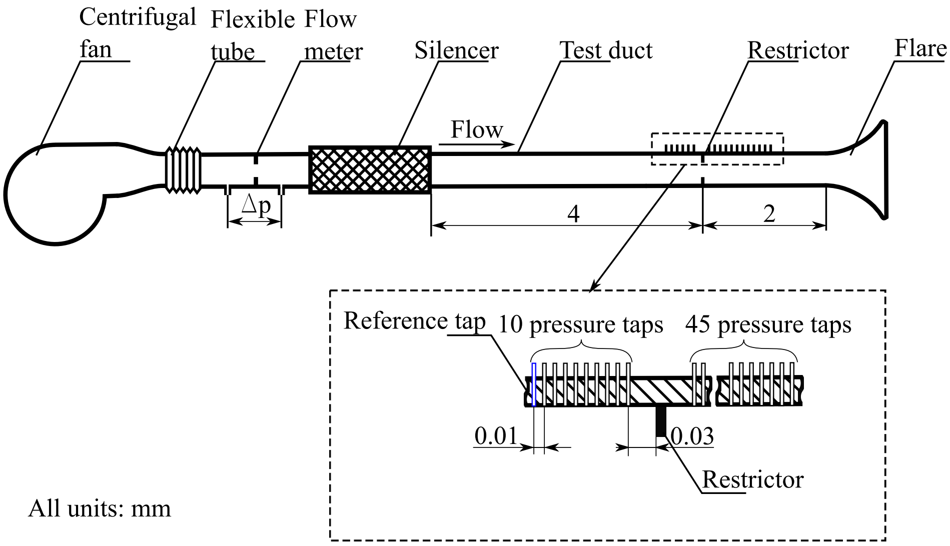

FIGURE 3.6: Schematic illustration of the experimental arrangement for the static pressure drop measurement.

support the restrictor, the pressure taps cannot to be mounted immediately upstream of the restrictor. The distance between the closest pressure tap and the restrictor was 30 mm. The pressure taps therefore covered 120 mm upstream of the restrictor. The arrangement of the pressure taps downstream of the restrictor was similar to the upstream except with more pressure taps. A total of 45 pressure taps were mounted downstream of the restrictor and covered 480 mm downstream of the restrictor. The mean flow speeds in the duct ranged from about 10 m/s to 25 m/s.

3.4.1.2 Expermental results of static pressure measurement near the restrictor

A representative experimental measurement of the static pressure drop distribution normalized by the dynamic pressure of the free stream versus streamwise distance X from the restrictor normalized by the height of the restrictor h is shown in Figure 3.7. The reference static pressure was the static pressure measured at the first pressure tap upstream of the restrictor, as shown in Figure 3.6. The internal diameter of the restrictor is 70 mm, with the height $h = 15$ mm. Four mean flow speeds are 10.1 m/s, 14.8 m/s, 19.6 m/s and 25.3 m/s.

It is shown in Figure 3.7 that, as the airflow approaches the restrictor, the pressure increases slightly due to blockage by the restrictor. A sudden pressure drop occurs when flow passes the restrictor. The static pressure continues to drop until the vena contracta is reached and then gradually increases until a maximum downstream pressure point is reached. The decrease in pressure as the airflow passes through the restrictor is a result of the increased velocity of the airflow passing through the open area of the restrictor. The velocity decreases as the airflow leaves the restrictor, the pressure increases and then tends to return to its original level. However, due to pressure losses caused by friction

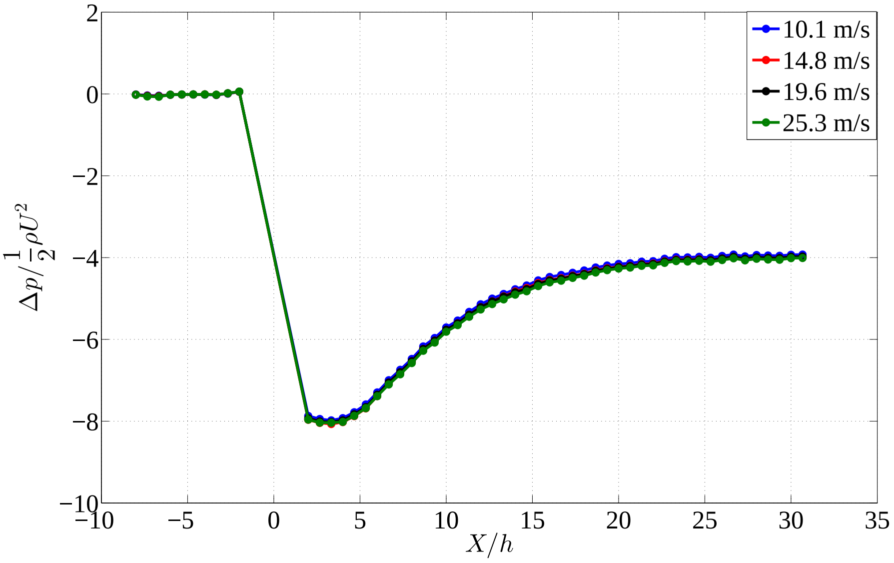

FIGURE 3.7: Axial variation of static pressure drop Δp for the restrictor with an internal diameter of 70mm under different flow speeds. The static pressure drop has been normalised using the dynamic pressure based on the mean flow speed in the duct.

and turbulence generation, the pressure does not fully recover. For the restrictor with different internal diameters, the distances from the restrictor to the fully recovered point are different. At the position of $X/h = 10$, where the flow reattaches, the static pressure is still recovering. The static pressure measurement by itself is not sufficient to estimate the size of the separation bubble, which is believed, indirectly, to be one of the regions (together with the region upstream of the restrictor) of highest turbulence level.

For a specific restrictor, the static pressure drop at different flow speeds can be collapsed using the dynamic pressure of the free stream,

$$\Delta p = C_d \frac{1}{2} \rho U^2 \tag{3.20}$$

where C_d is the drag coefficient. For a specific restrictor, when the Reynolds number is larger than 20000, C_d is a constant. In this work, as the minimum Reynolds number based on the duct diameter is about 73000, the effect of the flow speed on the drag coefficient can be ignored. This can also be observed from Figure 3.7 in which the static pressure is collapsed under different mean flow speeds.

3.4.2 Velocity fluctuation downstream of a single-hole restrictor

In this section, the flow state downstream of the restrictor was measured using a CTA. The time-averaged velocity profile, turbulence intensity, and the PSD of the unsteady velocity were measured.

3.4.2.1 Experimental arrangement

The experimental arrangement of the flow state measurements downstream of the restrictor using the CTA is shown in Figure 3.8. The internal diameter of the restrictor is 65 mm, corresponding to a height of 17.5 mm. A single hot-wire probe 55P11 from Dantec was driven using an AN-1005 CTA from AA Lab Systems. The hot-wire was calibrated in the free stream against a standard Pitot tube. The probe was inserted in the duct through the hole in the duct wall and was set perpendicular to the free stream direction. The overheat ratio of the hot-wire was set as 1.5. The data was sampled at 10 kHz for a duration of 40 seconds for each measured point.

A total of 9 measurement points were distributed downstream of the restrictor separated every 50 mm. The distance between the first measurement point and the restrictor was 100mm. This distance was selected based on the size of the flange, which was used to fix the restrictor and the size of traverse. According to the discussion concerning the point of reattachment, the length of the recirculation is about 17.5 cm. The first axial position of the measurement point is in the recirculation zone.

At each axial measurement position, the hot-wire probe was traversed along the radial direction of the cross-section of the duct corresponding to 76 measurement points. The step size was 1.25 mm starting from 2.5 mm from the wall. The total traverse radius was 95 mm, which is 5 mm less than the diameter of the duct for two reasons. The first is due to the fragility of the hot-wire probe since it is a difficult to position the probe very close to the wall without breakage. This limitation is not serious since boundary layer noise is not a main noise source in this problem. Second, to traverse the probe inside the duct, a hole which is slightly larger than the probe holder, was drilled in the duct wall. Consequently, the flow near the hole was affected by the hole. Measurements very close to the lower duct wall are therefore not important.

3.4.2.2 The flow state downstream of the restrictor

The radial variation of mean flow speed downstream of the restrictor of d=65 mm at various downstream locations is shown in Figure 3.9 for a mean flow speed in the duct of 21.7 m/s. Due to a lack of directivity of the single-wire, the velocity profile is ambiguous in the recirculation region. Outside of the recirculation zone, the direction of the main flow stream is parallel to the centre line of the duct, the mean flow velocity profile can be measured accurately using the single wire. The axial distance between the measured position and the restrictor are represented by non-dimensional distance X/D, where X is the distance between the measured position and D is the internal diameter of the duct. The development of the flow as it convects downstream is clearly shown. Due to the blockage of the restrictor, the mean flow velocity increases sharply when flow passes the restrictor. The flow expands to fill the whole cross-section of the duct and the maximum

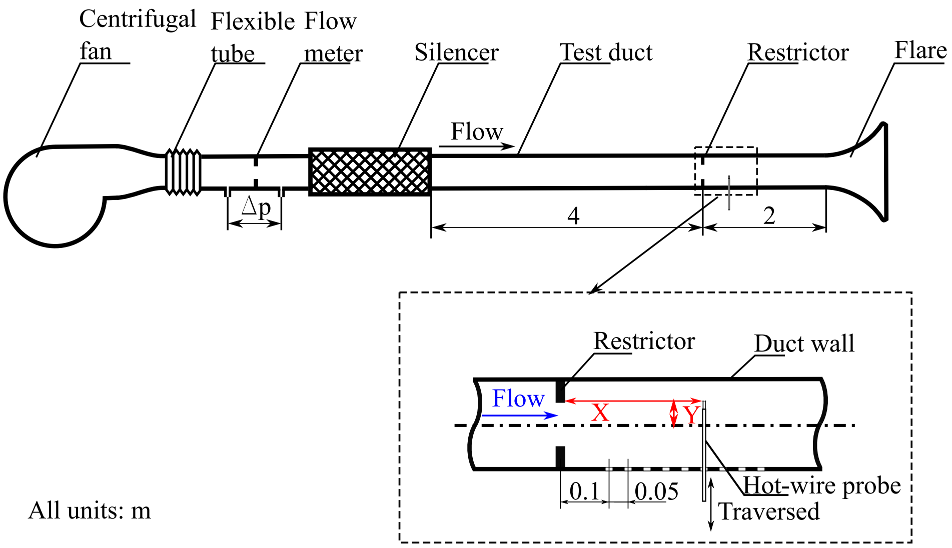

FIGURE 3.8: Schematic illustration of experimental arrangement of flow measurement downstream of the restrictor using CTA.

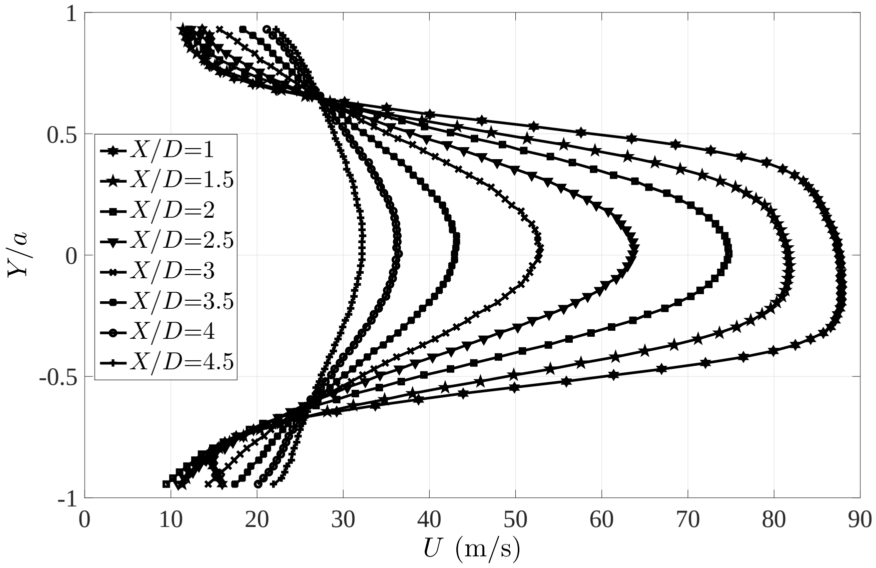

FIGURE 3.9: Mean flow velocity profile downstream of the restrictor with an internal diameter of d=65 mm under a mean flow speed of U=21.7 m/s. Streamwise measured positions X are normalised by duct diameter D and radial measured positions Y are normalised by duct radius a.

flow speed drops quickly. According to Figure 3.9, when $X/D = 1$, the maximum flow velocity is about 87m/s, which then drops to about 33m/s at $X/D = 4.5$.

Figure 3.10 shows the development of the turbulence intensity downstream of the restrictor. Close to the restrictor, the turbulence intensity has a large variation along the radial direction. Along the radial direction, from the duct wall to the centre line of the duct, the turbulence intensity increases gradually until the shear layer is reached at which the turbulence intensity is highest. The turbulence intensity then drops sharply moving towards the duct centre line where lowest turbulence intensity is observed. Along the

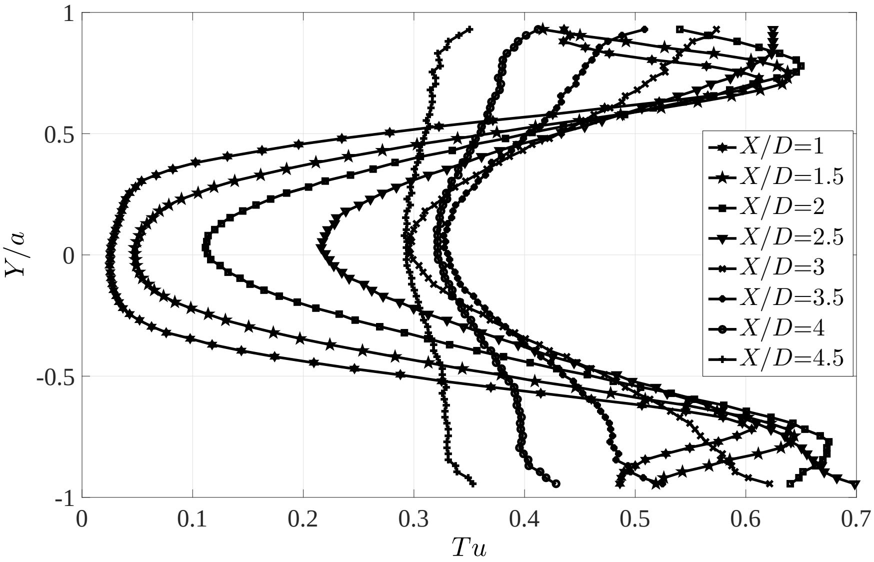

Figure 3.10: Turbulence intensity Tu downstream of the restrictor with an internal diameter of d=65 mm under a mean flow speed of U=21.7 m/s. Streamwise measured positions X are normalised by duct diameter D and radial measured positions Y are normalised by duct radius a.

axial direction, as the shear layer expands to the whole duct cross-section, the point of highest turbulence intensity moves towards the duct wall and the turbulence intensity decreases. Meanwhile, the turbulence intensity along the duct centre line is increasing. At $X/D = 4.5$, the furthest axial distance from the restrictor, the turbulence intensity along the radial direction has comparatively small variation (<0.05).

Maps of the velocity PSD versus radial distance at various axial locations is shown in Figure 3.11. The results are plotted over a fixed range of values from -60 dB to 0 dB to illustrate the development of the velocity spectra. The most intense velocity fluctuations occur in the shear layer near the restrictor. As the flow expands to the whole duct, the velocity fluctuation become more uniform at the different radial positions.

Velocity spectra in the recirculation and shear layer downstream of the restrictor is shown in Figure 3.12. The internal diameter of the restrictor was d=65 mm and the mean flow speed was U=21.7 m/s. Streamwise measured positions X were $X/D = 1$ downstream of the restrictor. In recirculation zone, no peaks appear on the velocity spectra. This may suggest a weak recirculation in this zone.

From the experimental results above, the following conclusions can be drawn. First, the mean flow velocity along the duct centreline downstream of the restrictor is much higher than the mean flow velocity due to blockage of the restrictor. The high flow speed drops quickly due to the expansion of the flow downstream of the restrictor. Second, the turbulence intensity is highest in the shear layer close to the restrictor. The largest velocity fluctuations also occur in the shear layer.

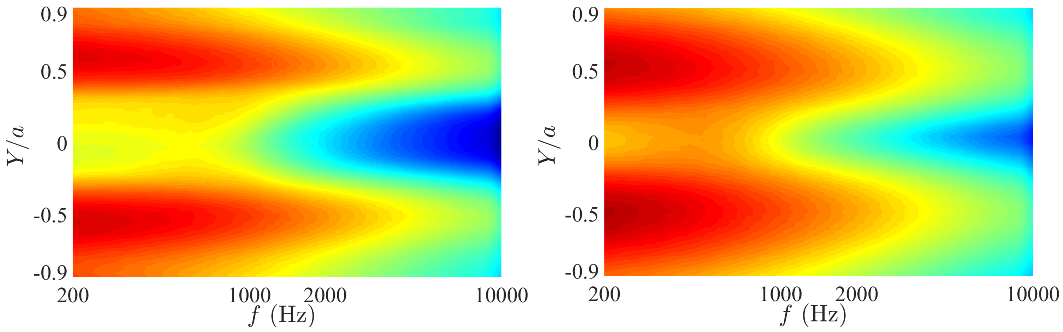

(a) $X/D = 1$ (b) $X/D = 1.5$

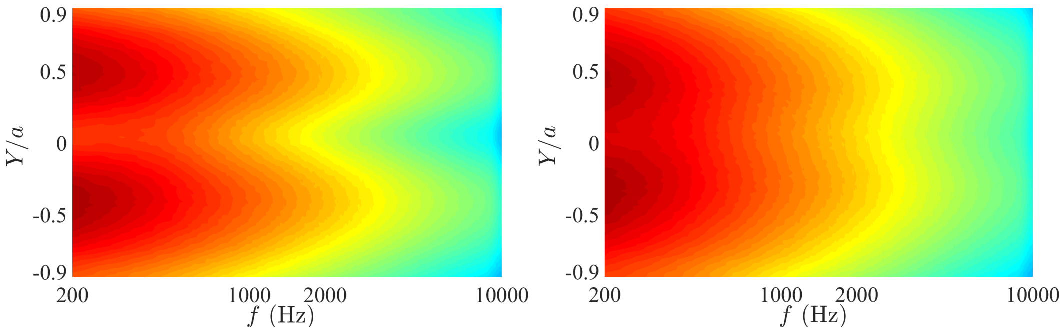

(c) $X/D = 2$ (d) $X/D = 2.5$

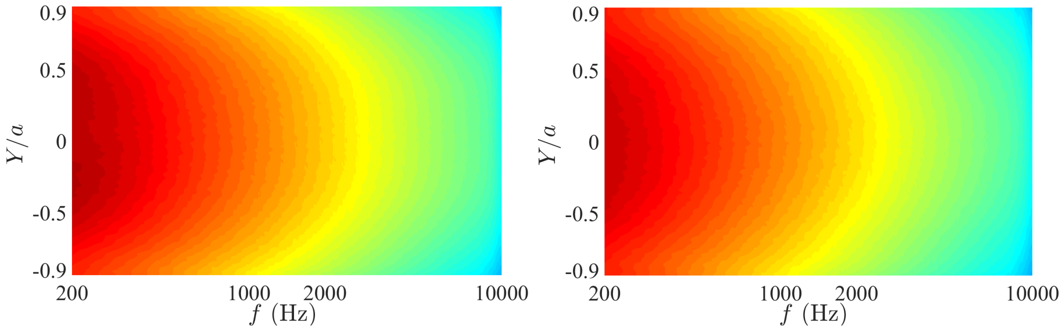

(e) $X/D = 3$ (f) $X/D = 3.5$

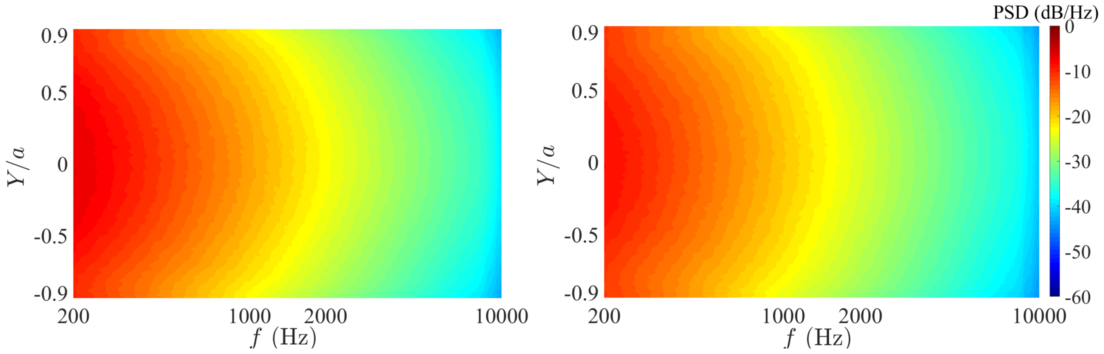

(g) $X/D = 4$ (h) $X/D = 4.5$

FIGURE 3.11: Velocity spectra downstream of the restrictor with an internal diameter of d=65 mm under a mean flow speed of U=21.7 m/s. Streamwise measured positions X are normalised by duct diameter D and radial measured positions Y are normalised by duct radius a.

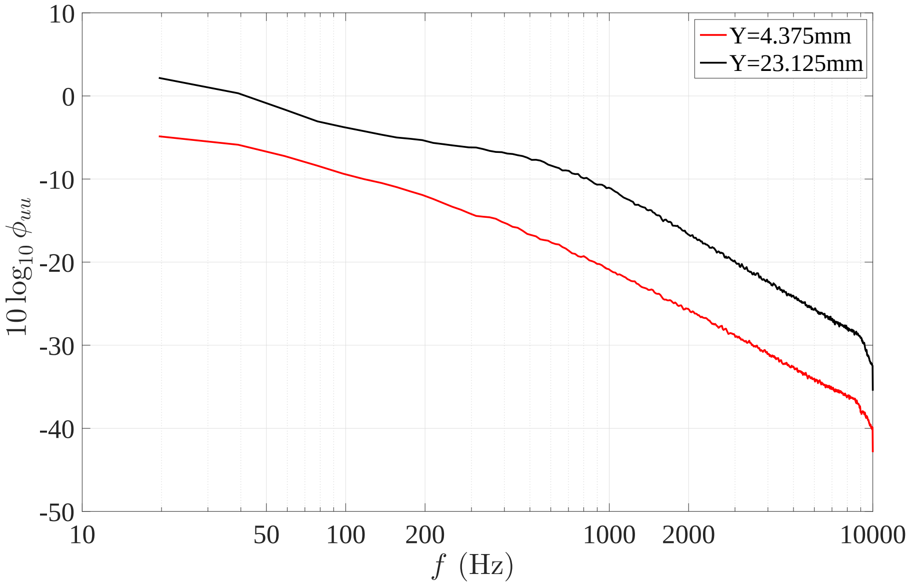

FIGURE 3.12: Velocity spectra in the recirculation and shear layer downstream of the restrictor with an internal diameter of d=65 mm under a mean flow speed of U=21.7 m/s. Streamwise measured positions X are $X/D = 1$ downstream of the restrictor.

3.5 Modal analysis

Well away from the restrictor, flow noise can be neglected compared to acoustic pressure fluctuations. The noise generated by the restrictor propagates along the duct in the form of a series of modes. In this section, modal analysis is performed from the pressure measurements on the duct wall to investigate the acoustic properties generated by the restrictor. The modal analysis results are useful for determining the acoustic field from the hydrodynamic pressure fluctuations and also for determining the sound power, as described in Section 4.3.2.

3.5.0.3 Experimental arrangement of modal analysis

The experimental arrangement for performing modal analysis is shown in Figure 3.13. A microphone array containing 12 microphones was flush-mounted to the duct wall to make the wall pressure measurements. The microphones used were FG-3329-P07 from Knowles Electronics and arranged circumferentially with the same angular interval. The microphone array was located outside of the recirculation zone of the restrictor (1.2 m downstream of the restrictor) to reduce the effect of hydrodynamic pressure fluctuations on the wall pressure measurement. As only one flush-mounted microphone ring was used, only spinning modes can be resolved up to order $m = 2$. The pressure data was sampled using a 24-bit National Instruments data acquisition system at a frequency of 20 kHz and the sampling time was 20s.

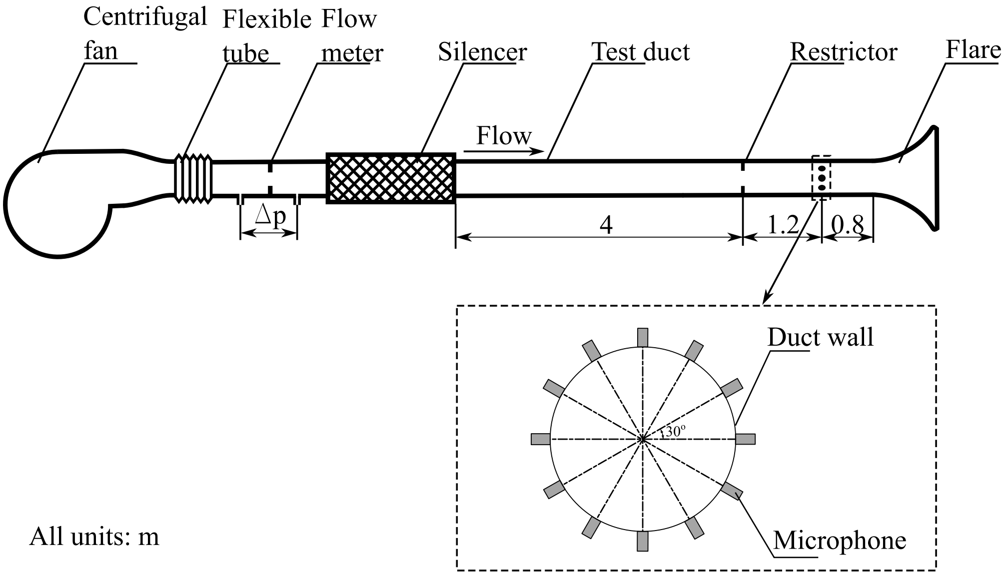

FIGURE 3.13: A schematic of the experimental arrangement of modal analysis.

3.5.0.4 Characteristic of the wall pressure spectrum

A representative experimental pressure spectrum is shown in Figure 3.14. The PSD of the wall pressure shown in Figure 3.14(a) has both a broadband spectrum and narrow band peaks. The frequencies of the peaks correspond to the modal cut-on frequencies. The nodal lines of the first four higher order modes are also plotted in Figure 3.14. It is clearly shown that both spinning modes (m) and radial mode (n) have been excited.

3.5.0.5 Modal amplitude calculation

For a cylindrical hard-walled duct of diameter $0.1m$, the first radial mode is cut-on at a frequency of $4183Hz$. If only the plane wave mode and the first two spinning modes are considered, according to Equation 3.14, the sound field in a narrow frequency band can be expressed as

$$p(r,\theta,z)=\sum_{m=-2}^{2}p_m(r,z)e^{-im\theta}, \tag{3.21}$$

where P_m is the modal pressure of the m^{th} spinning mode, which only contains the single radial mode order $n=0$ given by

$$p_m(r,z)=A_m\frac{\mathrm{J}_m(k_{rm0}r)}{N_{m0}}e^{-ik_{zm0}z}. \tag{3.22}$$

As $e^{-im\theta}$ are an orthonormal basis, Equation 3.22 can be inverted to give the pressure mode amplitude as

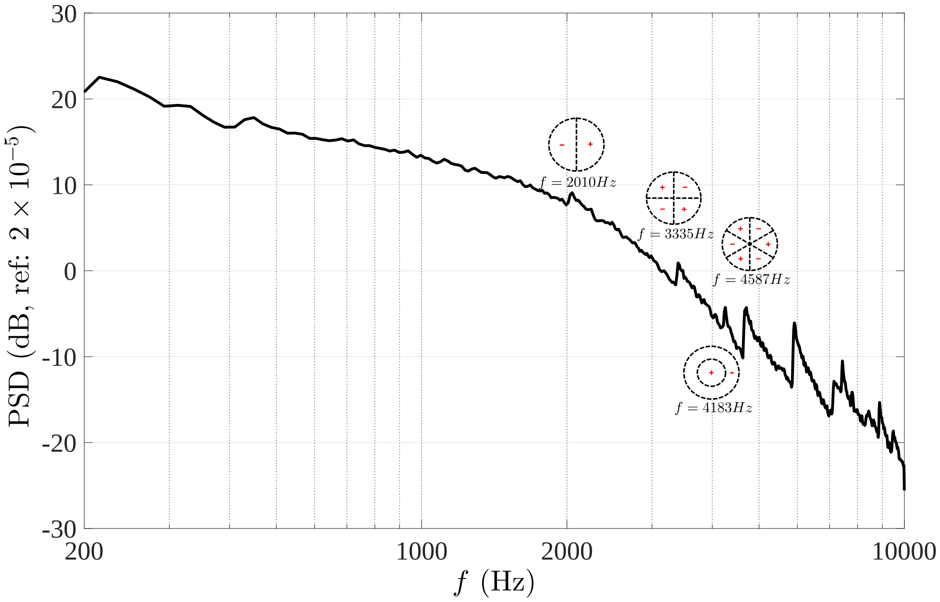

(a) PSD of the wall pressure.

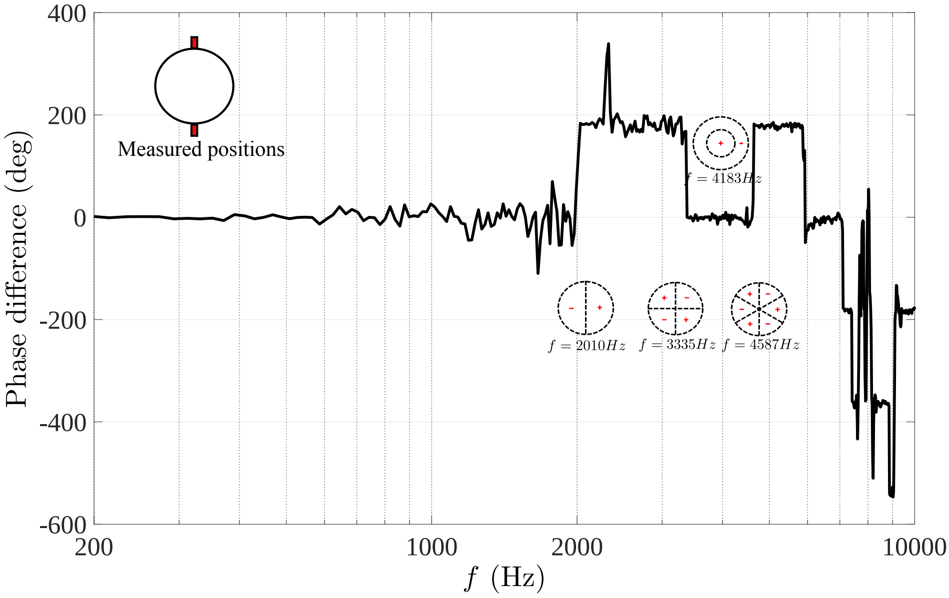

(b) Phase difference between two measured points.

FIGURE 3.14: Wall pressure measured at 1.2 m downstream of the restrictor with an internal diameter of 65 mm under a mean flow speed of 10.0 m/s. The corresponding modal shape is plotted at cut-on frequencies.

$$p_m(r,z) = \frac{1}{2\pi}\int_0^{2\pi} p(r,\theta,z)e^{-im\theta}d\theta. \tag{3.23}$$

In practice, Equation 3.23 is realised in the discrete form as

$$p_m(r,z) = \frac{\Delta\theta}{2\pi}\sum_{j=1}^{N} p(r,\theta_j,z)e^{-im\theta_j}. \tag{3.24}$$

where N is the total number of the measurement points along circumferential direction. In this thesis, a total of 12 microphones were used, therefore $N = 12$. The noise from the restrictor is a broadband random signals and thus we can only calculate the PSD of the mode amplitudes, thus the following equation is obtained,

$$S_{pp} = \frac{\Delta\theta}{2\pi}\frac{\Delta\theta}{2\pi}\sum_{j=1}^{N}\sum_{j'=1}^{N} S_{\theta_j\theta_j'}(r,\theta_j,\theta_j',z)e^{-im(\theta_j-\theta_{j'})}, \tag{3.25}$$

where

$$S_{\theta_j\theta_j'}(r,\theta_j,\theta_j',z) = \frac{\pi}{T}p(r,\theta_j,z)p^*(r,\theta_{j'},z) \tag{3.26}$$

is the cross spectrum of sound pressure between two microphones. Therefore,

$$|A_m(r,z)|^2 = \frac{N_m^2}{(\mathrm{J}(k_{rm}a))^2}\frac{\Delta\theta}{2\pi}\frac{\Delta\theta}{2\pi}\sum_{j=1}^{N}\sum_{j'=1}^{N} S_{\theta_j\theta_j'}(r,\theta,\theta,z)e^{-im(\theta_j-\theta_{j'})} \tag{3.27}$$

The PSD of the mode amplitudes for the first three spinning modes can be obtained from measurements of the pressure cross spectrum between all combinations of microphone pairs.

3.5.0.6 Experimental results of modal analysis

Representative experimental results of the modal analysis for different restrictors under different mean flow speeds is shown in Figure 3.15. At frequencies below the first cut-on frequency, the sound power is carried only by the plane wave. In all cases the modal spectra decay very close to f^{-2}. This f^{-2} frequency scaling law is also observed in the far field sound power discussed in chapter 4. The plane wave modal spectra are higher for the restrictor with smaller internal diameter. Increasing the flow speed also leads to an increasing level of the modal spectra. At frequencies above the first cut-on frequency, higher order modes are excited. Figure 3.15 clearly shows that the modal amplitudes for the restrictor d=65 mm is higher than that for the restrictor d=75 mm, suggesting that the restrictor with smaller internal diameter is more efficient in exciting the higher order modes. Figure 3.15(c) and Figure 3.15(d) shows that the relative amplitude of the modal spectra for the mean flow speed of 10.0 m/s is higher than that for the mean flow speed of 22.5 m/s. The reason may be that when the flow speed is higher, the narrow-band peaks increase smaller than the broad-band noise spectra.

3.6 Surface pressure and wall pressure measurements

3.6.1 Sound field due to a dipole source distribution in an infinite duct

According to the classical Curle theory for aerodynamic sound generation from solid surfaces, noise sources due to a turbulent flow over a solid surface can be represented by a distribution of dipole sources. As the restrictor is installed in the duct perpendicular to the axial direction of the duct, the acoustic source due to the restrictor can be represented by acoustic dipole sources aligned in the axial direction distributed over the surfaces of the restrictor. In this section, an expression is derived for the calculation of sound field induced by an axial dipole source distribution in a cylindrical duct. In this work, as the highest mean flow speed is 25 m/s in the duct, the effect of the flow speed on sound propagation is ignored. The sound reflections at the end of the duct are also ignored. The acoustic source of interest is the unsteady aerodynamic loading on the restrictor, due to the presence of the recirculation regimes on both sides of the restrictor. The time-varying pressure $p(t)$ at any point $\mathbf{x}(r, \theta, z)$ in the cylindrical duct can be calculated from the Green's function solution to the wave equation 3.1,

The acoustic source due to the restrictor is represented by acoustic dipole sources distributed over the surface of the restrictor. The strength of the dipole is $\mathbf{f}(\mathbf{x}_s, \tau) = \mathbf{f}(r_s, \theta_s, z_s, \tau)$. The time-varying pressure at any point in the duct can be calculated from the Green's function solution to the wave equation 3.1,

$$p(\mathbf{x}, t) = \int_{-\infty}^{+\infty} \int_{S_r} \mathbf{f}(\mathbf{x}_s, \tau) \cdot \nabla G(\mathbf{x}, t \mid \mathbf{x}_s, \tau) dS_r d\tau, \tag{3.28}$$

where $\mathbf{f}(\mathbf{x}_s, \tau)$ is the unsteady aerodynamic loading per unit area on the point $\mathbf{x}_s(r_s, \theta_s, z_s)$ on the restrictor surface S_r at time τ, and (r_s, θ_s, z_s) represents an arbitrary point on the surface of the restrictor in cylindrical coordinates. The integration over S_r is performed over both sides of the restrictor. Therefore, $\mathbf{f}$ is the 'pressure jump' across the restrictor. A Green's function solution for an infinite, hard-walled cylindrical duct without flow can be expressed as [16]

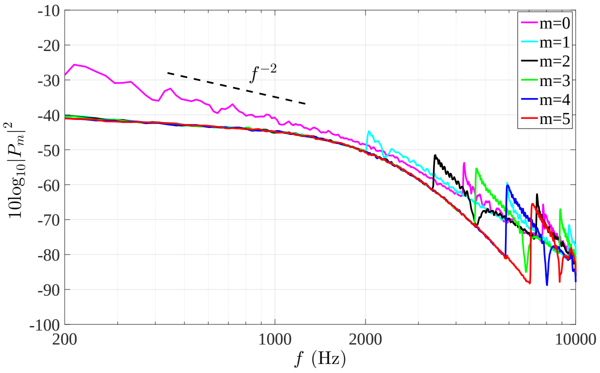

(a) d=65 mm, U=10.0 m/s.

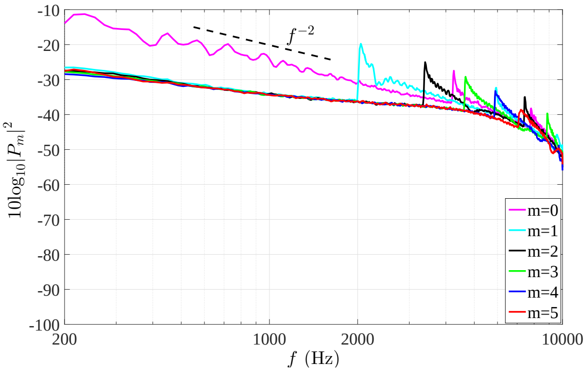

(b) d=65 mm, U=22.5 m/s.

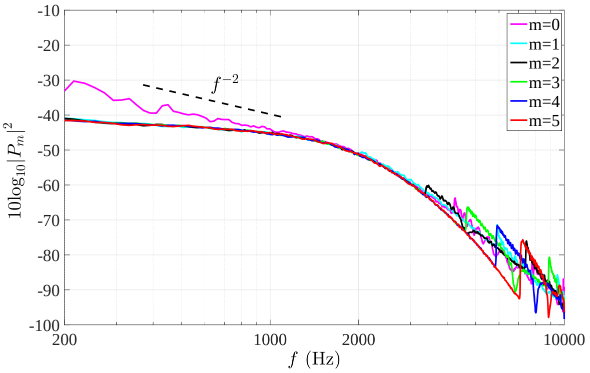

(c) d=75 mm, U=10.0 m/s.

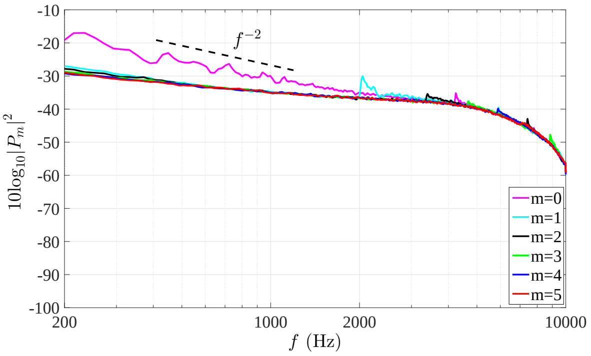

(d) d=75 mm, U=22.5 m/s.

FIGURE 3.15: Comparison of measured modal pressure spectra for restrictors with internal diameters of 65 mm and 75 mm under mean flow speeds of 10.0 m/s and 22.5 m/s.

$$G(\mathbf{x}, t \mid \mathbf{x}_s, \tau) = \frac{i}{4\pi} \sum_{m,n} \frac{\psi_{mn}(r_s, \theta_s)\psi^*_{mn}(r, \theta)}{N^2_{mn}} \int_{-\infty}^{+\infty} \frac{e^{i\omega(t-\tau)} e^{-ik_{zmn}(z-z_s)}}{k_{zmn}} d\omega, \tag{3.29}$$

where

$$\psi_{mn}(r, \theta) = \mathbf{J}_m(k_{rmn} r) e^{-im\theta}. \tag{3.30}$$

is the eigenfunctions of the cylindrical duct.

A dipole source aligned at an angle α relative to the duct axis has components given by

$$\vec{n} = [0, \sin\alpha, \cos\alpha]. \tag{3.31}$$

As the restrictor is installed perpendicular to the axis of the duct, in Equation 3.31, $\alpha = 0$, therefore

$$\vec{n} = [0, 0, 1]. \tag{3.32}$$

The ∇ operator in cylindrical coordinates is given by

$$\nabla G = \frac{\partial G}{\partial r}\vec{r} + \frac{1}{r}\frac{\partial G}{\partial \theta}\vec{\theta} + \frac{\partial G}{\partial z}\vec{z}. \tag{3.33}$$

Substituting Equation 3.29 into Equation 3.33 gives the non-zero component of ∇G as

$$\frac{\partial G}{\partial z_s}\vec{z} = \frac{i\vec{z}}{4\pi} \sum_{m=-\infty}^{\infty} \sum_{n=0}^{\infty} ik_{mn} \frac{\psi_{mn}(r, \theta)\psi^*_{mn}(r_s, \theta_s)}{N^2_{mn}} \int_{-\infty}^{\infty} \frac{e^{i\omega(t-\tau)} e^{-ikmn(z-z_s)}}{\kappa_{mn}} d\omega. \tag{3.34}$$

Substituting Equations 3.34 into Equation 3.28 gives the expression of the sound field induced by the restrictor as

$$p(\mathbf{x}, t) = \frac{1}{2\pi} \int_{-\infty}^{\infty} \int_{S_r} f(\mathbf{x}_s, \tau) \sum_{m=-\infty}^{\infty} \int_{-\infty}^{\infty} g_m(\mathbf{x}_s, x, r, \omega) e^{i\omega(t-\tau)} d\omega dS_r d\tau, \tag{3.35}$$

where

$$g_m(\mathbf{x}_s, x, r, \omega) = \frac{1}{2} \sum_{n=0}^{\infty} \frac{\psi_{mn}(r, \theta)\psi^*_{mn}(r_s, \theta_s)}{N^2_{mn}} e^{-ik_{zmn}(z-z_s)}. \tag{3.36}$$

Equation 3.35 can be written in the frequency domain as

$$p(\mathbf{x},\omega) = \int_{S_r} f(\mathbf{x}_s,\omega) \sum_{m=-\infty}^{\infty} g_m(\mathbf{x}_s,x,r,\omega) dS_r. \tag{3.37}$$

Since the noise from the restrictor is broadband, it can be expressed as the PSD of the sound pressure which is defined by

$$S_{pp}(\mathbf{x},\omega) = \lim_{T\to\infty} \frac{\pi}{T} \mathrm{E}\{|\mathrm{p}(\mathbf{x},\omega)|^2\}, \tag{3.38}$$

where E{} denotes expectation. Substituting Equation 3.37 into Equation 3.38 gives

$$S_{pp}(\mathbf{x},\omega) = \int_{S_r}\int_{S_r^{'}} \sum_{m=-m_0}^{m_0} \sum_{m^{'}=-m_0}^{m_0} S_{ff}(\mathbf{x}_s,\mathbf{x}_s^{'},\omega) g_m(\mathbf{x}_s,x,r,\omega) g_{m^{'}}^{*}(\mathbf{x}_s^{'},x,r^{'},\omega) dS_r dS_r^{'}, \tag{3.39}$$

where

$$S_{ff}(\mathbf{x}_s,\mathbf{x}_s^{'},\omega) = \lim_{T\to\infty} \frac{\pi}{T} \mathrm{E}\{\mathrm{f}(\mathbf{x}_\mathrm{s},\omega)\mathrm{f}^{*}(\mathbf{x}_\mathrm{s}^{'},\omega)\} \tag{3.40}$$

is the cross spectral density of the fluctuating force acting on the restrictor. The cross spectral density defined by Equation 3.40 is determined by the degree to which the fluctuating force at two points $\mathbf{x}_s$ and $\mathbf{x}_s^{'}$ are correlated at frequency ω.

At the frequencies below the first cut-on frequency, only the plane wave can propagate in the duct. Equation 3.39 simplifies to

$$S_{pp}(\mathbf{x},\omega) = \frac{1}{4A^2} \int_{S_r}\int_{S_r^{'}} S_{ff}(\mathbf{x}_s,\mathbf{x}_s^{'},\omega) dS_r dS_r^{'}. \tag{3.41}$$

For frequencies above the first cut-on frequency, higher order modes are excited, leading to

$$\begin{aligned} S_{pp}(\mathbf{x},\omega) = \frac{1}{4} \int_{S_r}\int_{S_r^{'}} \sum_{m=-m_0}^{m_0} \sum_{n=0}^{n_0} \sum_{m^{'}=-m_0}^{m_0} \sum_{n^{'}=0}^{n_0} & S_{ff}(\mathbf{x}_s,\mathbf{x}_s^{'},\omega) \\ & \times \frac{\psi_{mn}(r,\theta)\psi_{mn}^{*}(r_s,\theta_s)}{N_{mn}^2} \frac{\psi_{m^{'}n^{'}}^{*}(r,\theta)\psi_{m^{'}n^{'}}(r_s,\theta_s)}{N_{m^{'}n^{'}}^2} \\ & \times e^{-ik_{zmn}(z-z_s)} dS_r dS_r^{'}. \end{aligned} \tag{3.42}$$

In Equations 3.41 and 3.42, if the hydrodynamic loading on the two sides of the restrictor are assumed to be uncorrelated, the cross spectra can be expressed as

$$S_{ff}(\mathbf{x}_s, \mathbf{x}_s^{'}, \omega) = S_{ff}^{+}(\mathbf{x}_s^{+}, \mathbf{x}_s^{+'}, \omega) + S_{ff}^{-}(\mathbf{x}_s^{-}, \mathbf{x}_s^{-'}, \omega), \tag{3.43}$$

where the superscript $\{\}^{+}$ and $\{\}^{-}$ represent upstream and downstream surfaces of the restrictor respectively. Using Equations 3.41 and 3.42, the PSD of the pressure field in the cylindrical hard-walled duct can be obtained, provided the cross spectra of the fluctuation force over both sides of the restrictor are known. It also implies that the sound field induced by an restrictor is controlled by the “pressure jump”across the restrictor.

As the flow reattaches downstream of the restrictor, unsteady pressures on the duct wall are produced. For pressure fluctuations on the duct wall, the axis of the dipoles are perpendicular to the duct wall in the radial direction with unit vector components given by

$$\vec{n} = [1, 0, 0]. \tag{3.44}$$

Normal to the rigid-walled duct wall, the boundary condition gives

$$\frac{\partial G(\mathbf{x}, t \mid \mathbf{x}_s, \tau)}{\partial r} = 0. \tag{3.45}$$

Substituting Equations 3.44 and 3.45 into Equation 3.28 gives

$$p(\mathbf{x}, t) = 0, \tag{3.46}$$

suggesting that the surface pressure fluctuations on the duct wall do not radiate sound. The dominant noise source is therefore located on the surface of the restrictor rather than the duct wall where highest pressure fluctuations occur, as we show in the next section.

3.6.2 Wall pressure and surface pressure measurements around the single-hole restrictor

In this section, the surface pressure on the restrictor is measured to calculate the sound field transmitted along duct based on Equation 3.39. Meanwhile, the wall pressure immediate upstream and downstream of the restrictor is measured to obtain the flow state near the restrictor.

3.6.2.1 Experimental arrangement

The experimental arrangement required to measure the wall pressure at the upstream and downstream of the restrictor and the surface pressure on the restrictor is shown in Figure 3.16. For the wall pressure measurement near the restrictor, a total of 10 microphones were flush-mounted to the duct wall along the axial direction upstream of the restrictor and a total of 50 microphones were flushed-mounted to the duct wall downstream of the restrictor, as shown in Figure 3.16. The distances between the restrictor and the first microphone, both upstream and downstream were 0.03 m. The distance between two adjacent microphones was 0.015 m. The measured points cover a distance of 0.162 m upstream of the restrictor and 0.765 m distance downstream of the restrictor.

For the surface pressure measurements, restrictors with pressure taps were 3D-printed due to the difficulty to mount the microphone on the surface of the restrictor whose thickness was 3.3 mm. The pressure taps were connected to the tubes for the transmission of the surface pressure. The tubes were made to run inside the restrictor. Due the thickness of the restrictor, only a small number of pressure taps can be located on the surface of the restrictor. To investigate the properties of the surface pressure and calculated the sound field based on the surface pressure measurements, two arrangements of pressure taps were designed, as shown in Figures 3.16(b) and 3.16(c). The internal diameter of the restrictor shown in Figures 3.16(b) and 3.16(c) is 65 mm. For the first arrangement, 5 pressure taps were placed along the radial direction where the distance between two consecutive pressure taps is 2.9 mm. It is assumed that the pressure fluctuations over the restrictor are axi-symmetric and therefore only one line of radial pressure taps were used. Along the circumferential direction, 60 pressure taps were placed at the radius of 41.25 mm. The distance between two consecutive taps was about 4.3 mm. For the second arrangement, two lines of pressure taps, each containing 9 taps along the radial direction were located. The distance between two consecutive taps along the radial direction was 2 mm. The angular interval between the two lines was 3.4°. A similar arrangement of pressure taps for the restrictors with internal diameters of 55 mm and 75 mm were also manufactured.

The experimental arrangement for the calibration of the pressure taps is shown in Figure 3.17. The calibration of the microphone was made by measuring the transfer function between the remote microphone and reference microphone. The remote microphones for performing the surface pressure measurements were electric condenser microphone FG-3329-P07 manufactured by Knowles Electronics, and the reference microphone used was a G.R.A.S. $1/4''$ microphone. The remote microphones were connected to the tubes by a T-junction. The other end of the T-junction was connected to a long capillary tube of internal radius of 1 mm and about 3 m in length to avoid reflections from the sealed end. A steel horn was made to make sure that the reference microphone and the pressure tap of the restrictor was in the same sound field. The sound field was generated by a loudspeaker driven by the white noise source. After the transfer function was obtained for each pressure tap, the real pressure at the pressure taps can be calculated based on the measured data from the remote microphones.

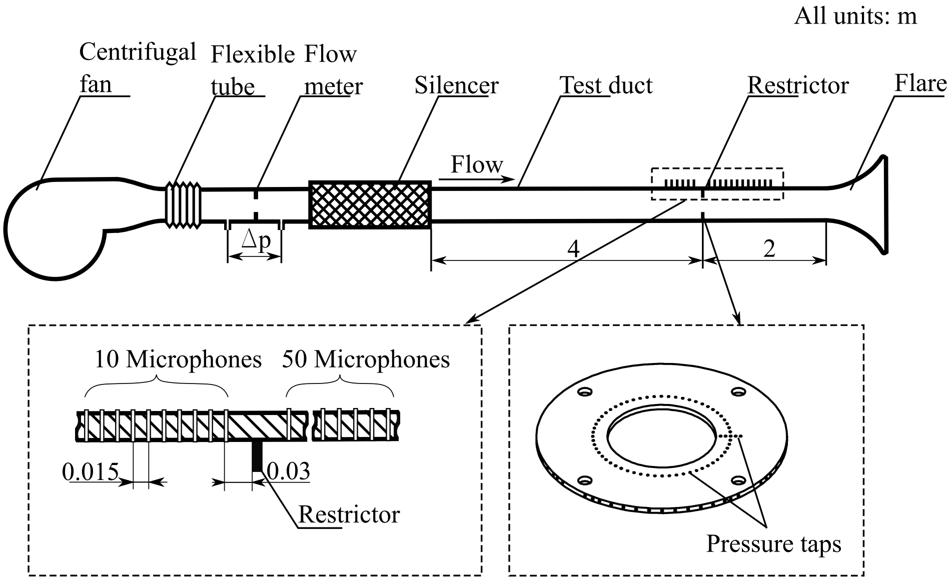

(a) Experiment arrangement of surface pressure measurement and wall pressure measurement at immediate upstream and downstream of the restrictor.

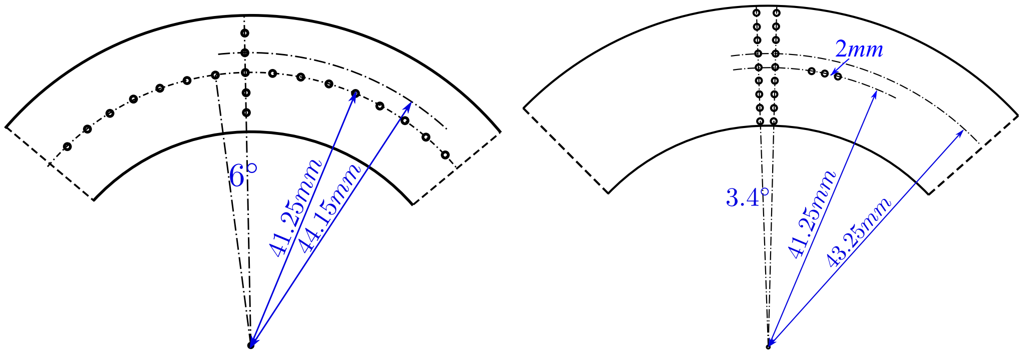

(b) The first arrangement of pressure taps on the surface of the restrictor.

(c) The second arrangement of pressure taps on the surface of the restrictor.

Figure 3.16: Experiment arrangement of surface pressure measurement and wall pressure measurement at immediate upstream and downstream of the restrictor.

3.6.2.2 Properties of the wall pressure and the surface pressure

Maps of the PSD of the duct wall pressure, as a function of axial distance (normalized by the duct diameter D) upstream and downstream of the restrictor with an internal diameter of 65 mm under a mean flow speed of 10.8 m/s, is shown in Figure 3.18. The minus sign of the horizontal axis represents the upstream of the restrictor. For comparison, the surface pressure which was measured with a radial position of 47.25 mm is also plotted in this figure. Region A and region D represent the duct wall downstream of the restrictor, and region B and region C represent the upstream and downstream surfaces of the restrictor respectively.

The wall pressure spectra upstream of the restrictor are seen to be much smaller than that downstream of the restrictor. Upstream of the restrictor the flow appears to be slowly varying until about 0.5 duct diameters of the restrictor. The highest spectral

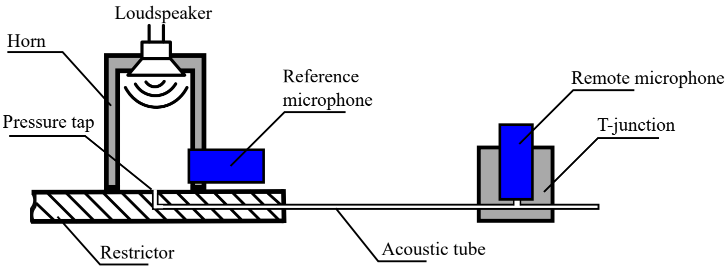

(a) Schematic illustration of the calibration of the pressure taps.

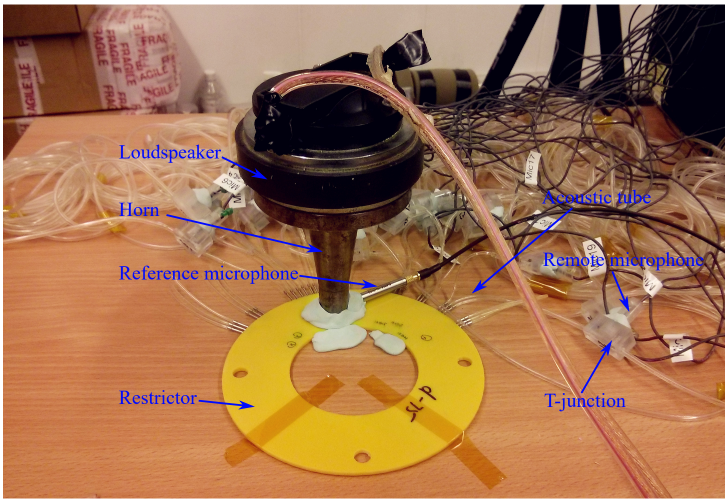

(b) Photo of the calibration of the pressure taps.

FIGURE 3.17: Experimental arrangement of the calibration of the pressure taps in the restrictor.

level occurs at about 0.1 duct diameter upstream of the restrictor.

Downstream of the restrictor, the highest pressure fluctuations occur about 1.2 duct diameters of the restrictor, which may represent the reattachment point as discussed previously. The wall pressure spectra decrease gradually downstream of the restrictor. The surface pressure on the restrictor is much smaller compared to the pressure on the duct wall. As discussed above, even though the pressure fluctuations on the duct wall are much higher than that on the restrictor, they are non-radiating.

Maps of the PSD of the surface pressure versus radius (normalized by the radius of the duct) on the upstream surface of the restrictor is shown in Figure 3.19(a). The highest pressure fluctuation is seen to occur near the inner edge of the restrictor. A large variation in pressure spectra are observed between the inner edge of the restrictor and the duct wall. Pressure fluctuations are observed to increase as the edge of the restrictor is approached from the duct wall. Also observed near the duct wall are narrow band peaks corresponding to the cut-on frequencies of the duct modes. Clearly, in this region, above about 4kHz the acoustic field dominates hydrodynamic pressure fluctuations.

Maps of the PSD of the surface pressure versus radius (normalized by the radius of the duct) on the downstream surface of the restrictor is shown in Figure 3.19(b). Similar

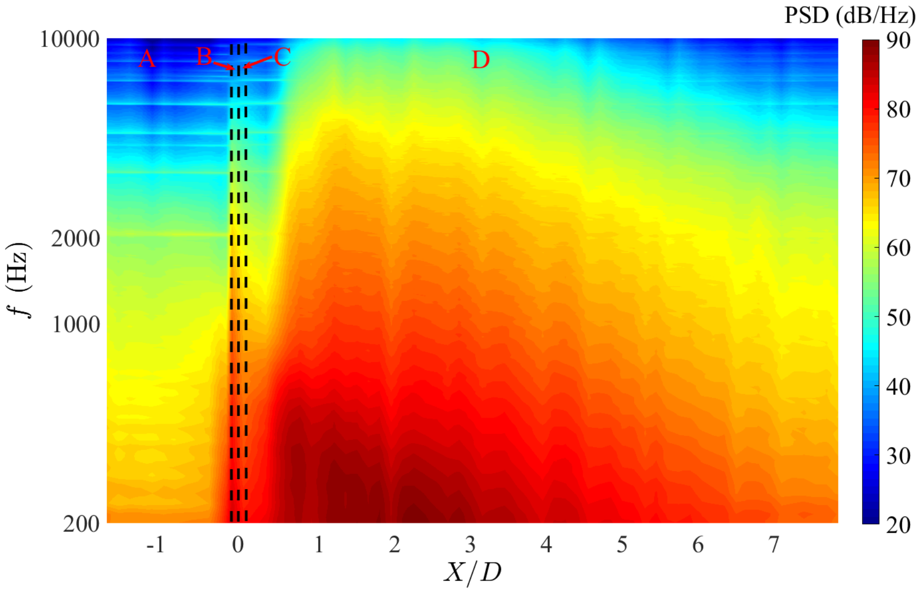

Figure 3.18: PSD of the pressure fluctuations on the restrictor surface and on the duct wall at measured position X, region B and region C represent upstream and downstream surface of the restrictor and region A and region D represent upstream and downstream duct wall near the restrictor. The test case has an internal diameter of the restrictor d=65 mm and a mean flow speed U=10.8 m/s in the duct.

to the upstream side, highest pressure fluctuations also occur at the inner edge of the restrictor. From the inner edge to about $Y/a = 0.75$, the fluctuations decrease gradually. Pressure fluctuations appear to decrease slowly at radial positions closer to the wall than $Y/a = 0.75$ on the downstream surface of the restrictor.

The PSD of pressure fluctuations on the upstream surface of the restrictor along the circumferential direction at a fixed radius of 47.25 mm is shown in Figure 3.20(a). The pressure spectra are observed to remain roughly constant suggesting that the flow behaviour around the restrictor is axis-symmetric on upstream surface. For the downstream side, similar results are obtained, as shown in Figure 3.20(b).

To calculate the sound field in the duct using Equations 3.42 and 3.41, the cross spectrum between any two points on the surface of the restrictor must be calculated between all points on the surface of the restrictor. We therefore start with a measurement of the coherence function to estimate the magnitude of the cross spectrum in relation to the PSD. The cross spectrum properties of the surface pressure is obtained in this section for the estimation of the cross spectrum between any two points on the restrictor surface in the next section.

The coherence of the surface pressure on the upstream side of the restrictor with an internal diameter of 65 mm for a mean flow speed of 10.8 m/s is shown in Figure 3.21. Along the radial direction, the surface pressure has coherence values greater than 0.5 for measurement points of 2 mm apart up to about 2000 Hz. Between 2000 Hz and 5000 Hz, the coherence is higher than 0.1. Above 5000 Hz, the coherence drops to about

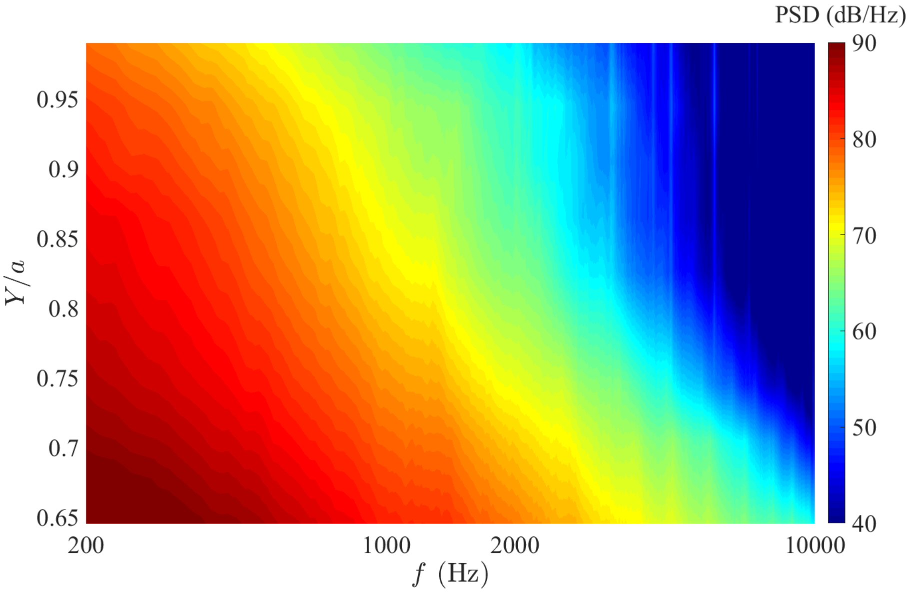

(a) PSD of the pressure fluctuation on the upstream surface of the restrictor.

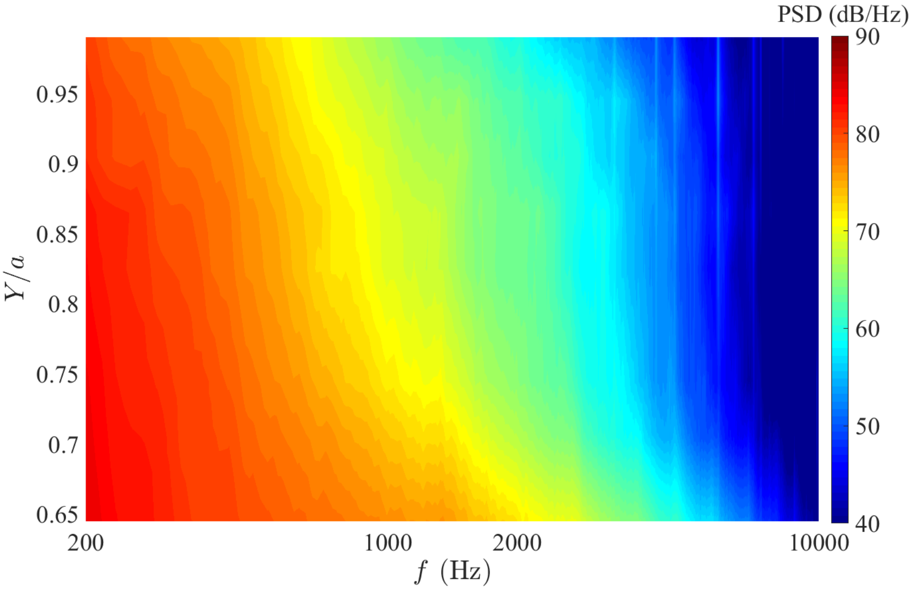

(b) PSD of the pressure fluctuation on the downstream surface of the restrictor.

FIGURE 3.19: PSD of the pressure fluctuations on the upstream and downstream surface of the restrictor along radial direction with an internal diameter of the restrictor d=65 mm and a mean flow speed U=10.8 m/s in the duct.

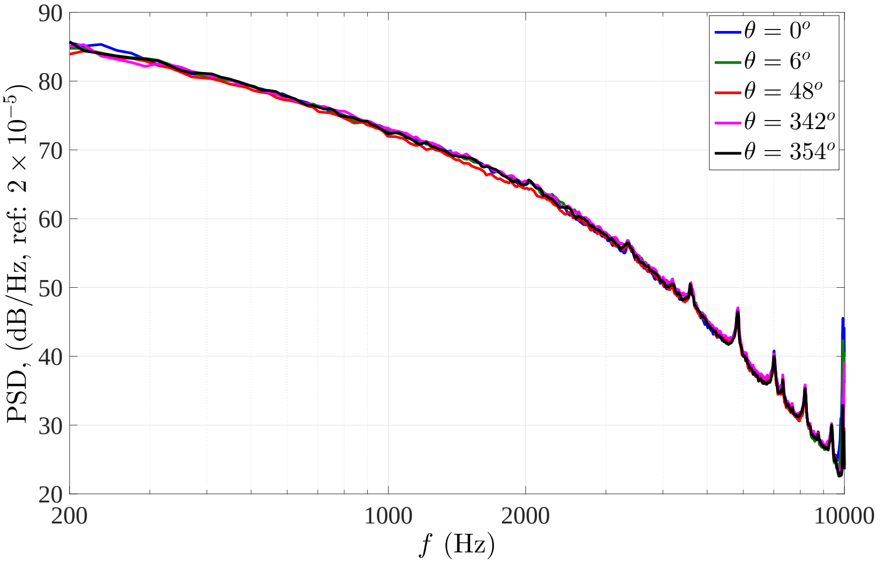

(a) PSD of the pressure fluctuation on the upstream surface of the restrictor along circurferential direction.

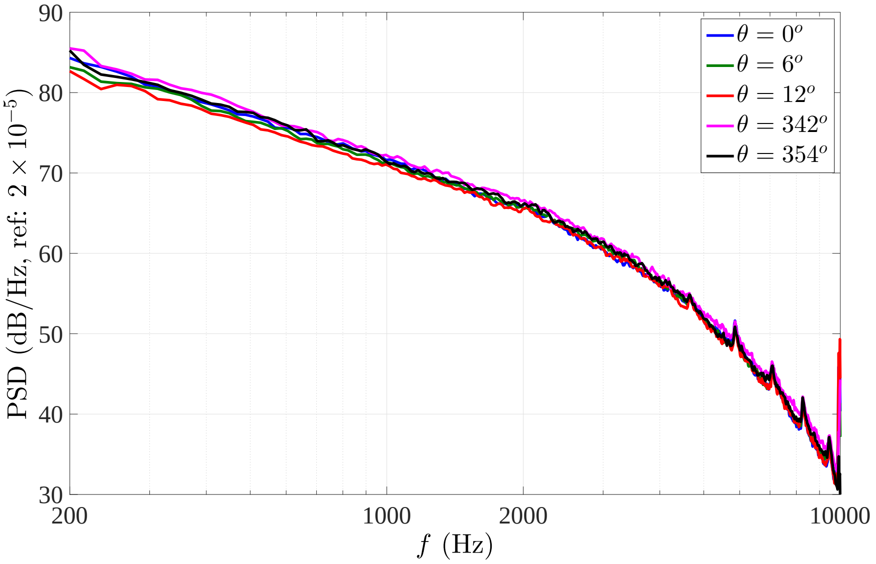

(b) PSD of the pressure fluctuation on the downstream surface of the restrictor along circurferential direction.

FIGURE 3.20: Comparison of the PSD of the pressure fluctuation on the surface of the restrictor along circumferential direction with an internal diameter of the restrictor d=65 mm and a mean flow speed U=10.8 m/s in the duct.

zero. At a separation distance of 4 mm, the surface pressure only has significant levels of coherence (> 0.1) in the plane wave frequency range less than about 2kHz. The coherence drops gradually as the distance between two points increasing. When the separation distance is greater than 8 mm, the coherence falls to nearly 0. The coherence along the circumferential direction is shown in Figure 3.21(c). The measured points is at a radius of 41.25 mm. When the distance between two measured points is 1.5 mm, the coherence of the surface pressure along the circumferential direction is very small in the plane wave frequency range but increases sharply above 3000 Hz. When the separation is 3 mm, the coherence drops to about zero. Above 3000 Hz, similar coherence as the 1.5 mm separation distance is obtained. The high coherence above 3000 Hz implies that the surface pressure measurement in high frequency range is starting to become dominated by the acoustic field radiated by the restrictor. The presence of the cut-on frequencies is clearly observed.

The coherence of the surface pressure on the downstream side of the restrictor has similar properties, but slightly higher in level, to the upstream surface, as shown in Figure 3.22.

The magnitude of the cross spectral density of the pressure fluctuation on the upstream surface of the restrictor along radial and circumferential direction is shown in Figure 3.23 for different separation distances corresponding to the coherence measurements shown in Figure 3.21. Consistent with the coherence, the magnitude of the CPSD drops rapidly as the separation distance increases. Along the radial direction, when the separation distances are at 6 mm and above, the magnitude of the CPSD are more than 10dB below the PSD of the surface pressure at the reference position. As the separation distance increases above 6 mm the cross spectrum ceases to change. Along the circumferential direction, similar behaviour of the CPSD is observed. When the separation increases above 3 mm, the magnitude of the CPSD ceases to change.

Based on the discussion above, the following properties of the surface pressure can be concluded.

- The surface pressure is axi-symmetric.
- The PSD of the surface pressure on the upstream side is higher than the downstream side. For both sides, the highest pressure fluctuation occurs at the inner edge of the restrictor.
- For both sides, the surface pressure is coherent within a small distance. In the plane wave frequency range, the coherence length is about 4 mm in the radial direction and 1.5 mm in the circumferential direction when the mean flow speed is 10 m/s. Above the first cut-on frequency, the coherence length is about 2 mm in the radial direction and smaller than 1.5 mm in the circumferential direction.

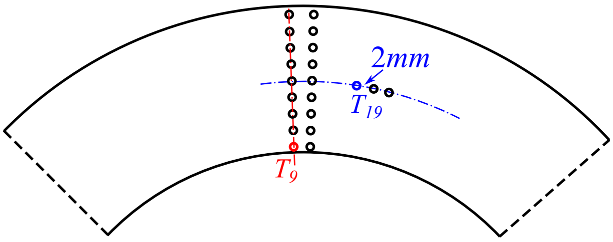

(a) Arrangements of pressure taps for coherence measurements.

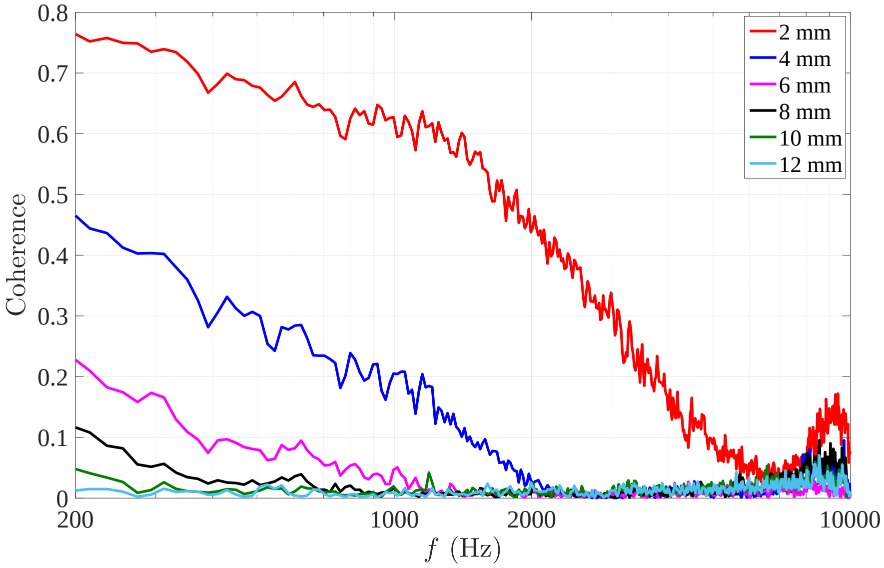

(b) Coherence of the surface pressure on the upstream side along radial direction.

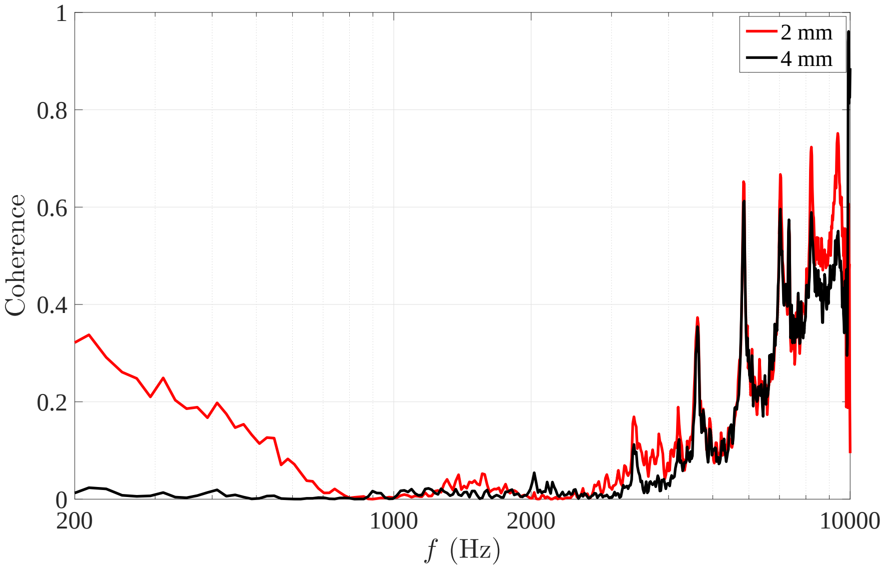

(c) Coherence of the surface pressure on the upstream side along circurferential direction.

FIGURE 3.21: Coherence of the surface pressure on the upstream side of the restrictor with an internal diameter of the restrictor d=65 mm and a mean flow speed U=10.8 m/s in the duct. For radial direction, the coherence was between pressure tap T_9 and other pressure taps in radial direction. For circumferential direction, the coherence was between pressure tap T_{19} and other pressure taps along circumferential direction.

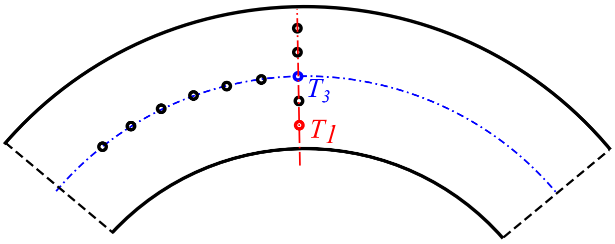

(a) Arrangements of pressure taps for coherence measurements.

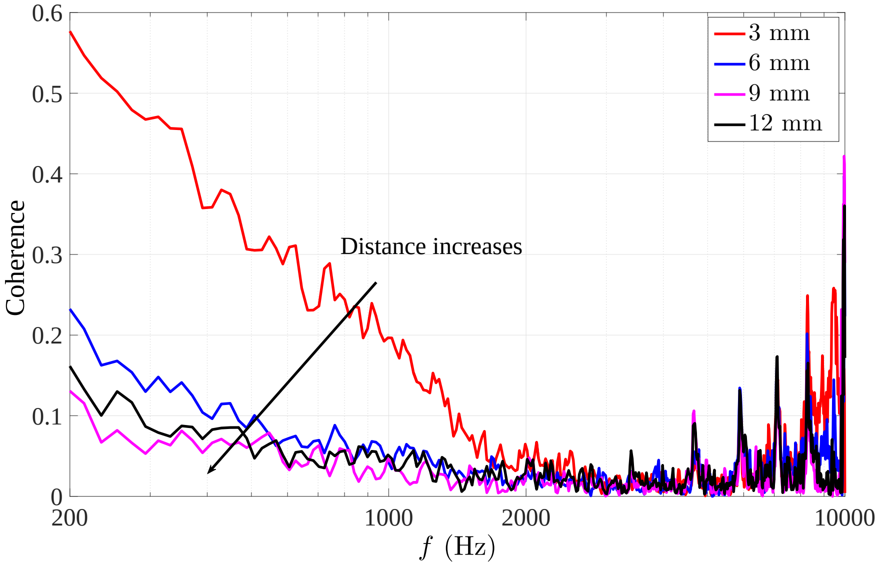

(b) Coherence of the surface pressure on the downstream side along radial direction.

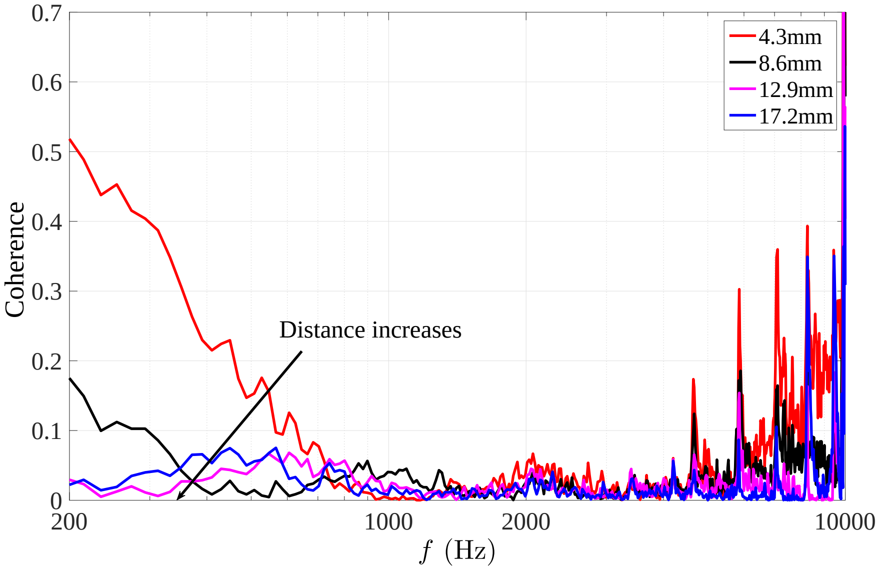

(c) Coherence of the surface pressure on the downstream side along circurferential direction.

FIGURE 3.22: Coherence of the surface pressure on the downstream side of the restrictor with an internal diameter of the restrictor d=65 mm and a mean flow speed U=10.8 m/s in the duct. For radial direction, the coherence was between pressure tap T_1 and other pressure taps in radial direction. For circumferential direction, the coherence was between pressure tap T_3 and other pressure taps along circumferential direction.

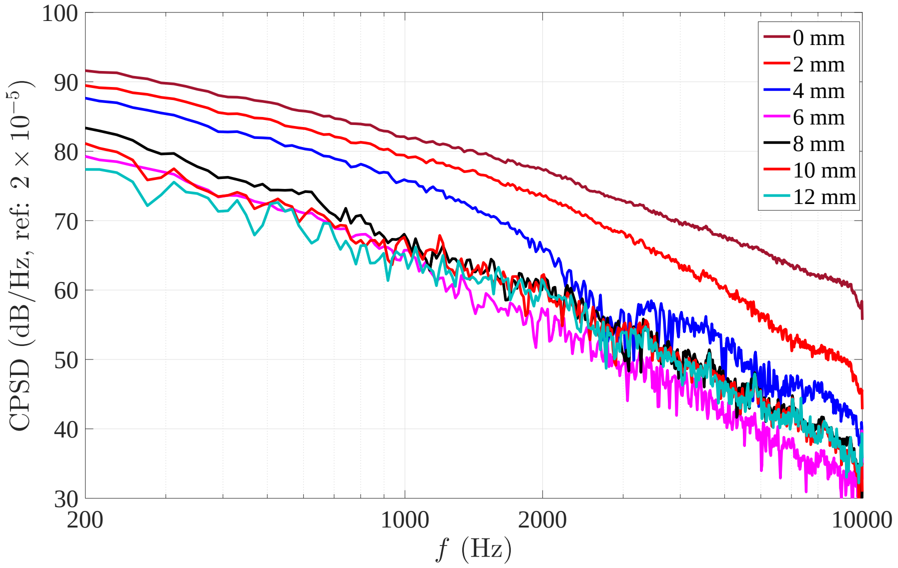

(a) Cross spectral density (CPSD) of the pressure fluctuation on the upstream surface of the restrictor along radial direction.

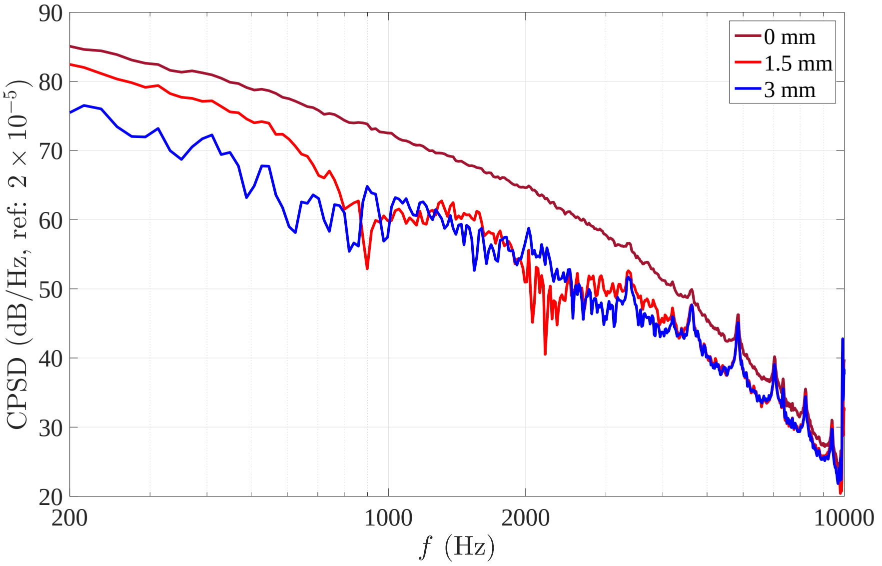

(b) Cross spectral density (CPSD) of the pressure fluctuation on the upstream surface of the restrictor along circumferential direction.

FIGURE 3.23: CPSD of the pressure fluctuation on the upstream surface of the restrictor along radial direction and circumferential direction with an internal diameter of the restrictor d=65 mm and a mean flow speed U=10.8 m/s in the duct.

- For both sides, the surface pressure is coherent over a larger distance along the radial direction than the circumferential direction. The coherence length is larger on the downstream side than the upstream side.

3.6.2.3 Sound field prediction in the duct based on the surface pressure

To use Equations 3.41 and 3.42 to calculate the sound field in the duct induced by the restrictor, the surface pressure cross spectra over the entire surface of the restrictor must be measured. However, it is difficult to measure the surface pressure over the entire surface of the restrictor due to the way in which the pressure tubes run inside the restrictor. Based on the properties of the surface pressure and the pressure taps arrangement sketched in Figure 3.16(c), approximations are made to calculate the CPSD between any two points on the restrictor surface.

A schematic illustration of the approximate method to calculate the CPSD at all combinations of points required in Equations 3.41 and 3.42 is shown in Figure 3.24. The CPSD between any two points along the radial direction can be calculated based on the arrangement in Figure 3.16(c). As the surface pressure is axi-symmetric, the measured cross spectra along the radial direction therefore applies to all circumferential angles θ. For the cross spectra between two points at different radial locations is approximated by the cross spectrum between the two points with the closest separation distance, which is not in the radial direction (due to high CPSD along the radial direction), as shown in Figure 3.24. For example, consider the calculation of the cross spectrum between point T_4 and an arbitrary point T_i. The cross spectra between pressure tap T_3 and the pressure taps along the circumferential direction are first measured. A series of cross spectral values with different separation distances are therefore obtained. The cross spectrum between points T_3 and T_i is then assumed to be similar to the cross spectra between two points with closest separation distance. This approximation is accurate for three reasons. First, the variation of the cross spectrum of the surface pressure along the circumferential direction is small, suggesting a small error in the approximation. Second, the cross spectra tend to a constant level as distance increases, which is most likely due to the acoustic pressure contribution to the total pressure, which is coherent over a much larger distance than the hydrodynamic contribution. Third, the coherence between the pressure taps near the inner edge is higher than that near the duct wall, the coherence between the pressure taps along the middle line of the restrictor is assumed to be the average coherence of the two sides. Using this approximation the cross spectra between any two points can also be predicted. However, in practice it is only required between two points within an area over which the surface pressure is coherent. This area will be calculated in the next section.

Due to flow noise, the sound field calculated from Equation 3.41 was compared with the far-field sound power measurement. A representative comparison at different flow speeds

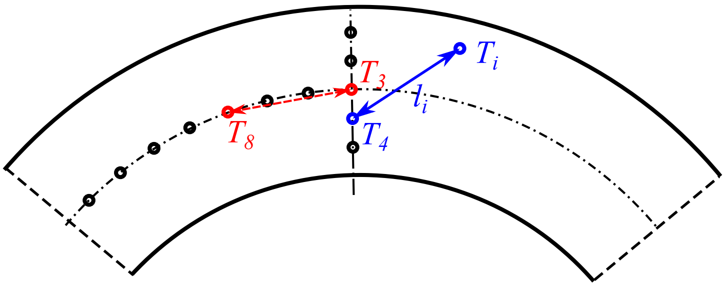

FIGURE 3.24: Illustration of the approximate calculation method of the surface pressure cross spectrum density between any two points.

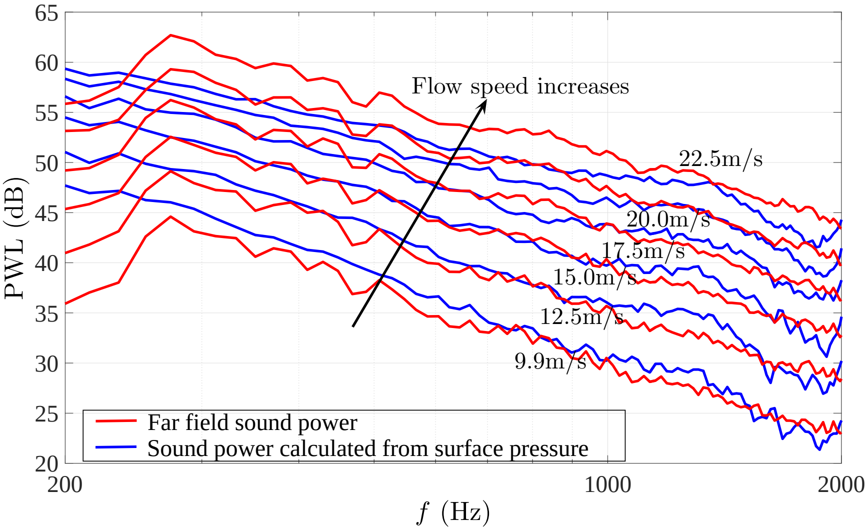

FIGURE 3.25: The comparison of PWL spectra from far field measurements and surface pressure measurements for the restrictor with an internal diameter of d=65mm under different mean flow speeds in the duct.

is shown in Figure 3.25. The red curves represent the sound power obtained from far-field sound measurements and the blue curves represent the sound power measurements based on the surface pressure from Equation 3.41. The agreement between two curves is better than 2 dB at frequencies above about 300 Hz at low flow speeds below 17.5 m/s. At higher flow speeds, 20.0 m/s and 25.0 m/s, agreement is poorer. The reason for this discrepancy is currently unclear.

3.6.2.4 Correlation area of surface pressure

The measured coherence results in figures 3.21 and 3.22 indicates that at a particular frequency, the surface pressure is only correlated over a small area, which we shall refer to as the correlation area. If we assume that the surface pressure PSD remains roughly constant within the correlation area the cross spectrum integrated over the surface required by Equation 3.39 can be approximated by

$$\int_{s'} S_{ff}(\mathbf{x}_s, \mathbf{x}_s', \omega) dS' = S_{ff}(\mathbf{x}_s, \omega) A_c(\mathbf{x}_s, \omega). \tag{3.47}$$

where $A_c(\mathbf{x}_s, \omega)$ is the correlation area.

Substituting Equation 3.47 into Equation 3.41 and letting $\bar{A}_c(\omega)$ denote the correlation area averaged over the restrictor surface yields the following relationship between the PSD of the noise averaged over a duct cross section, and $\bar{S}^-_{ff}(\omega)$ and $\bar{S}^+_{ff}(\omega)$, the surface pressures averaged over the upstream and downstream surfaces of the restrictor respectively,

$$\bar{A}_c(\omega) = \frac{\bar{S}_{pp}(\omega)}{\bar{S}^-_{ff}(\omega) + \bar{S}^+_{ff}(\omega)} \frac{4A^2}{A_r}. \tag{3.48}$$

The average correlation area calculated from Equation 3.48 for different flow speeds are plotted in Figure 3.26. The correlation length may be approximately calculated from $l_c(\omega) \propto \sqrt{\bar{A}_c(\omega)}$ and is about 1.6 cm at 1000 Hz at a mean flow speed of 9.9 m/s in the plane wave frequency range. This distance is significantly greater than the separation distance between the pressure taps.

Nelson and Morfey[47] suggested that the correlation length should vary as $l_c \propto U/f$ and hence the correlation area as $A_c \propto U^2/f^2$. In Figure 3.27, the sound power, surface pressure and correlation area from Equation 3.48 integrated over the plane wave frequency range are plotted versus Mach number. The sound power in this frequency bandwidth can be seen to obey a $U^{5.7}$ scaling law and the surface pressure a $U^{3.9}$ scaling law. This suggests from Equation 3.48 gives a scaling law for the correlation area of $U^{1.8}$ which is consistent with Nelson and Morfey's assumption of U^2. However, Figure 3.26 does not show the f^{-2} dependence for the correlation area predicted by Nelson and Morfey.

3.6.2.5 Sound source distribution on the surface of the restrictor

Equations 3.41 and 3.42 can be used to determine the source distribution over the surface of the restrictor. The sound source distribution for the plane wave and higher order modes is shown in Figure 3.28 and 3.29 respectively. Over the frequency range in which only plane waves can propagate, surface pressure fluctuations on the upstream surface of the restrictor are slightly larger than on the downstream side and are therefore mostly responsible for sound generation. On both sides of the restrictor, the surface pressure fluctuations near the duct wall contributes most to the sound field. Above the first cut-on frequency, however, upstream surface pressure fluctuations are greater than on the downstream side and mostly concentrated near the inner edge of the restrictor.

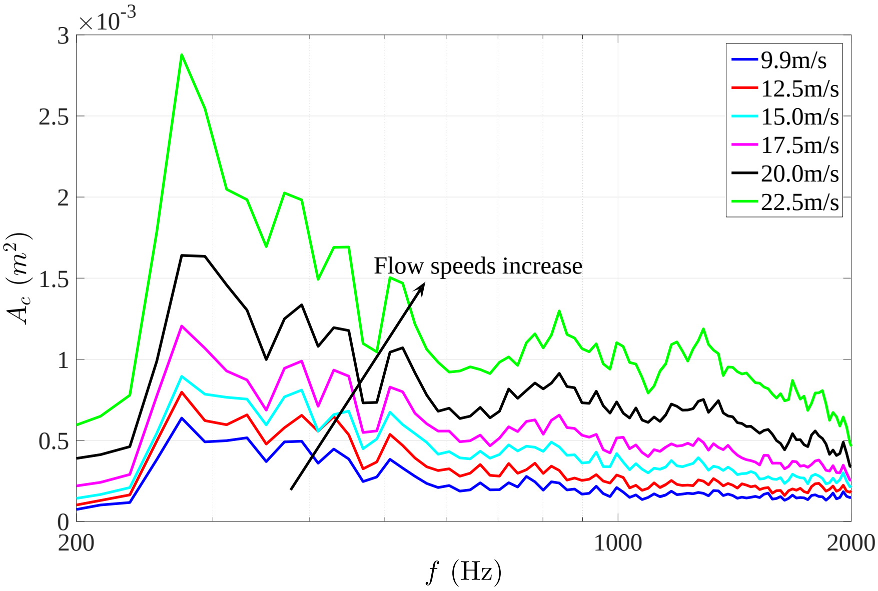

FIGURE 3.26: The average correlation area in plane wave frequency range for the restrictor with an internal diameter of d=65mm under different mean flow speeds in the duct.

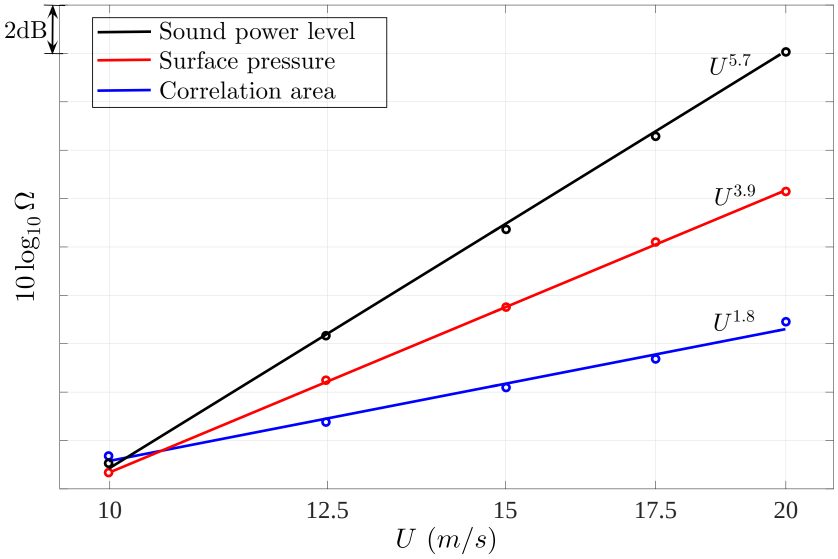

FIGURE 3.27: Different velocity scaling laws for sound power, surface pressure and correlation area, Ω represents sound power, sound pressure and correlation area integrated over 500-2000 Hz respectively.

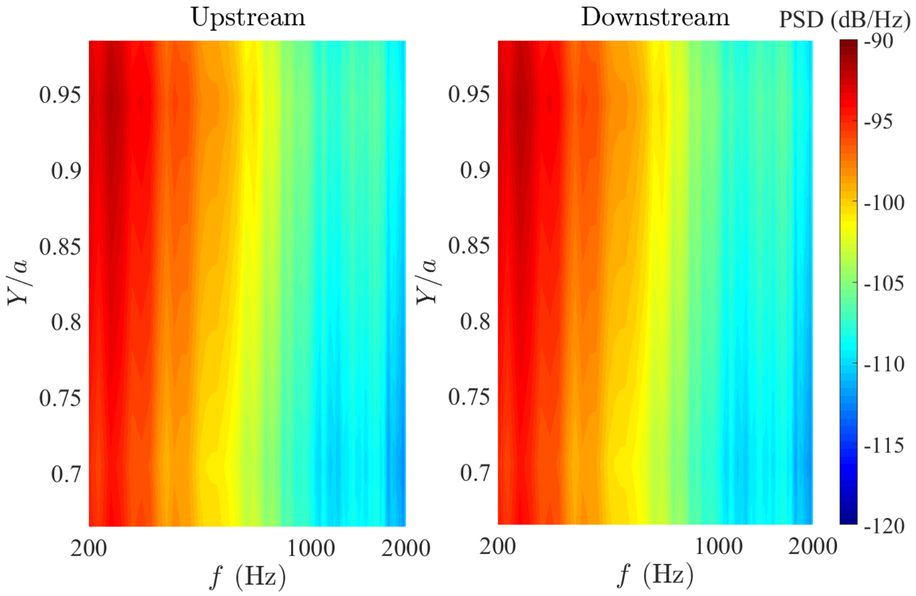

FIGURE 3.28: Sound source distribution on the surface of the restrictor for the plane wave. The test case is for an internal diameter of 65 mm under a mean flow speed of 10.0 m/s.

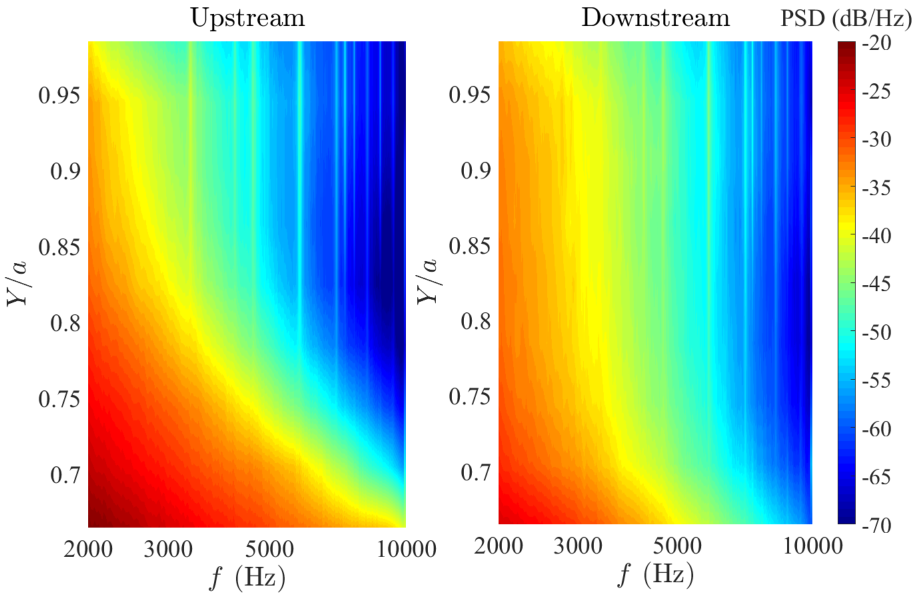

FIGURE 3.29: Sound source distribution on the surface of the restrictor for the higher order mode. The test case is for an internal diameter of 65 mm under a mean flow speed of 10.0 m/s.

3.7 Summary

In this chapter, the aerodynamic and acoustic properties in an empty duct and a duct with a single hole restrictor have been investigated experimentally. The surface pressure of the restrictor has been measured and a model for the relationship between pressure fluctuations on the restrictor surface and the radiated noise has been developed. The principal findings presented in this chapter may be summarized as follows:

- Compared to the acoustic field generated by a restrictor, the acoustic field generated by the turbulent flow in an empty duct is very low. In an empty duct, the aerodynamic pressure fluctuation is dominant.
- The static pressure drop across an single hole restrictor can be collapsed using the dynamic pressure $\frac{1}{2}\rho U^2$. Due to the high Reynolds number in this work, the influence of the mean flow speed on the drag coefficient of the restrictor can be ignored.
- The wall pressure fluctuation upstream of the restrictor is low. The flow downstream of the restrictor acts like a confined jet. The highest flow speed occurs along the centre line of the duct. The highest turbulence intensity occurs in the shear layer. The recovery of the flow downstream of the restrictor is slow.
- The highest surface pressure fluctuation is found to occur at the inner corner of the restrictor on the upstream side. The surface pressure fluctuations obey a U^4 velocity scaling law. Following a U^6 velocity scaling law of the sound power, the correlation area of the surface pressure follows a U^2 velocity scaling law.
- Experimental results show that the surface pressure fluctuations of the restrictor is the main noise source of the sound field in the duct, even though the highest pressure fluctuations occur at the reattachment point on the duct wall downstream of the restrictor. Wall pressure fluctuations on the duct wall downstream of the restrictor are therefore much less important than the restrictor itself.

Chapter 4

Sound power prediction of single-hole restrictor based on pressure drop

In this chapter, a model for the prediction of the sound power generated by a single-hole restrictor is presented. The model is based on the idea first proposed by Gordon in which the unsteady force acting on the restrictor is assumed to be directly proportional to the steady hydrodynamic force acting on the restrictor caused by drag mechanisms. Thus, the basic principle is a similarity between the unsteady and steady forces. The steady force can be deduced from the pressure drop acting across the restrictor. As discussed in the review in Chapter 1, the basic theory developed by Gordon was extended by Nelson and Morfey in 1981 [47] and recently updated by Kårekull [34]. It is shown in this thesis that all three methods do not satisfactorily predict the noise power of the restrictors investigated in this thesis. A refinement to the basic Gordon model are therefore presented that provides greater prediction accuracy. The previous models [17, 18, 33, 34, 47] are reviewed and discussed.

In this Chapter the sound power of the restrictor noise is obtained from measurements of the far field radiated sound pressure. The sound power spectra are compared to predictions obtained from the previous models based on pressure drop across the restrictor and again with that predicted using the new model. The new model will be shown to provide improved prediction accuracy compared with previous models. The model will be used to perform a parameter study of the noise generation in terms of the restrictor geometry.

4.1 Previous models for the restrictor noise prediction

In this section the previous models for the restrictor noise prediction based on pressure drop across the restrictor are introduced. In the next section these models are used to attempt to collapse the measured data.

4.1.1 Gordon's model

To investigate the noise generated by different in-duct elements installed near the end of the duct, Gordon [17] developed a model based on the measurement of the pressure drop across the in-duct elements. In his experimental arrangement, the in-duct elements were installed between 0 and 3.2 duct diameters from the end of the duct. The pressure drop in Gordon's model therefore assumed that the downstream side of the pressure was open to atmospheric pressure. In the current work the restrictor is assumed to be located within an infinite length duct so that the influence of the duct cannot be ignored. Gordon's model is not valid to predict the restrictor noise in the current work. However, his model will be modified in the next section to predict the noise due to restrictor well away from the end of the duct end.

When an in-duct element is placed in a duct carrying a mean flow, it exerts an unsteady force $F(t)$ acting on the fluid due to the unsteadiness of the flow around it. This unsteady force generates noise, which is then transmitted down the duct. The total time varying force distribution $F(t)$ can be expressed as the sum of a steady component and a time varying unsteady component that acts as the noise sources

$$F(t) = F + F^{'}(t), \tag{4.1}$$

where F is the steady hydrodynamic drag force, and $F^{'}(t)$ is the perturbation of the force.

The total time averaged sound power W (integrated over all frequencies) radiated into free field due to an unsteady compact force distribution was derived by Ribner [53] and is given by,

$$W \propto \overline{\left(\frac{\partial F}{\partial t}\right)^2} \frac{1}{\rho c_0^3}. \tag{4.2}$$

In Gordon's model, this free field compact source expression for the sound power prediction was used to estimate the in-duct sound power. The duct is therefore assumed to have no effect on the radiated sound power. His model also assumed that there is proportionality between the unsteady force and the steady force. With this assumption, the sound generated by the unsteady force can be related to the steady hydrodynamic force. In Equation 4.2, when retarded time effects are ignored, for noise sources due to fluctuating forces acting on the restrictor, Equation 4.2 may be rewritten as

$$W = K_G \frac{F^2 \bar{f}^2}{\rho {c_0}^3}, \tag{4.3}$$

where it is assumed that the force fluctuates at some characteristic frequency $\bar{f}$, ρ is the mean air density and K_G is a frequency-independent constant. The steady hydrodynamic force F was calculated from the pressure drop across the in-duct element. As the in-duct element was installed close to the end of the duct, Gordon assumed that the pressure downstream of the in-duct element equals the atmosphere pressure. The characteristic frequency of the unsteady force $\bar{f}$ was assumed to be dependent on the characteristic length of the in-duct element.

Although Equation 4.3 provides an estimate of the *total* sound power generation, it may also be applied to the sound power within frequency bands, such that now K_m varies with the frequency f. The generalisation of Equation 4.3 to a spectral density in unit frequency bands $W(f)$ is of the form

$$W(f) = K_G(f) \frac{F^2 \bar{f}^2}{\rho {c_0}^3}, \tag{4.4}$$

where $K_G(f)$ is the corresponding constant that we analyse in detail in Section 4.2.3.

4.1.2 Nelson and Morfey's model

Based on the same assumptions as Gordon's, namely that the root mean square (RMS) fluctuating (*total*) force acting on the in-duct element is proportional to the steady force, Nelson and Morfey developed a model to predict the sound power of noise generation by in-duct elements in a rectangular duct. In their model, the in-duct element is assumed to be installed in an infinite duct. Duct propagation effects on the sound power radiation are therefore included. Different expressions were developed for the frequency ranges below the first cut-on frequency where only plane wave mode can propagate and above the first cut-on frequency where many higher order modes are propagating.

Nelson and Morfey expressed sound power $W(f)$ for different frequency ranges. In the frequency range where only plane waves are able to propagate, the PSD of transmitted sound power is given by

$$W(f) = \frac{1}{4A\rho c_0} S_{FF}(f), (f < f_0). \tag{4.5}$$

At frequencies above the first cut-on frequency for a rectangular hard walled duct, where higher order modes are able to propagate, the sound power spectrum is given by

$$W(f) = \frac{k^2}{24\pi\rho c_0}\left(1 + \frac{3\pi}{4k}\frac{b_1 + b_2}{A}\right) S_{FF}(f), (f > f_0), \tag{4.6}$$

where $S_{FF}(f)$ is the PSD of the total fluctuating force acting on the in-duct element, A is the cross-sectional area of the duct, b_1 and b_2 are the cross-sectional length and width, k is the acoustic wave number, and f_0 is the cut-on frequency of the first transverse duct mode. The terms in front of S_{FF} represent the effects of the duct on the sound power radiation. Integrating the PSD of the total fluctuating force in the frequency band Δf with centre frequency of f_c gives

$$\int_{f_c - \Delta f/2}^{f_c + \Delta f/2} S_{FF}(f) df = (F_{rms})^2, \tag{4.7}$$

where F_{rms} is the RMS force in the frequency band Δf. It is assumed that the RMS fluctuating force is proportional to the steady force in a frequency band Δf. In each unit frequency band, the RMS force is give by

$$(F_{rms}(f))^2 = K_{NM}(St)(F^2), \tag{4.8}$$

where F is the total steady drag force, the Strouhal number $St = \frac{fU}{L}$ is defined in terms of the characteristic length L of the in-duct element. However, we show in Section 4.3 that this Strouhal dependence is not observed in the experimental results and the collapse of the spectra is obtained by plotting against absolute frequency f. The definition of frequency dependent constant $K_{NM}(St)$ here is defined to be slightly different from Nelson and Morfey's original work by taking the square value of Nelson and Morfey's definition to be consistent with other work discussed in this chapter.

For the element in a duct, the mean drag force can be written in terms of Δp, the static pressure drop across the in-duct element is

$$F = A\Delta p, \tag{4.9}$$

where A is the area of the duct cross-section.

Equations 4.5 and 4.6 can then be expressed in terms of pressure drop as

$$W(f) = K_{NM}(St)\frac{A}{4\rho c_0}(\Delta p)^2, (f < f_0), \tag{4.10}$$

and

$$W(f) = \frac{k^2 A^2}{24\pi\rho c_0}\left(1 + \frac{3\pi}{4k}\frac{b_1 + b_2}{A}\right)(\Delta p)^2, (f > f_0), \tag{4.11}$$

where the term in curly brackets in Equation 4.11 arises from the high frequency density of modes in the rectangular duct.

Nelson and Morfey's model was derived for a rectangular duct. To predict the noise generation by different in-duct elements in a circular duct, Oldham and Ukpoho [48] rewrote Nelson and Morfey's expression for a circular duct as

$$W(f) = K_{NM}(St)\frac{A}{4\rho c_0}(\Delta p)^2, (f < f_0) \tag{4.12}$$

and

$$W(f) = \frac{k^2 A^2}{24\pi \rho c_0}\left(1 + \frac{3\pi}{4rk}\right)(\Delta p)^2, (f > f_0), \tag{4.13}$$

where a is the radius of the duct. In the next section, Oldham and Ukpoho's model based on Nelson and Morfey's model is used to attempt to collapse the measured data from the current work.

4.1.3 K*å*rekull's model

Kårekull has adopted the same model as Nelson and Morfey by computing the steady drag force acting on the orifice plate from the momentum flux instead of from $F = A\Delta p$ the pressure drop. In his paper he states that the latter is inaccurate when the element dimensions are much smaller than the duct although he does not explains the reason for this. To compute the drag, Kårekull exploits the proportionality between the drag force and the momentum flux, i.e.

$$F \propto \rho_0 AU \cdot U_{vc} = \frac{\rho A U^2}{\sigma}, \tag{4.14}$$

where U is the mean flow velocity in the duct and U_{vc} is the mean flow velocity at the vena contracta, and σ is the vena contracta ratio given by

$$\sigma = \frac{\frac{A_j}{A}}{1 + \sqrt{\frac{1}{2}(1 - \frac{A_j}{A})}}, \tag{4.15}$$

where A_j is the open area of the in-duct element. With the expression of the drag force of Equation 4.14, Kårekull's model for the prediction of the sound power spectra for a circular duct is given by

$$W(f) = K_K(St)\frac{\rho A}{2c_0\sigma^2}U^4, (f < f_0) \tag{4.16}$$

and

$$W(f) = K_K(St)\frac{\rho A^2 k^2}{12\pi c_0 \sigma^2}\left(1 + \frac{3\pi}{4rk}\right)U^4, (f > f_0). \tag{4.17}$$

Kårekull's model is developed for a restrictor with small internal diameter such as in restrictors comprising multiple small holes. In the current work, the internal diameters of the restrictor are comparable to the duct dimensions. However, for completeness we compare Kårekull's prediction to our experimental data. Meanwhile, in section 4.3.4, Kårekull's method for computing the steady drag force acting on the restrictor is also discussed.

4.2 New model for restrictor noise prediction

The various models outlined above for predicting the noise from the in-duct elements are applied to attempt to collapse the measured data in this work in the next section, and have been shown to provide poor predictions of the noise spectra. In this section, a new model based on the pressure drop method is developed to predict the noise spectra due to the single hole restrictor.

Gordon's model for the predictions of in-duct element self-noise assumes that the static pressure downstream of the in-duct element is the same as atmosphere pressure, which is only accurate for in-duct elements installed close to, or at the end of the duct, as was the case in his experimental arrangement (less than 3.2-duct diameters). However, this assumption is not accurate when the in-duct element is installed well away from the end of the duct. We now follow his general approach for the predictions of restrictor self-noise based on the steady force F acting across the restrictor and the characteristic frequency $\bar{f}$ in Equation 4.4.

4.2.1 Calculation of the steady force

The steady drag force acting on the restrictor can be calculated from the pressure drop across it. A schematic of the restrictor installed in a duct is shown in Figure 4.1. The pressure drop was measured between two reference planes, one upstream and one downstream of the restrictor, shown as reference planes 1 and 2 in figure 1. The flow speed at a third reference plane (marked 3 in figure 1) located immediately downstream of the restrictor, was used to compute the characteristic frequency from $\bar{f} = U_3/L$. The static pressures and mean flow speeds at the three reference planes are denoted here by p_1, U_1, p_2, U_2, p_3, U_3 respectively. The density variation of the air in the duct is ignored.

The mean drag force acting on the restrictor is given by the product of the static pressure drop across it and the duct cross sectional area, as given by Equation 4.9. The pressure drop between the reference plane 1 and the reference plane 2 can be expressed in terms of the drag coefficient of the restrictor C_d as shown in Euqation 3.20. Substituting

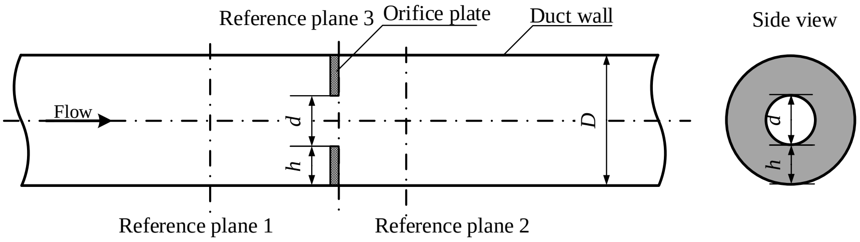

FIGURE 4.1: Schematic illustration of an restrictor in a duct.

Equation 3.20 into Equation 4.9 yields the following expression for the mean drag force action on the restrictor,

$$F = C_d \frac{1}{2} \rho U^2 A. \tag{4.18}$$

4.2.2 Calculation of characteristic frequency of unsteady force

The characteristic frequency $\bar{f}$ of the unsteady force is obtained from the characteristic length L of the restrictor and the mean flow velocity at the reference plane 3,

$$\bar{f} \propto \frac{U_3}{L},$$

The mean flow velocity at reference plane 3 can be calculated from the mean flow speed well upstream of the restrictor U and the duct area A assuming mass conservation

$$AU_1 = A_j U_3. \tag{4.19}$$

The height h of the orifice plate is one of the main factors that controls the behaviour of the flow around the restrictor and is therefore selected as the characteristic length of the restrictor. Thus, $\bar{f}$ can be predicted by combining the three results above to give

$$\bar{f} \propto \frac{A}{A_j h} \sqrt{\frac{2\Delta p}{\rho C_d}}.$$

4.2.3 New model

Considering Equation 4.4, for the steady force acting on the restrictor of Equation 4.18 and for the characteristic frequency of the unsteady force field, the final equation for the sound power due to the restrictor can be written as

$$W(f) = K_m(f) \frac{\rho}{4 c_0{}^3} C_d^2 \frac{A^4}{A_j^2} \frac{1}{h^2} U^6, \tag{4.20}$$

where $K_m(f)$ is a frequency dependent constant corresponding to the constant $K_G(f)$ in Gordon's model. Equation 4.20 can be re-expressed in term of the restrictor diameter ratio

$$\beta = \frac{d}{D}, \tag{4.21}$$

where d is the internal diameter of the restrictor and D is the duct diameter,

$$W(f) = K_m(f)\frac{\rho}{4{c_0}^3}C_d^2\frac{\pi^2 a^2}{(1-\beta)^2\beta^4}U^6. \tag{4.22}$$

Equation 4.22 is now expressed in terms of easily measurable parameters, together with the frequency dependent constant $K_m(f)$. The sound power level in a unit frequency band can therefore be non-dimensionalised as

$$10\log_{10} K_m(f) = PWL(f) - 10\log_{10}\left[\frac{\rho}{4{c_0}^3}C_d^2\frac{\pi^2 a^2}{(1-\beta)^2\beta^4}U^6\right] - 120, dB \tag{4.23}$$

where $a = D/2$ is the duct radius, and $PWL(f)$ is the sound power level in a unit frequency band. According to Equation 4.22, the sound power obeys a U^6 power law. One interpretation of K_m in Equation 4.22 is that it represents a universal non-dimensional power spectrum that is valid for moderate values of β at low Mach number flows. In this work, the range of the β is from 0.5 to 0.8 and the maximum mean flow speed is 25 m/s.

The sound power generation per unit area of the restrictor area A_r can be written in terms of β as

$$\frac{W(f)}{A_r} = K_m(f)\frac{\rho\pi U^6}{4{c_0}^3}C_d^2 H(\beta), \tag{4.24}$$

where $H(\beta)$ is a non-dimensional function that is only a function of the restrictor diameter ratio, defined by

$$H(\beta) = \frac{1}{\beta^4(1+\beta)(1-\beta)^3}. \tag{4.25}$$

Equation 4.24 shows that the noise generation by the single hole restrictor is a complicated function of the restrictor dimensions and determined by $C_d^2 H(\beta)$, where C_d is an easily measured drag coefficient. It can also be calculated through the relationship between the discharge coefficient and the drag coefficient which is given by

$$C_d = \frac{1}{C_{dis}^2}\frac{1-\beta^4}{\beta^4}, \tag{4.26}$$

where C_{dis} is the discharge coefficient of the restrictor which can be calculated through the Reader-Harris Gallaghter Equation [1],

$$\begin{aligned} C_{dis} = 0.5961 + 0.0261\beta^2 - 0.216\beta^8 + 0.000521\left(\frac{10^6\beta}{Re}\right)^{0.7} \\ +(0.0188 + 0.0063M_1)\beta^{3.5}\left(\frac{10^6}{Re}\right)^{0.3} \\ +(0.043 + 0.080e^{-10Lu} - 0.123e^{-7Lu})(1 - 0.11M_1)\frac{\beta^4}{1-\beta^4} \\ -0.031(M_2 - 0.8M_2^{1.1})\beta^{1.3}. \end{aligned} \tag{4.27}$$

where Re is the Reynolds number based on the duct diameter, Lu is the distance between the restrictor and the upstream pressure tap. The term M_1 is a function of β and Re,

$$M_1 = \left(\frac{19000\beta}{Re}\right)^{0.8}. \tag{4.28}$$

and M_2 is a function of β and L_d which is the distance between the restrictor and the downstream pressure tap,

$$M_2 = \frac{2L_d}{1-\beta}. \tag{4.29}$$

The discharge coefficient is observed to become independent of Reynolds number (with respect to the duct diameter) at Reynolds numbers larger than about 20000. The predicted discharge coefficient from Equation 4.27 for different restrictors under different flow speeds is plotted in Figure 4.2, which shows a variation of less than 0.03.

In our experimental rig, a mean flow speed of 10 m/s corresponds to a Reynolds number of approximate 72000. The effect of the mean flow speeds on the discharge coefficient is therefore small. Figure 4.3 shows a comparison of the predicted drag coefficient versus β at the four mean flow speeds of 10 m/s, 15 m/s, 20 m/s and 25 m/s obtained from Equation 4.26 with the measured drag coefficient obtained from the pressure drop averaged over the four flow speeds. It clearly shows that the mean flow speed has negligible effect on the drag coefficient.

In a specific experimental arrangement, L_u and L_d are both fixed. If the effect of the Reynolds number is ignored, the expression for the drag coefficient in Equation 4.26 is determined only by the restrictor diameter ratio β through the term $\frac{1-\beta^4}{\beta^4}$. Combining this term with Equation 4.25, the overall effect of β on the restrictor noise can be predicted. Figure 4.4 is a plot of the term $C_d^2H(\beta)$ which quantifies the dependence of the noise generation efficiency on β. It shows that the sound generation by the restrictor is significantly affected by changes in the internal diameter. As the internal diameter

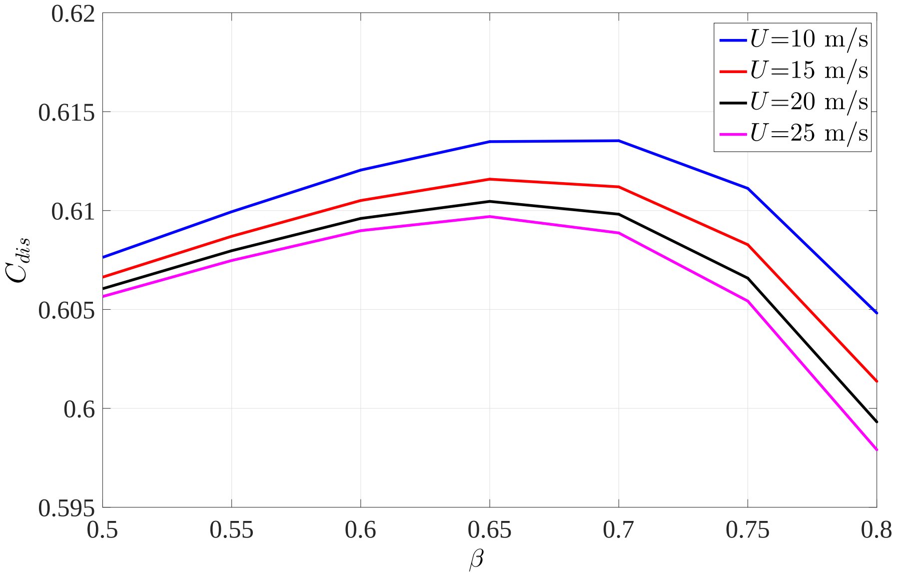

FIGURE 4.2: Calculated discharge coefficient for different restrictors under different mean flow speeds.

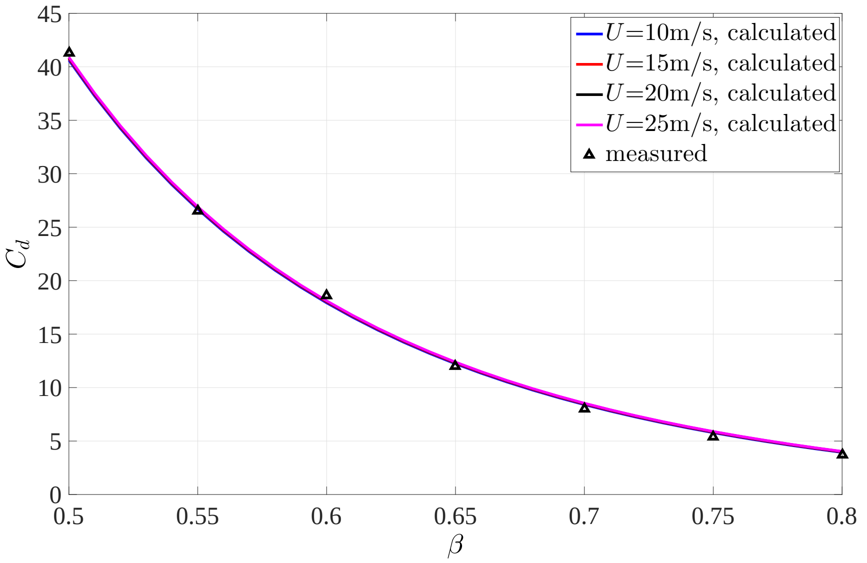

FIGURE 4.3: The comparison of the measured and calculated drag coefficient.

of the restrictor becomes smaller, the sound increases significantly. When the restrictor is absent , $\beta \rightarrow 1$ and the sound generation is predicted to be zero. The ratio β of the restrictors investigated experimentally in this work is 0.5-0.8 based on commonly used restrictor in an ADS, corresponding to about 16 dB change in sound power transmission in the duct according to Figure 4.4.

Equation 4.26 allows the drag coefficient of the restrictor to be obtained without measurement. The only input parameter needed in Equation 4.22 is the restrictor dimension.

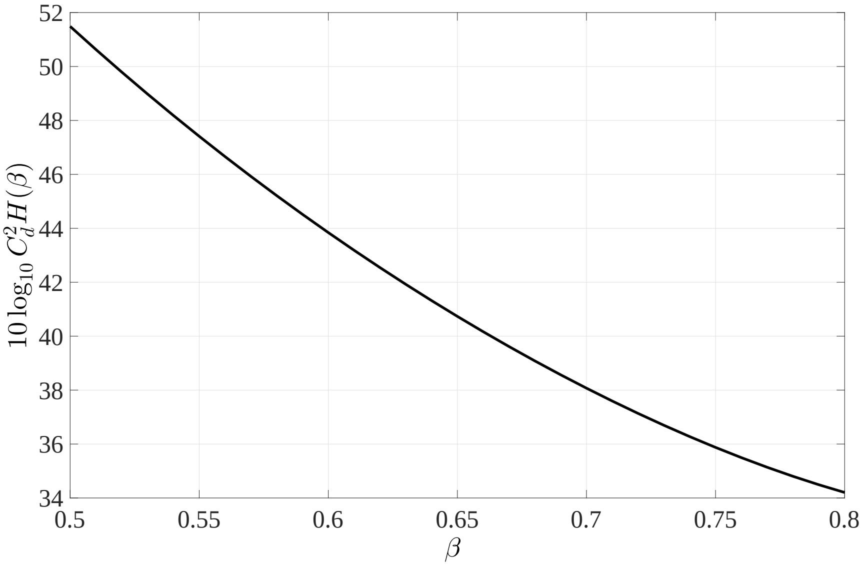

FIGURE 4.4: Variation of the sound power generation due to the change of ratio between the internal diameter of the restrictor and the duct diameter.

However, Equation 4.22 can only be applied to predict the noise generation by the restrictor and cannot be applied to predict the pressure drop. In a real ADS, the restrictor is used to obtain a pressure drop to adjust the flow rate. The pressure drop is usually measured 10 diameters upstream and downstream of the restrictor to make sure the flow is fully recovered. The calculated drag coefficient from Equation 4.26 is based on a situation in which the flow is not fully recovered and therefore cannot be applied to calculated the real pressure drop provided by the restrictor.

4.3 Sound power measurement

In this work the sound power measurements were made from acoustic pressure measurements both inside and outside of the duct. In the duct, the acoustic pressure can be expressed in terms of a series of acoustic modes and the sound power calculated from the determination of the mode amplitudes. In this section, based on the modal analysis technique described in the last chapter, the sound power is calculated. As only spinning modes can be resolved from the arrangement of microphones at the duct wall from the modal analysis, the in-duct sound power calculation is only performed up to 4183 Hz, which is the cut-on frequency of the first radial mode. The in-duct sound field radiates efficiently from the end of the duct only above 185 Hz corresponding to the cut-off frequency of the flare, and at frequencies not too close to the modal cut-on frequencies where the modal reflectivity is very high. The far-field sound power measurement therefore can be performed in the anechoic chamber at the end of the duct at all frequencies except below 185 Hz and at the cut-on frequencies. The frequency range of the far-field sound power measurement is 200-10000 Hz. The in-duct sound power is now compared to the far field sound power estimate to verify the accuracy of the sound power measurement procedure.

4.3.1 Experimental arrangement

The experimental arrangement for performing far-field sound power measurements is shown in Figure 4.5. The measurements were made using a single polar array of microphones and assuming that the radiated sound field is axi-symmetric. The microphone array was located within a small enclosure in which sound absorbing wedges were attached to the wall to simulate free field condition. The wedges have a cut-off frequency of 250 Hz. The array comprises a total of 10 FG-3329-P07 microphones from Knowles Electronics. It was situated over an arc at a 1 m radius from the centre of the flare, as shown in Figure 4.5. The 10 microphones were equally spaced over an angular range of $5^\circ < \theta_m < 85^\circ$, in 9° interval. The microphones were calibrated using a B&K 4321 calibrator. Windscreens are attached on the top of the microphone to reduce the effect of the flow on the acoustic measurements. The data were sampled using a 24-bit National Instruments data acquisition system at a frequency of 20 kHz giving an upper frequency measurement limit of 10000 Hz. The cut-off frequency of the flare is 185 Hz and the cut-off frequency of the anechoic space is 250 Hz. The minimum frequency plotted in this chapter is therefore 250 Hz. Since below this frequency, reflections back into the duct can no longer be ignored. The noise from the restrictor at frequencies above 10000 Hz was found experimentally to be very low.

For axi-symmetric sound pressure radiation, the sound power can be calculated from

$$W(f) = \frac{2\pi R^2}{\rho c_0} \int_{0^\circ}^{90^\circ} S_{pp}(\theta, f) \sin\theta d\theta, \tag{4.30}$$

where R is the distance between the sound source and the measured position, θ is the position of the measured point. For the discrete microphone positions, Equation 4.30 reduces to,

$$W(f) = \frac{2\pi R^2}{\rho c_0} \sum_{n=1}^{N} S_{pp}(\theta_n, f) \sin\theta_n \Delta\theta, \tag{4.31}$$

where N is the total number of the microphone, $\Delta\theta$ is the angle interval between two microphones, θ_n represents the positions of the microphones.

A series of restrictors with different internal diameters ranging between 50 mm and 80 mm were selected for investigation. The static pressure drop across the restrictor was measurement using two pressure taps mounted on the duct wall 0.1 m upstream and 0.05 m downstream of the restrictor according to ISO 5167 [1]. The static pressure was measured using a FCO520 pressure meter manufactured by Furness Controls. The drag coefficient of the restrictor can be calculated from Equation 3.20. The mean flow speed

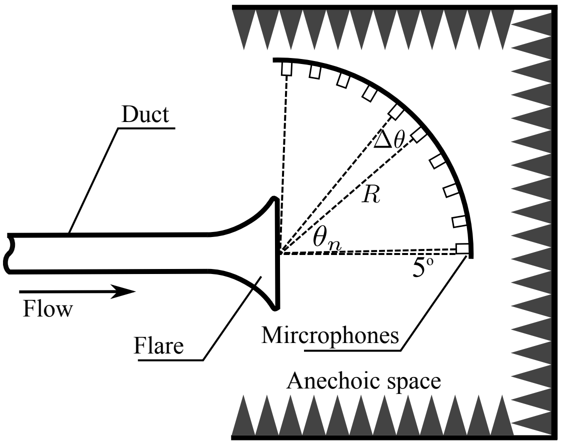

Figure 4.5: Experimental arrangement for the far field sound power measurements.

Table 4.1: Restrictor measurement cases

d (mm)	β	h (mm)	C_d	Mean flow velocity (m/s)
50	0.50	25	34.2	7.2-16.0
55	0.55	22.5	20.5	10.6-20.2
60	0.60	20	13.4	9.8-23.8
65	0.65	17.5	7.91	10.6-25.5
70	0.70	15	4.7	10.3-25.1
75	0.75	12.5	2.7	10.1-25.1
80	0.80	10	1.6	10.2-25.3

in the duct was determined from the fan speed and the size of the restrictor. The mean flow speed investigated ranges from 7.2 m/s to 25.5 m/s. However, it found to be difficult to obtain a large mean flow speed for restrictors with small internal diameters. The flow speeds for the restrictor with small internal diameter vary within a narrow range. The noise and pressure drops for a total of 48 test cases with different combinations of the restirctor dimensions and mean flow speeds were measured. The detailed test cases are presented in Table 4.1.

4.3.2 In-duct sound power measurement

In this section the sound power transmitted in the duct as a function of frequency is determined by first determining the amplitudes for all the modes that can be resolved using the single ring of microphones, as described in Section 3.5. The total sound power can be deduced from the sum of the sound powers in each mode. The sound power in each mode can be determined according to the theory set out below.

The axial particle velocity in a cylindrical hard-walled duct is given by

$$u_z(r,\theta,z) = -\frac{1}{i\omega\rho}\frac{\partial p(r,\theta,z)}{\partial z}. \tag{4.32}$$

Differentiating Equation 3.4 for the acoustic pressure in each mode, the axial particle velocity can be expressed as

$$u_z(r,\theta,z) = \frac{1}{\rho c_0}\frac{k_{zmn}}{k}A_{mn}\frac{\mathrm{J_m}(k_{rmn}r)}{N_{mn}}e^{-i(m\theta+k_{zmn}z)}. \tag{4.33}$$

At a single frequency, and when the flow speed can be neglected, the axial sound intensity for a single mode is given by

$$I_z(r,\theta) = \frac{1}{2}\mathbf{Re}\{p^*_{mn}(r,\theta,z)u_z(r,\theta,z)\}. \tag{4.34}$$

Note that, in a duct without reflections, the axial intensity is independent of axial position along the duct, which is the case in the present duct above about 185 Hz.

Substituting Equations 3.4 and 4.33 into Equation 4.34 gives

$$I_{zmn} = \frac{1}{\rho c_0}\frac{k_{zmn}}{k}\frac{|\mathrm{J_m}(k_{rmn}r)|^2}{|N_{mn}|^2}\overline{|A_{mn}|^2}. \tag{4.35}$$

Integrating the sound intensity over the duct cross-section gives the sound power for a single mode W_{mn} as

$$W_{mn} = \frac{1}{2}\frac{1}{\rho c_0}\frac{k_{zmn}}{k}E\{|A_{mn}|^2\}, \tag{4.36}$$

where $E\{\}$ represents the expectation. Owing to the orthogonality of the Bessel functions, the overall sound power in the duct is the sum of the sound power of individual modes,

$$W = \sum_m\sum_n W_{mn}. \tag{4.37}$$

Using Equations 4.36 and 4.37, the in-duct sound power can be calculated from the measurements of the modal amplitude A_{mn} obtained through modal analysis results described in Section 3.5. A comparison between the measured in-duct sound power from Equation 4.37 and far-field sound power from Equation 4.31 is shown in Figure 4.6. Agreement of better than 1 dB is observed which confirms the accuracy of the far-field sound power measurements and the assumption of zero reflection. As only spinning

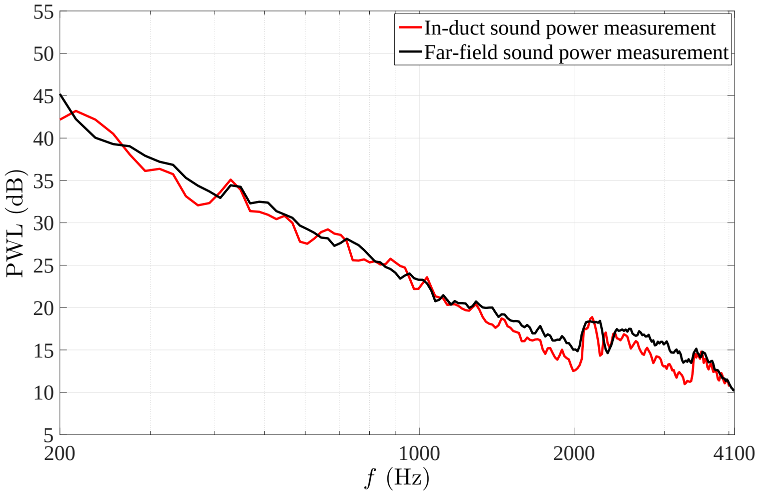

FIGURE 4.6: Comparison of in-duct sound power measurement and far-field sound power measurement for the restrictor with an internal diameter of 65 mm under a mean flow speed of 10.0 m/s.

modes can be resolved in this work, the upper frequency limitation of the in-duct sound power measurement is 4183 Hz, which is the cut-on frequency of the first radial mode. Due to the larger frequency range of the far-field sound power measurement, the following discussions will be based on the far-field sound power measurements.

4.3.3 Far field sound power measurement

In this section, the sound power of the restrictor noise is measured from the far-field radiated pressure assuming axi-symmetry. The measured sound power and the sound power predicted from the theories based on pressure-drop presented in Section 4.1, and the new model, are compared. The results in this section are presented both in terms of narrow band spectra and one-third octave band spectra to allow direct comparison with previous results.

The PWL spectra of the noise generated by the restrictor is shown in Figure 4.7(a) and the corresponding sound power level in one-third octave bands is shown in Figure 4.7(b) for a total of 48 different combinations of restrictors and flow speeds. The sound power level can be seen to vary by about 35 dB across all cases. An important observation of those results is that the spectra plotted against frequency (in Hz) are parallel to each other. Spectral shape is therefore maintained in all cases, suggesting that the only effect of the speed and the restrictor size is to apply a frequency independent scaling factor to the models presented in Section 4.2.3. This finding also indicates that collapse of the spectra can be obtained by plotting against frequency f in Hz, rather than Strouhal number as argued by the previous theories.

Below about 2010 Hz, when only the plane wave can propagate, the spectra plotted against frequency on a logarithmic scale exhibit straight line decay, suggesting a frequency power law, $W \propto f^{-2}$. Above 2010 Hz, higher order modes are excited and some

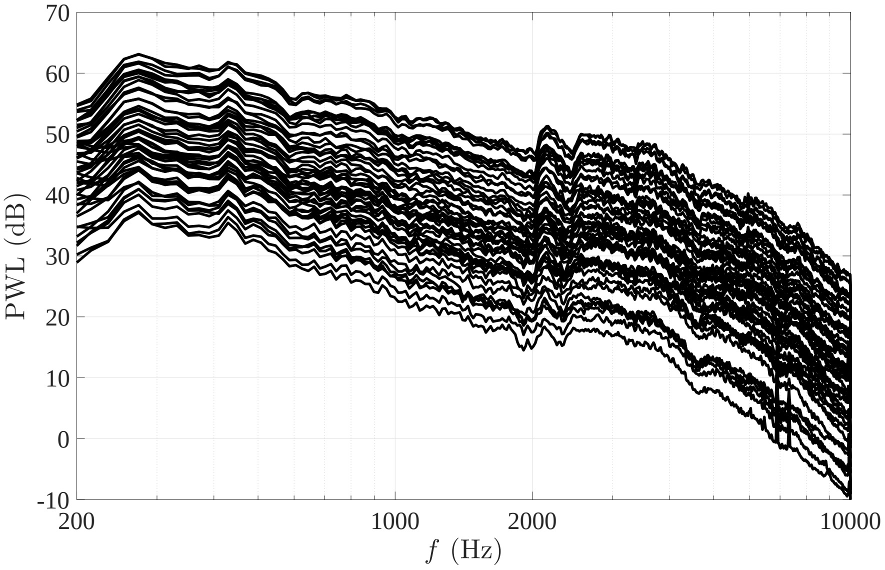

(a)

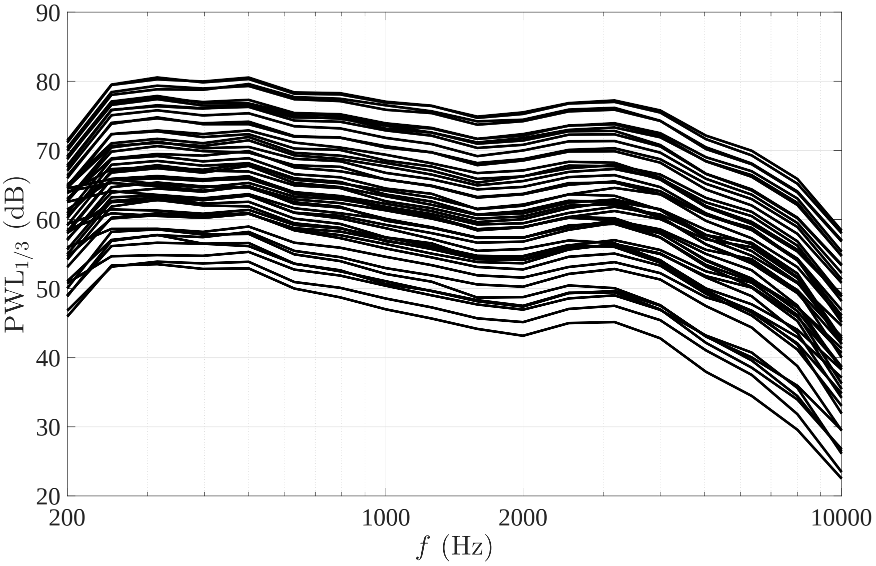

(b)

FIGURE 4.7: (a)PSD of sound power of the noise generated by restrictors with different internal diameters under different mean flow speeds, (b)Sound power level of the noise generated by restrictors with different internal diameters under different mean flow speeds (1/3 octave band).

'humps' appear in the spectra, corresponding to the cut-on frequencies. For the restrictors of different sizes, the relative amplitudes of the humps are slightly different. The noise spectra at the cut-on frequencies due to the restrictor with smaller internal diameter have larger amplitudes. This suggests that smaller restrictors are more efficient in exciting higher order modes. This results are consistent with the modal analysis result presented in Figure 3.15 in Chapter 3.

4.3.3.1 The velocity dependence of sound power

Nelson and Morfey suggested that the radiated sound power of the in-duct elements obeys a U^4 velocity scaling law at frequencies below the first cut-on frequency. At frequencies above the first cut-on frequency, due to the effect of higher order modes, the radiated sound power is predicted to have a U^6 velocity dependence. The velocity scaling law is also investigated in the current work.

Figure 4.8 is a graph of the variation in radiated sound power integrated over all frequencies for each restrictor versus mean flow speed plotted on a logarithmic scale. The data points are represented by the symbols and the straight line of best fit is shown as a dashed curve. The noise data shows that, over the entire frequency bandwidth, the sound power follows closely a well behaved power law of the form U^n. The exponent n varies with the orifice plate diameter around an average value of about $n = 6$ consistent with the prediction in Equation 4.22.

This procedure was repeated for the sound power in the frequency band below the first cut-on frequency between 250 Hz and 2000 Hz, and above the first cut-on frequency in the bands 2000 Hz to 3000 Hz when only a single higher order mode is present, and in the band 2000 Hz and 10000 Hz where multiple higher order modes are present. The index n in the velocity scaling law U^n for these cases is shown in Table 4.2. In general, the index n for the restrictor with smaller internal diameter is higher than for larger internal diameter. The reason for this may be due to the contribution to overall noise due to the jet flow through the restrictor which follows a U^8 power law. The flow velocity in the vena contracta of the smaller restrictor is much higher than for the larger restrictor. For the restrictors with internal diameters of between 50 mm and 80 mm, the velocity dependence varies between 4.8 to 6.7. These limits are either side of the U^6 scaling law predicted in Equation 4.22. The noise prediction formula of Equation 4.22 therefore represents an average behaviour which is therefore most likely to be in error for small diameter plates at high frequencies.

Table 4.2 shows that at frequencies below the first cut-on frequency, the velocity exponent n is smaller than that in the higher frequency band. At the frequencies between 2000 Hz and 3000 Hz, when only one higher order mode is excited, the velocity dependence n is typically an order 1 greater. This sensitivity of n to frequency bandwidth was also observed in the measured data presented by Nelson and Morfey.

4.3.3.2 Collapse of the sound power spectra using pressure-drop models

The expression for the sound power spectrum developed by Nelson and Morfey is equated to the measured sound power spectra presented in Figure 4.9 in order to determine the non-dimensional factor $K_{NM}(St)$. The non-dimensional spectrum $K_{NM}(St)$ is plotted in Figure 4.9 against Strouhal number, as proposed by Nelson and Morfey.

TABLE 4.2: Velocity dependence of the far-field sound power

d (mm)	Frequency range (Hz)			
	250-2000	2000-3000	2000-10000	250-10000
50	6.5	7.6	7.7	6.7
55	6.4	7.3	7.5	6.6
60	6.0	7.0	7.2	6.1
65	5.4	6.3	6.4	5.6
70	4.9	5.9	6.1	5.1
75	4.6	5.5	5.8	4.9
80	4.7	5.6	6.0	4.7

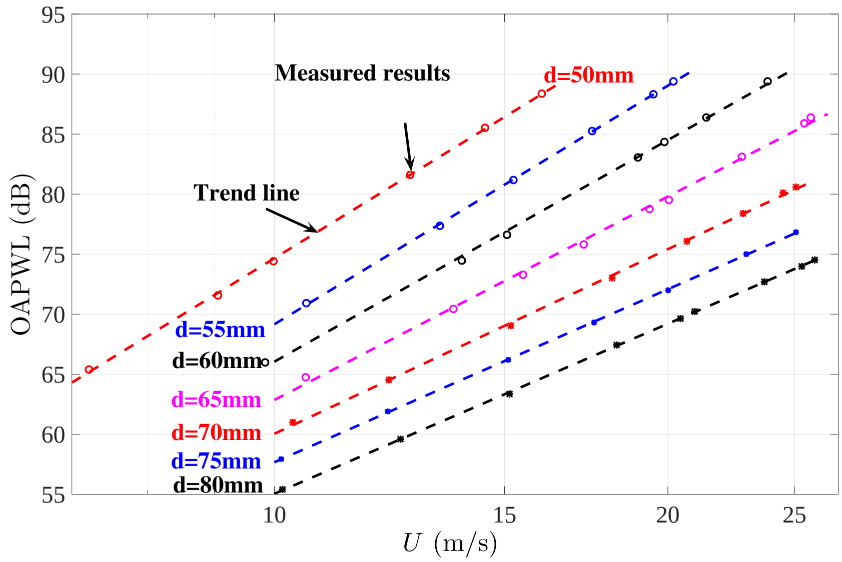

FIGURE 4.8: The velocity independence of the radiated sound power.

Collapse of the spectra at Strouhal numbers below about 6 is generally poor. A variation in spectra of up to about 15 dB is observed and plotting against Strouhal number causes the spectra to be shifted. However, above this Strouhal number good collapse of the spectra is obtained. In this frequency range, there are approximately 5 to 10 modes, which is consistent with the ‘high’ frequency modal density asymptotic approximation made by Nelson and Morfey.

The results from the application of Kårekull’s model to our cases in Table 4.1 are shown in Figure 4.10. Similar to the results of Nelson and Morfey’s model, the collapse against Strouhal number is poor. This may be because Kårekull’s model is developed for the restrictor with a small open ratio β (< 0.0053).

The non-dimensional spectra K_m defined in Equation 4.23 from the new model are presented in Figure 4.11. The results are presented both as narrow band spectra and in 1/3 octave bands. Below 4000 Hz, the data collapses to within about 7 dB. Above about 4000 Hz, the data collapse to within 10 dB. The results suggest that the approach incurs a prediction error of up to 10 dB.

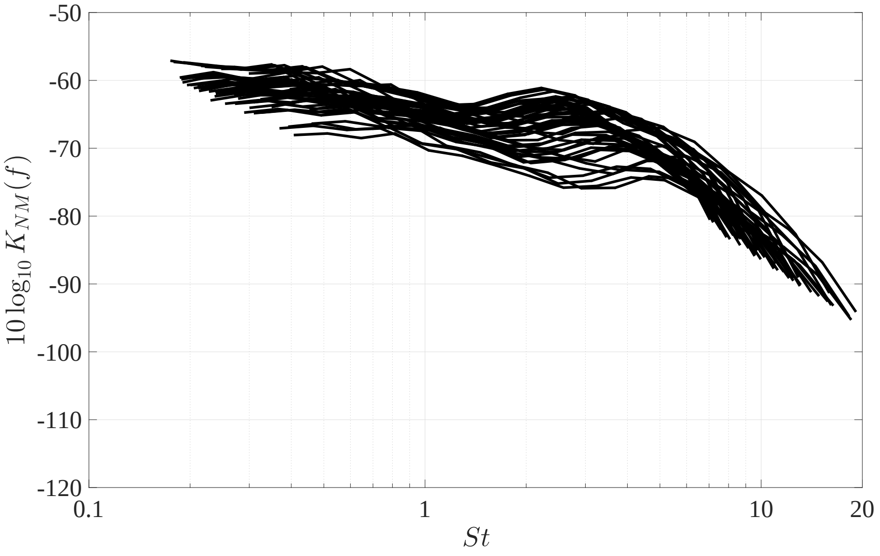

FIGURE 4.9: The general sound power spectra for restrictor noise from Nelson and Morfey's model.

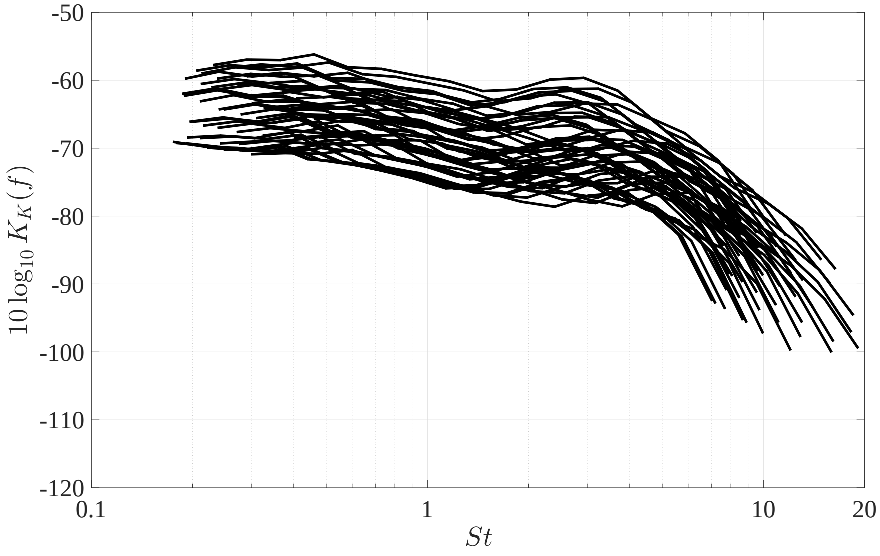

FIGURE 4.10: The general sound power spectra for restrictor noise from Kårekull's model.

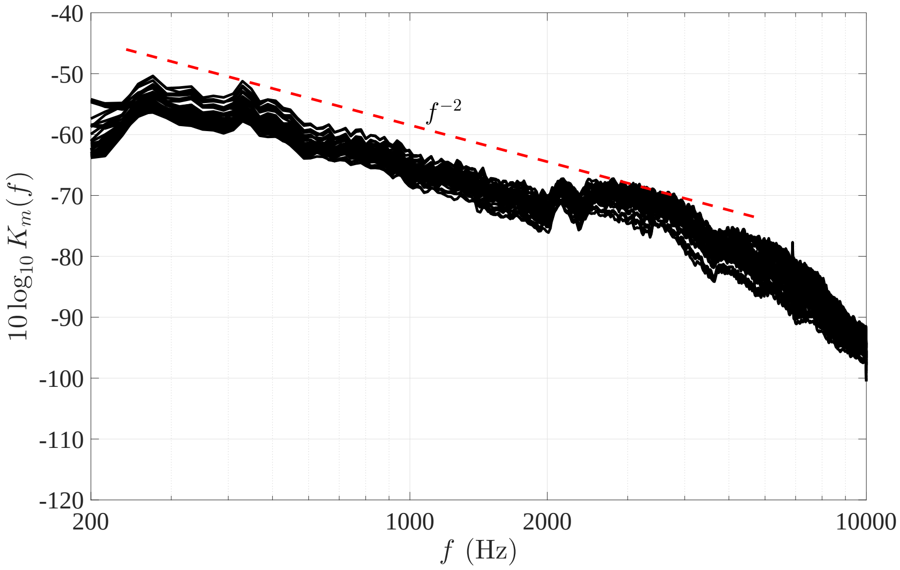

(a) The overall collapse of sound power using the new model.

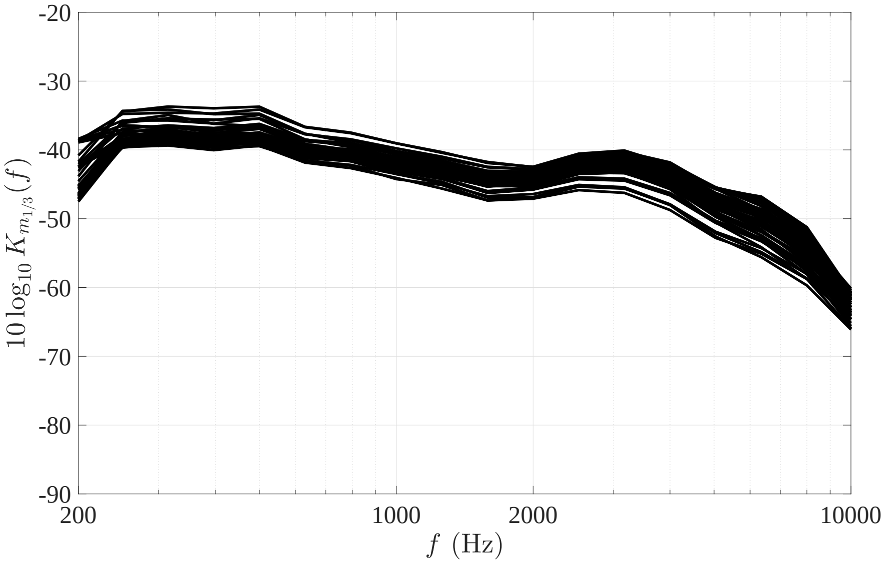

(b) The overall collapse of sound power level using the new model (1/3 octave band)

FIGURE 4.11: The overall collapse of restrictor sound power spectra using the new model.

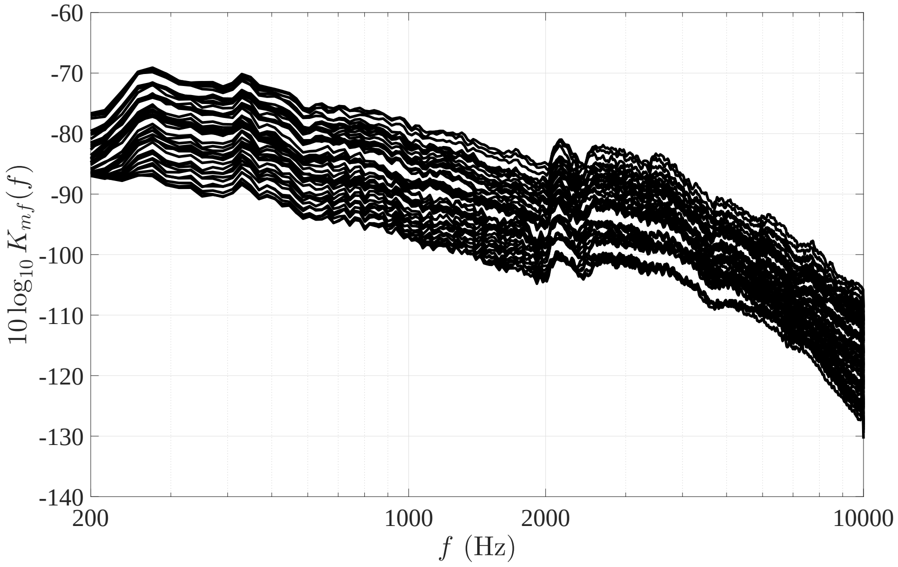

FIGURE 4.12: The overall collapse of sound power using momentum flux force model.

4.3.4 Discussion of the new model

4.3.4.1 The calculation of the steady force

In the new model developed in this thesis, the steady force is calculated from the product of the static pressure drop and the cross-sectional area of the duct. However, the static pressure drop is related to the measurement position. In Nelson and Morfey's experimental arrangement, the pressure taps were installed 'sufficiently far' to avoid the unsteady flow effect on the static pressure measurement. In Kårekull's paper, the pressure taps locations were selected according to the ISO 5167 international standard. These two measurements are both applied in this paper. It is found that although different static pressure drops were obtained, the collapse in results are similar. The benefit of using the ISO 5167 pressure arrangement is that the drag coefficients can be calculated using the Reader-Harris Gallaghter Equation. It is also found that the effect of the unsteady flow on the pressure drop measurement is negligible.

In Kårekull's work, it is assumed that the force can be scaled with the momentum flux. This yields another method for the calculation of the steady force, as shown in Equation 4.14. Substituing Equation 4.14 into Equation 4.3 yields

$$W = K_{mf}(f)\frac{\rho A^2 U^6}{c_0^3 h^2 \beta^8}. \tag{4.38}$$

Application of Equation 4.38 to collapse the measured data is presented in Figure 4.12. Agreement is generally poor. The reason may be that the momentum flux method shown in Kårekull's work is only valid for the restrictor with small restrictor internal diameters.

4.3.4.2 The simplified model in the plane wave frequency range

The sound power spectra plotted above, and in previous studies by Oldham and Ukpoho [48], show that they follow a clear f^{-2} scaling law for the plane wave frequency range, as shown in Figure 4.11(a). In this section we exploit this finding to develop a simple expression for K_m for arbitrary frequency and bandwidth. In view of the above, we can write

$$K_m(f_c, \Delta f) = \int_{f_c-\Delta f/2}^{f_c+\Delta f/2} K_m(f)df = f_\tau \int_{f_c-\Delta f/2}^{f_c+\Delta f/2} \frac{1}{f^2}df, \tag{4.39}$$

where f_τ is a constant with units of frequency. However, we emphasize that f_τ is simply a scaling factor and does not have any physical significance as a characteristic frequency. Equation 4.39 can be evaluated to

$$K_m(f_c, \Delta f) = \frac{f_\tau \Delta f}{(f_c^2 + (\Delta f)^2/4)}. \tag{4.40}$$

For the PSD of the sound power, Δf=1 Hz and in the plane wave frequency range 200 Hz< f_c <2010 Hz, $\Delta f << f_c$, the constant K_m for a unit frequency bandwidth can be written as

$$K_m(f) = \frac{f_\tau \Delta f}{f^2}, (\Delta f = 1Hz). \tag{4.41}$$

The value of f_τ obtained from a least squares best fit through all the available spectral data is 0.245 Hz. For 1/3-octave bands, $\Delta f \approx 0.23 f_c$, which in Equation 4.40 yields the model for 1/3-octave band as

$$K_m(f_c, \Delta f) = \frac{0.23 f_\tau}{f_c}. \tag{4.42}$$

4.3.4.3 The sound power prediction using the new model

An example of the sound power level estimated using the normalized spectrum for a restrictor with an internal diameter of 65 mm is shown in Figure 4.13. The largest difference between the measured data and estimated data occurs in the high frequency range and is about 4 dB, when the mean flow velocity in the duct is 10.6 m/s.

The new pressure-drop model can be seen to provide better predictions of the experimental data compared to that obtained by previous models.

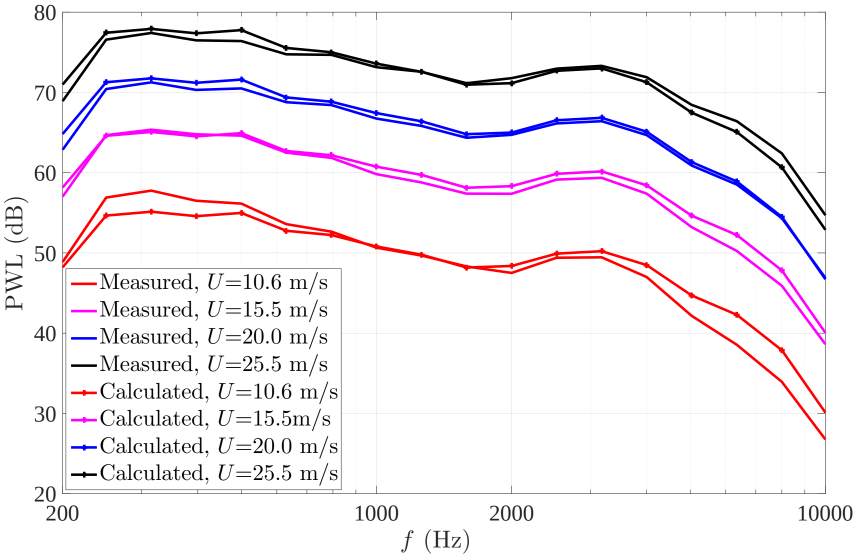

FIGURE 4.13: The sound power level calculated using Equation 4.23 for the restrictor with an internal diameter d=65 mm under different mean flow speeds.

4.4 Summary

In this chapter, the radiated sound power from the restrictors with different internal diameters under different mean flow speeds were measured. The range of the diameter ratio β of the restrictors investigated in this chapter is $0.5 < \beta < 0.8$, and the mean flow speed is from 10.0 m/s to 25.0 m/s. It has been shown that the PSD of the radiated sound power of different test cases are parallel, suggesting a frequency independent constant to collapse all the experimental results. Based on this observation, a semi-empirical model that contains easily measured parameters for the noise prediction by restrictors is developed with the assumption that the unsteady force on the surface of the restrictor is proportional to the steady force acting on the restrictor. This model can predict the restrictor noise with an error of 7 dB in the plane wave frequency range and an error of 10 dB in high frequency. This model also suggests that the sound power of restrictor obeys a U^6 velocity scaling law.

The size of the restrictor has a large effect on the restrictor noise. With the diameter ratio changing from 0.8 to 0.5, the radiated sound power increase about 16 dB.

In the plane wave frequency range, similar to the modal amplitude spectra, the radiated sound power follows a f^{-2} scaling law. Based on this observation, a very simple model that contains only one constant is developed to predict the restrictor sound power in the plane wave frequency range.

Chapter 5

Noise generation by a restrictor with upstream turbulence

5.1 Introduction

The previous chapters have presented a study on the characteristics and mechanisms of the noise generated by a single-hole restrictor within a duct. An ADS contains various components. Due to the length limitation of the ADS, two adjacent components must be installed close to each other. Quite often when an in-duct element is introduced upstream of the restrictor, such as a measuring device or a bend in the duct, the turbulent wake from the upstream element will interact with the restrictor to generate broadband interaction noise. The total noise now comprises the sum of the self-noise of the two elements plus the interaction noise. In some cases, interaction noise can dominate the two self-noise contributions. In this chapter, the mechanisms of interaction noise generation are investigated and a simple empirical model is developed to predict it.

In this chapter predictions are performed of the noise due to restrictors with varying internal diameters d interacting with upstream turbulence generated by rings with different dimensions installed upstream of the restrictor. Similar to the restrictor self-noise investigation presented in previous chapters, in-duct measurements, such as surface pressure measurements and modal analysis were performed to study the mechanisms of interaction noise generation. The radiated sound field at the end of the duct was also measured to deduce the sound power for comparison with the predictions of the interaction noise. The turbulence velocity spectra were measured close to the restrictor for various radial positions upstream of the restrictor to understand the noise generation mechanism. The downstream turbulence velocity spectra was also measured to assess the effects of the incoming turbulence on the downstream flow of the restrictor. Based on the measured sound power spectra a semi-empirical model is proposed in the final section of this chapter.

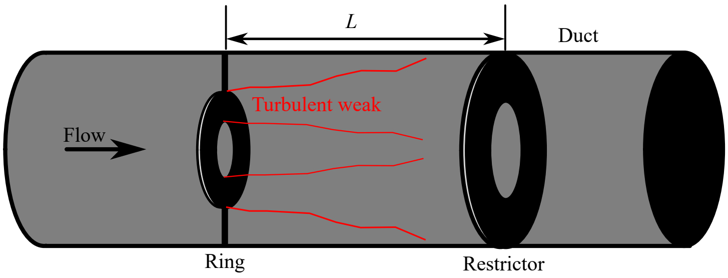

FIGURE 5.1: A schematic of turbulent weak shedding from the ring interacting with a restrictor, where L is the distance between the ring and the restrictor.

5.2 Generation and measurement of the interaction noise

For simplicity, statistical mean axi-symmetric turbulence was generated in the duct by the introduction of solid rings. Turbulence was produced in the wake of the rings. Different sized rings were introduced to generate different turbulence levels and length-scales. A schematic of the duct with restrictor and ring included is shown in Figure 5.1. The turbulent wake from the ring is shown to interact with the downstream restrictor. The distance between the ring and the restrictor is L and is varied in the experiment. The distance L and the external and internal ring diameters are the important geometric parameters in determining the turbulence level impinging on the surface of the restrictor. This chapter will show in Section 5.7 that the size of the restrictor also has a small effect on the turbulence level.

The interaction noise generated by the turbulence from a total of 8 different rings were investigated. The dimensions of the rings compared to the internal diameter of the duct is shown in Figure 5.2. The detailed dimensions of the rings is shown in Table 5.1. Figure 5.3 shows colour maps of the velocity spectra versus duct radius measured using the CTA at 8 axial positions downstream of ring 1 for a mean velocity of 15.0 m/s. The velocity spectra of the empty duct is also plotted for comparison. The location of the ring is marked in these figures as indicated in Figure 5.3. The highest velocity spectral level occurs in the wake region behind the ring. As the axial distance increases, the disturbance is shown to spread to the entire duct cross section. Narrow band peaks are observed at around 250 Hz in Figures 5.3(a), 5.3(b) and 5.3(c) which can be attributed to vortex shedding from the ring. The series of figures clearly show that the disturbance induced by the ring decays as the axial measurement distance increases from the ring. At the axial distance of 92 cm, which is the furthest measured axial position considered, the flow state has still not fully recovered to the undisturbed state, as shown by comparison with figure 5.25(h) for the empty duct. However, it will be later shown that interaction noise is negligible compare to the self-noise when the separation distance between the ring and the restrictor is around 90 cm for all restrictors investigated in the current work.

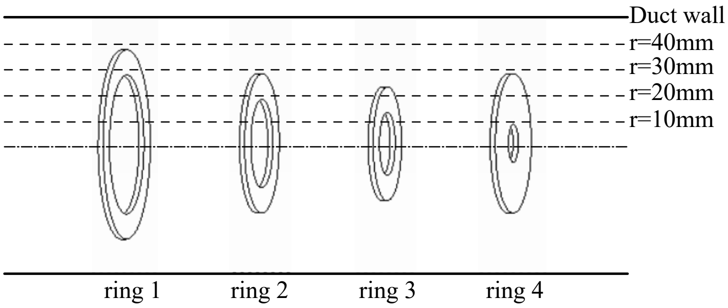

Figure 5.2: Schematic illustration of the rings with different diameters and widths.

Table 5.1: Size of the rings

Ring No.	Internal diameter (mm)	External diameter (mm)	width (mm)
ring1	55	75	10
ring2	35	55	10
ring3	25	45	10
ring4	15	55	20

The radiated sound power was measured from measurements of the acoustic pressure at ten far field microphones located at constant radius from the flare centre, as shown in Figure 2.1. As the interaction noise cannot be measured separately without contamination from self-noise, the measured total radiated sound power W_t is assumed to be the sum of self-noise of the restrictor W_s, the self-noise of the ring W_r and the interaction noise W_i. Therefore the interaction noise sound power spectra can be obtained from

$$W_i(f) = W_t(f) - W_s(f) - W_r(f). \tag{5.1}$$

In this chapter, the difference of sound power level ΔPWL between the total noise and the ring and restrictor self-noise is presented to show the increased sound power level, therefore

$$\Delta PWL = 10\log_{10}\frac{W_t(f)}{10^{-12}} - 10\log_{10}\frac{W_s(f)}{10^{-12}} - 10\log_{10}\frac{W_r(f)}{10^{-12}}. \tag{5.2}$$

In this section the radiated sound power of the self-noise of the different-sized rings is presented to allow measurements of interaction noise. The spectra of the self-noise of all rings sketched in Figure 5.2 is plotted in Figure 5.4. For comparison, the self-noise of the restrictor with an internal diameter of 65 mm is also plotted. Compared to the restrictor self-noise, two narrow band peaks are clearly observed in the sound power spectra of the ring noise. It can be attributed to vortex shedding from the ring. For some rings the level of the narrow bands peaks is higher than the restrictor self-noise. Apart from the narrow band peaks, the broadband self-noise generated by the ring is much lower than the self-noise of the restrictor. It should be noted that the results in the following sections may be affected at frequencies close to vortex shedding frequencies.

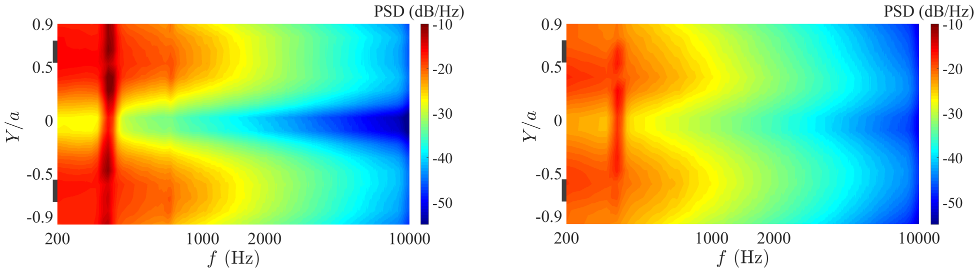

(a) L=7 cm. (b) L=12 cm.

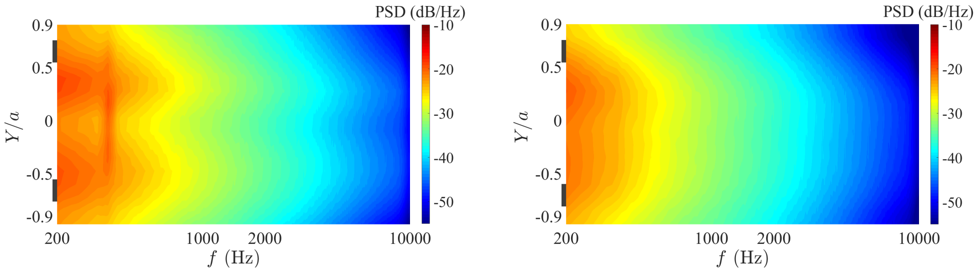

(c) L=17 cm. (d) L=27 cm.

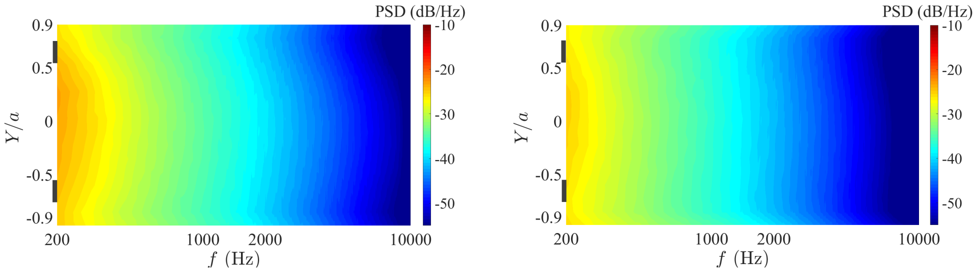

(e) L=52 cm. (f) L=72 cm.

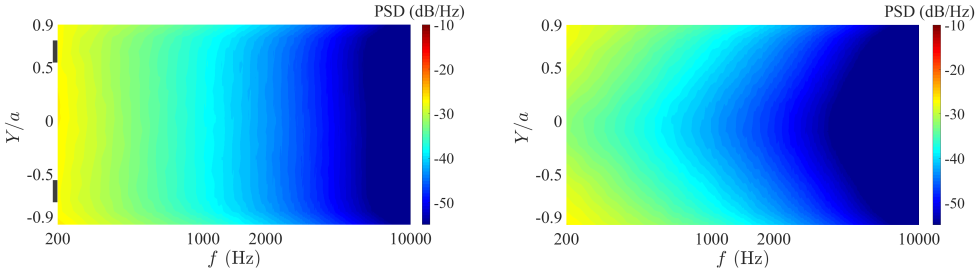

(g) L=92 cm. (h) Empty duct

FIGURE 5.3: Velocity spectra downstream of the ring 1 at different axial positions and the velocity spectrum of the empty duct under a mean flow speed of 15.0 m/s, where L is the axial distance between the ring and the measured point. The velocity spectra of the empty duct was measured when the flow is fully developed.

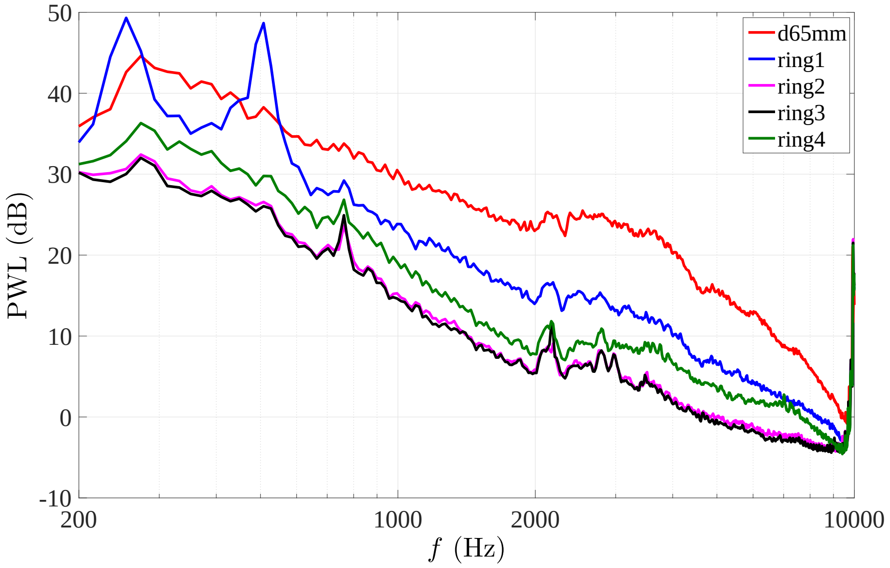

FIGURE 5.4: Comparison of the self-noise of different rings and restrictor with an internal diameter of 65 mm under the mean flow speed of 10.8 m/s.

5.3 Properties of the interaction noise

This section presents a parameter study in which the effects of mean flow speed, turbulence level, restrictor size on interaction noise generation are investigated. The total radiated sound power W_t, sound power of the restrictor self-noise W_s, and the sound power of the ring self-noise W_r were measured separately and the interaction noise is calculated from Equation 5.2.

5.3.1 Effects of mean flow speed on the interaction noise

Figure 5.5 compares the difference of PWL spectra between the total noise W_t and the sum of the ring and restrictor self-noise $W_s + W_r$, with varying mean flow speed. In this measurement, ring1 was installed 11 cm upstream of the restrictor with an internal diameter of 65 mm. The mean flow speed was varied between 10.0 m/s and 25.0 m/s. To assist comparison, the spectra of total noise is presented in Figure 5.5(a). The peaks in Figure 5.5(b) are due to the vortex shedding by the ring. The dips in the spectra arise from the subtraction of the ring self-noise from the total noise. For the total noise, only one obvious peak is observed. However, for the ring self-noise, two peaks are observed, as shown in Figure 5.4. The difference of the total noise and the self-noise also plotted against Strouhal number in Figure 5.5(c). Good collapse of the peaks illustrate the peaks are due to the vortex shedding of the ring. Figure 5.5(b) clearly shown that interaction noise generation is highly dependent on frequency. In the plane wave frequency range (below 2010 Hz), interaction noise generation is dominant, with the difference between the total noise and the self-noise being larger than 5 dB. As the frequency increases, the

Table 5.2: Velocity dependence of the interaction noise

Test case	Frequency range [Hz]			
	600-2000	2000-3000	2000-10000	600-10000
ring1-d55mm-11cm	5.4	6.3	6.6	5.6
ring4-d55mm-11cm	5.8	6.0	6.5	5.9
ring1-d65mm-11cm	5.9	6.7	7.1	6.0
ring4-d65mm-11cm	5.9	5.8	6.3	6.0
ring1-d75mm-11cm	6.3	7.8	7.8	6.4
ring4-d75mm-11cm	6.0	6.2	6.3	6.1

difference in level decreases. For the test cases shown in Figure 5.5(b), the difference is around 2 dB above 5000 Hz. It is also observed that the difference between the total noise PWL and the self-noise PWL is similar across the range of flow speeds investigated. This suggests that interaction noise obeys a similar velocity scaling law as the restrictor self-noise.

The PWL spectra of interaction noise calculated by subtracting self-noise from the total noise for ring1 installed 11 cm upstream of the restrictor with an internal diameter of 65 mm under different mean flow speeds is shown in Figure 5.6. Similar to the restrictor self-noise, the interaction noise spectra are parallel. The velocity dependence of the interaction noise integrated over different frequency bands for different combinations of the ring and restrictor is shown in Table 5.2. In general, interaction noise obeys a U^6 velocity scaling law and exhibits a small variation in power law with restrictor size and flow speed compared to the restrictor self-noise. The effects of the size of the restrictor on interaction noise generation will be discussed in more detail in section 5.3.3.

5.3.2 Effects of the turbulence level on the interaction noise generation

In the current work, for a specific restrictor, the level and characteristics of the upstream turbulence is determined by the dimensions of the ring as well as the separation distance between the ring and the restrictor. In this section, the effects on interaction noise due to variations in ring internal and external radius, and separation distance, are presented.

Figure 5.7 compares the PWL spectra of the total noise and self-noise for ring 1 installed at five different separation distances L upstream of the restrictor ranging between 3 cm and 80 cm. The internal diameter of the restrictor is 65 mm and the mean flow speed is 10.8 m/s. In these cases, the highest interaction noise appears to occur at the separation distance of 5 cm, where the total noise is about 10 dB above the self-noise in the plane wave frequency range and about 5 dB at frequencies above the first cut-on frequency. Interaction noise generation at $L = 3$ cm is seen to be slightly smaller than at $L = 5$ cm. However, vortex shedding peaks due to ring for $L = 3$ cm test case is higher than that for $L = 5$ cm test case. Furthermore, vortex shedding peaks at $L = 3$ cm occurs at higher frequency than $L = 5$ cm test case. This suggests a higher local flow speed at

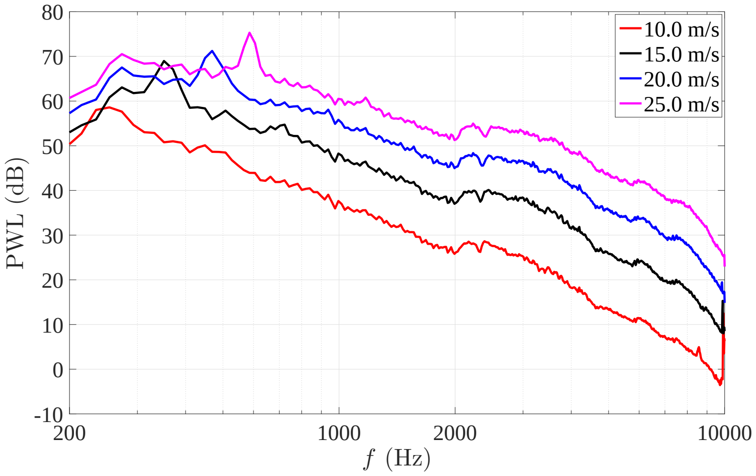

(a) PWL spectra of total noise of ring 1 installed 11 cm upstream d=65 mm restrictor under different mean flow speeds.

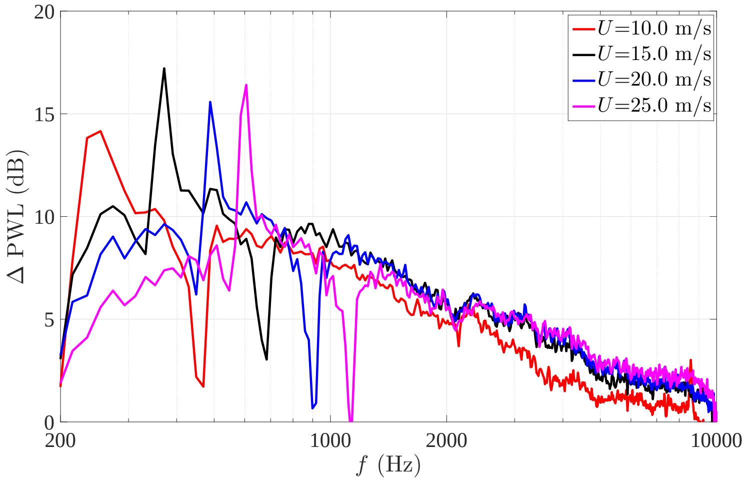

(b) Difference between the total noise PWL and self-noise PWL under different mean flow speeds plotted against frequency.

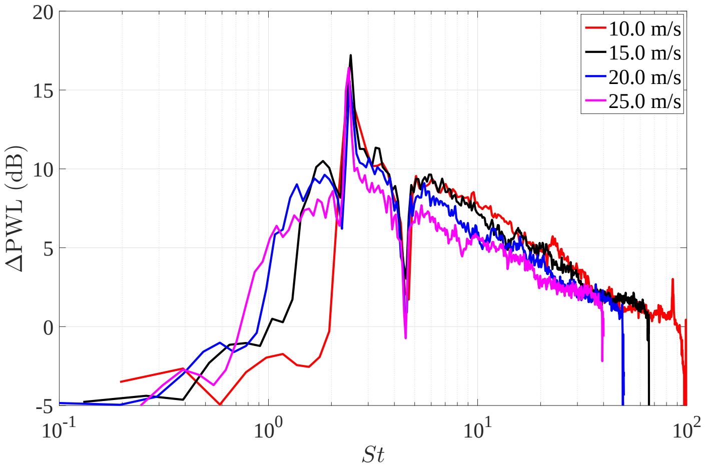

(c) Difference between the total noise PWL and self-noise PWL under different mean flow speeds plotted against Strouhal number.

FIGURE 5.5: Difference between the total noise PWL and self-noise PWL under different mean flow speeds. For all test cases, ring 1 was installed 11 cm upstream of the restrictor with an internal diameter of 65 mm.

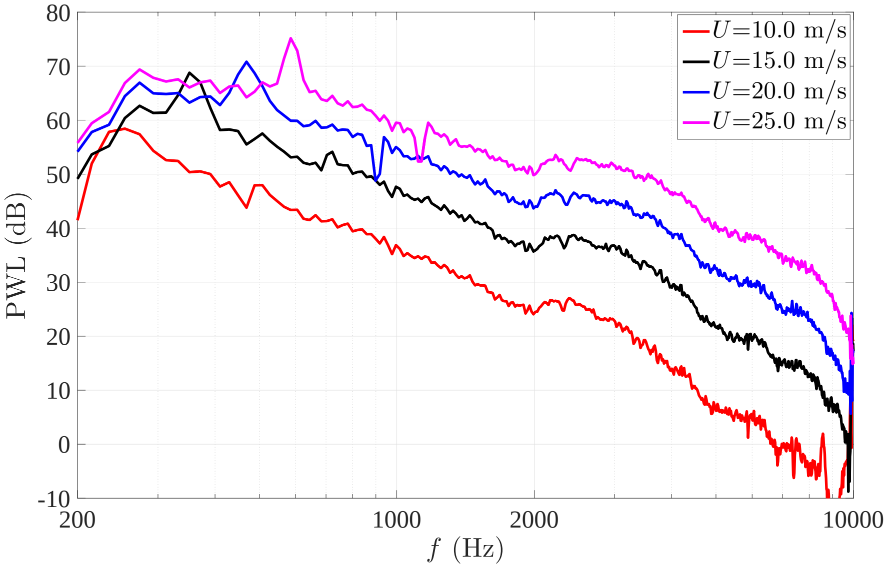

Figure 5.6: PWL spectra of interaction noise under different mean flow speeds. For all test cases, ring 1 was installed 11 cm upstream of the restrictor with an internal diameter of 65 mm.

the ring for $L = 3$ cm, which can be attributed to the higher local flow speed due to the blockage of the restrictor. As the flow approaches the restrictor, the speed of the flow around centre line is accelerated. The reason for lower interaction noise generation at $L = 3$ cm test case might be that the turbulent wake passes through the centre of the restrictor without fully impinging on the restrictor surface. As the separation distance increases above 5 cm the total noise decreases. This can be attributed to the decay of the turbulent flow produced by the ring. At the separation distance of 29 cm, the interaction noise is substantially below the self-noise in the plane wave frequency range. When the separation distance is 80 cm, interaction noise is negligible.

Different rings induce turbulence of different levels and length-scales, leading to the different interaction noise spectra. Figure 5.8 presents the difference between PWL spectra of the total noise and self-noise with different rings installed upstream of the restrictor at the same distance. The internal diameter of the restrictor for all cases was 65 mm. The mean flow speed in the duct was 10.8 m/s, and the separation distance between the ring and the restrictor was 11 cm. Among the four ring cases presented in Figure 5.8, in the plane wave frequency range, the highest interaction noise was generated by ring 1. Above the first cut-on frequency, the highest interaction noise was generated by ring 4. The non-parallel spectra imply that the interaction noise spectra is determined by the upstream turbulence velocity spectra.

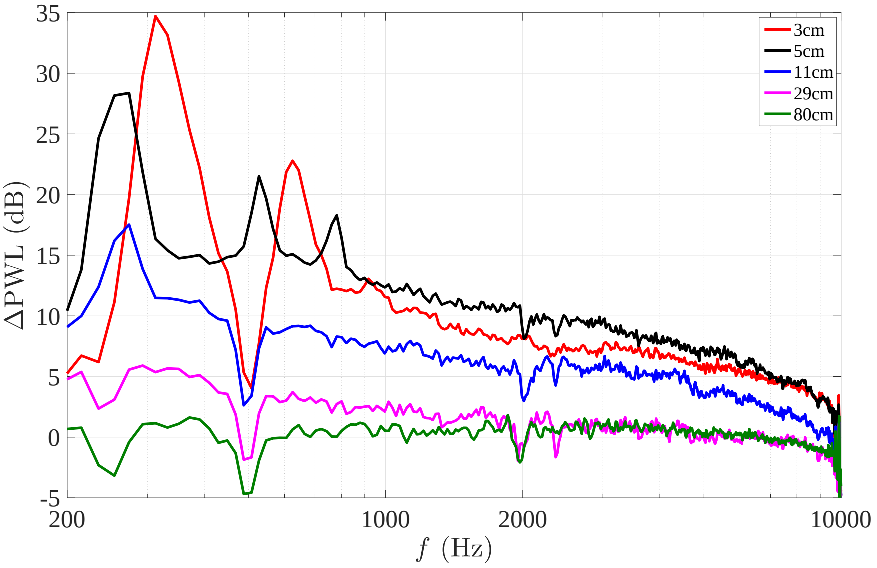

FIGURE 5.7: The effects of the separation distance between the ring and the restrictor on the difference between the total noise PWL and self-noise PWL. In the test case, ring1 was installed upstream of the restrictor of d=65 mm under a mean flow speed of 10.8 m/s.

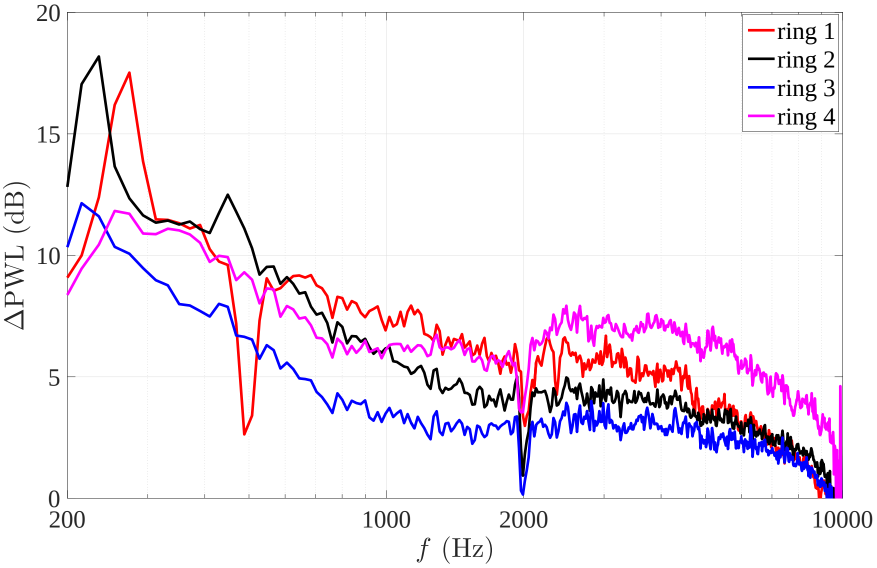

FIGURE 5.8: Variation of difference between the total noise PWL and self-noise PWL with different rings installed 11 cm upstream of the restrictor with an internal diameter of 65 mm under a mean flow speed of 10.8 m/s.

5.3.3 Effect of the size of the restrictor on the interaction noise generation

The interaction noise spectrum is determined by the combination of the upstream turbulence characteristics and the restrictor itself. In this section, interaction noise generation by different restrictors with the same ring installed upstream is investigated. Figure 5.9(a) presents the difference in the PWL spectra between the cases with and without ring 1 installed upstream of the restrictors with internal diameters of 55 mm, 65 mm and 75 mm. The separation distances between the ring and the restrictor were 11 cm for all three test cases. The difference between the total noise and the self-noise spectrum is largest for d=65 mm restrictor. By contrast, the restrictor d=55 mm produces the smallest difference. There are two reasons for the different interaction noise spectra by different restrictors. First, the self-noise of restrictor d=55 mm is highest. The difference between the total noise and self-noise is therefore smallest. Second, the restrictor d=75 mm produces least interaction noise, leading to the difference between the total noise and interaction noise being smaller than for the restrictor d=65 mm.

The interaction noise spectra obtained by spectral subtraction is shown in Figure 5.9(b). Similar to the self-noise spectra, the interaction noise spectra for different restrictors due to turbulence generated by the same ring are observed to be closely parallel. This observation suggests that the interaction noise spectra can be collapsed by the use of a frequency-independent parameter. In this investigation it has been observed that the interaction noise generated by an upstream turbulence generator is proportional to the square of the restrictor drag coefficient C_d^2. Reasonable collapse of the interaction noise spectra can therefore be obtained by normalizing the spectra using C_d^2, as shown in Figure 5.10. Below 700 Hz, the collapse of the spectra is within about 6 dB and improves as frequencies increases. The unsatisfactory collapse in the low frequency range may be because of noise contributions due to vortex shedding from the ring. Between 700 Hz and 2000 Hz, however, agreement is within 3 dB, and above the first cuton frequency agreement is better than 2dB. At very high frequencies, above about 8000 Hz, interaction noise generation is weak, leading to relatively poor collapse of the spectra.

The interaction noise spectra are seen to collapse reasonably well with C_d^2, which is the same power law observed for the self-noise sound power spectra discussed in Chapter 4. This suggests that the fundamental noise generation mechanism for self-noise generation and interaction noise may be identical. The precise reason for this scaling of the interaction currently remains unclear and further work is needed to explain its origin.

It has been shown in previous sections that for ring 1 installed upstream of d=65 mm restrictor, interaction noise only exceeds the self-noise in the plane wave frequency range at separation distances greater than 29 cm. Greater than 80 cm, negligible interaction noise is generated at all frequencies. Thus, for each combination of ring and restrictor there exist critical distances, above which, interaction noise can be neglected in a specific frequency range. The two critical distances for the different restrictors are shown in Table

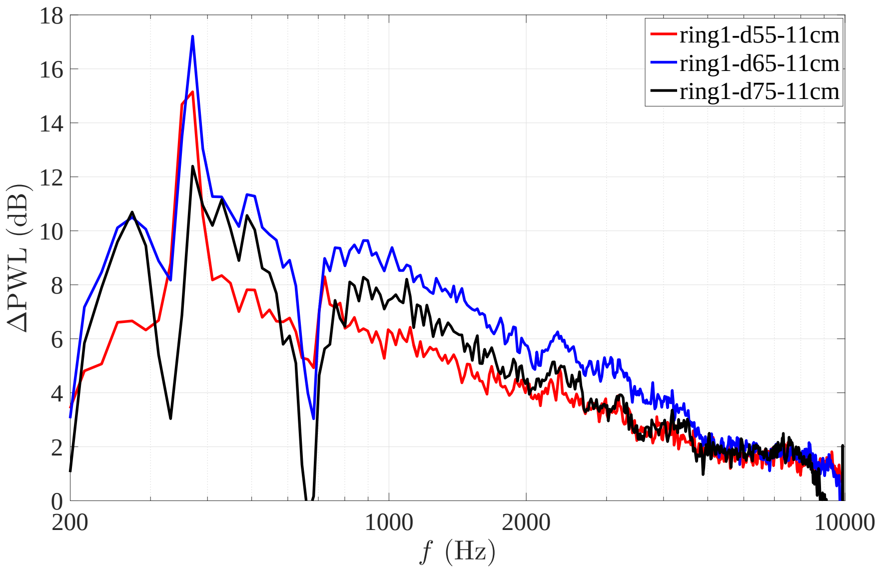

(a) Difference of the total noise PWL and self-noise PWL for different restrictors. For all test cases, ring1 was installed 11 cm upstream of the restrictors.

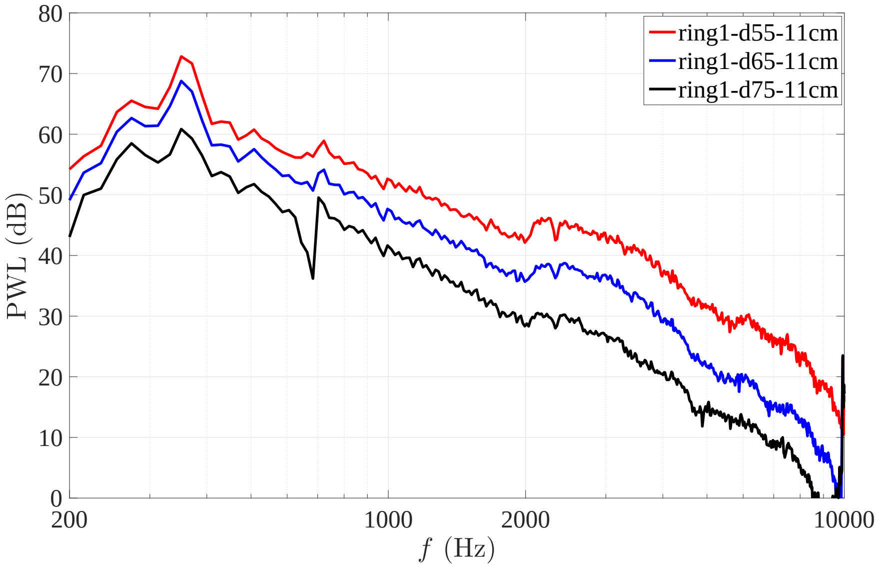

(b) Comparison of the interaction noise.

FIGURE 5.9: Variation of interaction noise with different restrictors under a mean flow speed of 15.0 m/s.

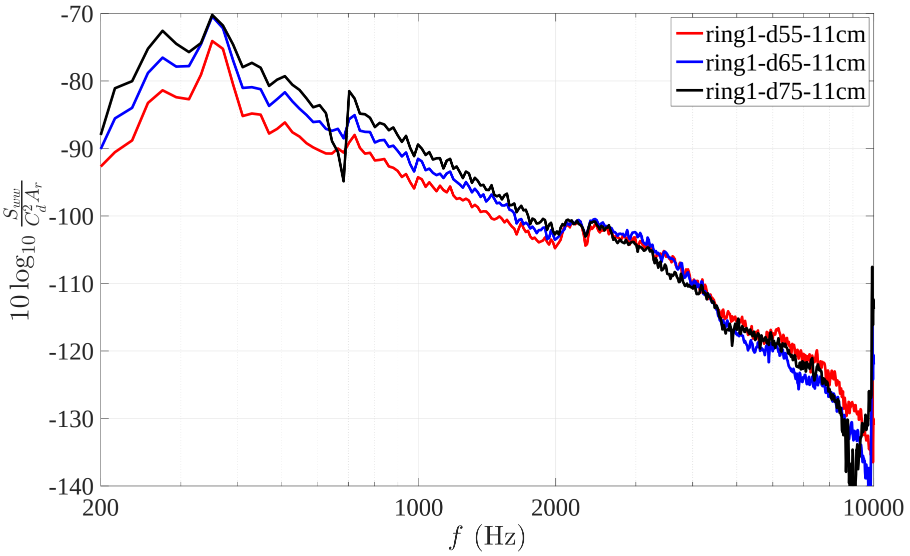

FIGURE 5.10: Collapse of the interaction noise power spectra S_{ww} using the drag coefficient, where C_d is the drag coefficient and A_r is the surface area of the restrictor. The mean flow speed is 15.0 m/s.

TABLE 5.3: Critical distances for the interaction noise generation

Test cases	Only in plane wave	Negligible interaction noise
ring1-d55mm	36 cm	92 cm
ring1-d65mm	29 cm	80 cm
ring1-d75mm	17 cm	29 cm

5.3. One critical distance is that the interaction noise is generated in all frequencies below this distance. Above this distance, the interaction noise is only generated in the plane wave frequency range. Another critical distance is that the interaction noise generation is negligible above this distance. For restrictors with larger internal diameters, interaction noise is generated within a smaller separate distance. This also suggests that the restrictors with larger internal diameter are less effective than smaller diameters in generating interaction noise. Further analysis of the behaviour of the interaction noise spectrum is presented in Section 5.6.

5.4 Modal amplitude of the total noise

Modal analysis was performed for the total noise (interaction noise plus self-noise) in this section to investigate the effects of upstream turbulence on each modal shape and amplitude. The modal analysis results of the total noise is presented in Figure 5.11, in which the modal amplitudes for the plane wave mode and the $m = 1$ mode are plotted and compared to that for the self-noise. Whilst the level of interaction noise can be seen to be higher than for the self-noise, the shapes of the modal amplitude spectra are similar to the self-noise spectra and have very similar behaviour to the total noise. The plane wave mode spectra of the total noise is significantly higher compared to that due to self-noise. For the higher order modes with cut-off frequencies above 4000 Hz, the mode amplitudes are only slightly higher than the that due to self-noise.

5.5 Surface pressure measurements

In this section measurements of the pressure over the restrictor surface with a ring installed upstream of the restrictor are presented to investigate the mechanisms of the interaction noise generation.

A representative surface pressure measurement is shown in Figure 5.12 in which colour maps are presented of the pressure PSD versus frequency and radial positions. In this case, the internal diameter of the restrictor is 65 cm, with ring 1 installed 11 cm upstream of the restrictor. The mean flow speed in the duct is 10.0 m/s. The surface pressure frequency and radius distributions are similar to that of the restrictor self-noise, as shown in Figure 3.19. One difference is the presence of a narrow band peak at around 250 Hz due to the vortex shedding by the ring. The radial distribution of pressure in this figure shows that the turbulent wake from the ring impinges fairly uniformly over restrictor since there is no localisation of the surface pressure due to the wake. This finding is investigated in more detail in section 5.6 below where the turbulence velocity distribution over the restrictor is investigated.

In addition to the distribution of the surface pressure PSD, the degree of coherence between any two points on the restrictor is also important in determining the efficiency of noise radiation along the duct. Figure 5.13(b) shows that the coherence of the surface pressure between a point on the inner radius of the restrictor and four points separated radially by 3mm, 6mm, 8mm and 12mm. Figure 5.13(c) shows the coherence between a point at 42.75 mm radius and six others separated circumferential by a distance of 4.3, 8.6, 12.9, 17.2, 21.5 and 25.8 mm.

In both figures the level of coherence is highest in the plane wave frequency range. The peak at about 250 Hz is due to vortex shedding by the ring. Above the first cut-on frequency of 2010 Hz, the coherence drops to very small levels (< 0.01), suggesting that the efficiency of radiation in this frequency range is very small. Along the radial direction shown in 5.13(b) the coherence is observed to drop quite sharply between the separation distances of 3 mm and 6 mm. However, at the two largest separation distances of 9mm and 12mm the coherence is unchanged. The reason for this finding may be due to the contribution to the surface by the vortex shedding due to the ring, which peaks at 250 Hz and its harmonic of 500 Hz, as shown more clearly in figure 5.15. The coherence is also observed to decay very slowly along the circumferential direction in 5.13(c), where the separation distance is varied over a larger range than along the radial direction.

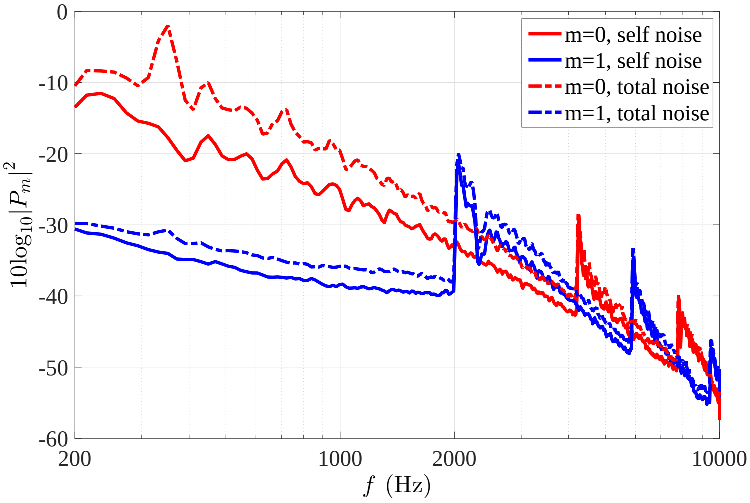

(a) d=55mm.

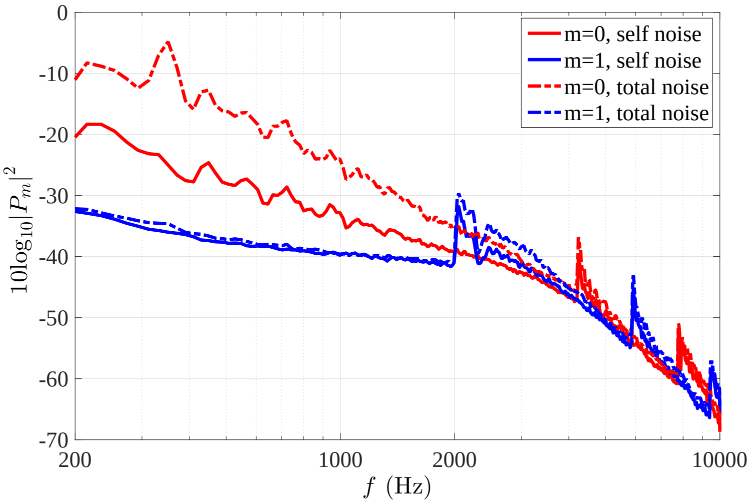

(b) d=65mm.

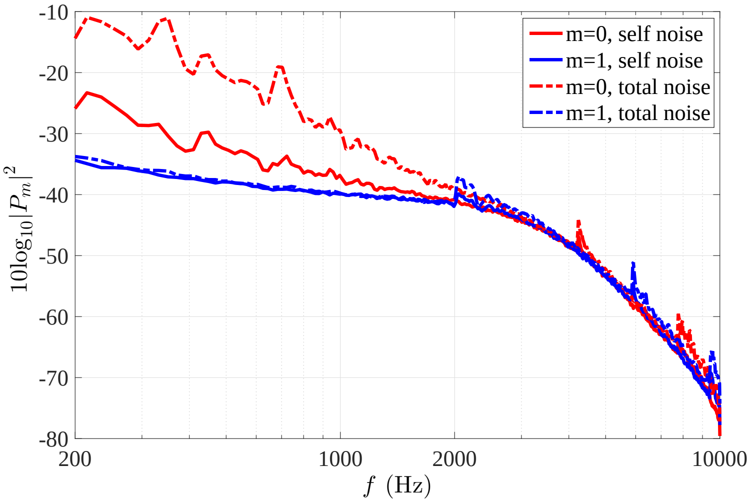

(c) d=75mm.

FIGURE 5.11: Comparison of the modal pressure spectra for restrictors with ring1 in front of them under a mean flow velocity of 15.0 m/s.

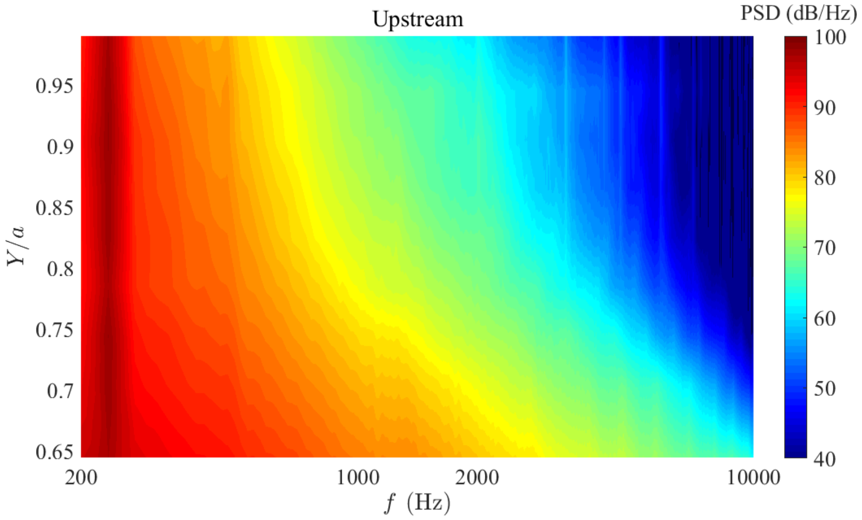

(a) Upstream side.

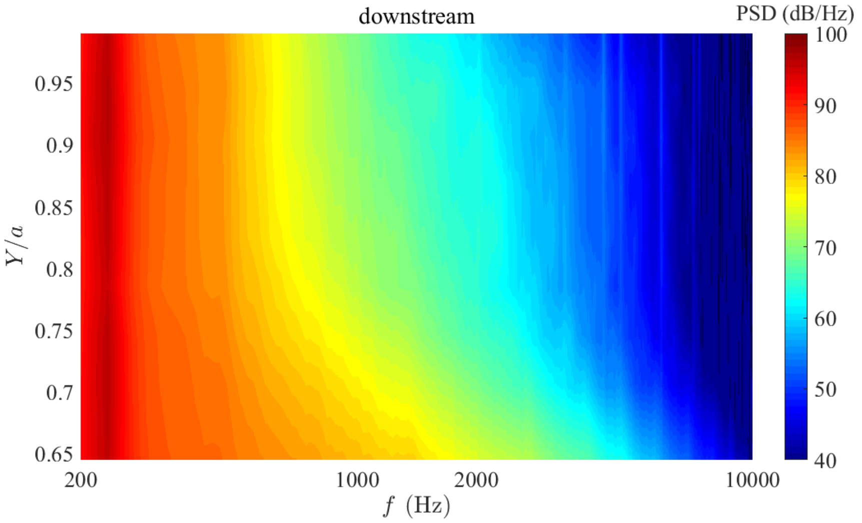

(b) Downstream side.

FIGURE 5.12: PSD of the surface pressure of the restrictor d=65 mm with ring1 installed 11 cm upstream under a mean flow speed of 10.0 m/s.

The surface pressure coherence due to the total noise is observed to be slightly higher than for the self-noise alone. It is currently unclear whether this is due to turbulence interaction or by coherent vortex shedding by the ring.

In this section the PSD of the total noise is calculated based on the surface pressure using the same procedure described in section 3.6.1 for the self-noise. Using Equation 3.48 the effective correlation area was calculated versus frequency and plotted in figure 5.14 at six different flow speeds between 9.9 m/s and 22.5 m/s. The peaks below about 600 Hz are due to the vortex shedding from the ring. Above 600 Hz, the correlation area due to the sum of interaction and self-noise generation noise mechanisms is seen to be roughly twice that due to self-noise alone at the same flow speed, which is consistent with higher levels of coherence for the total noise.

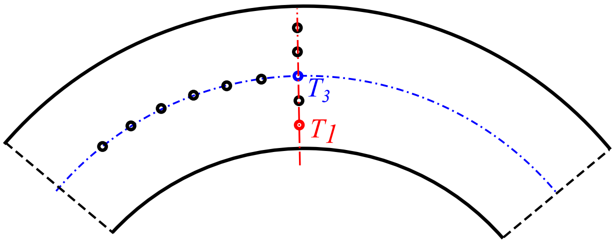

(a) The arrangement of pressure taps for coherence measurements.

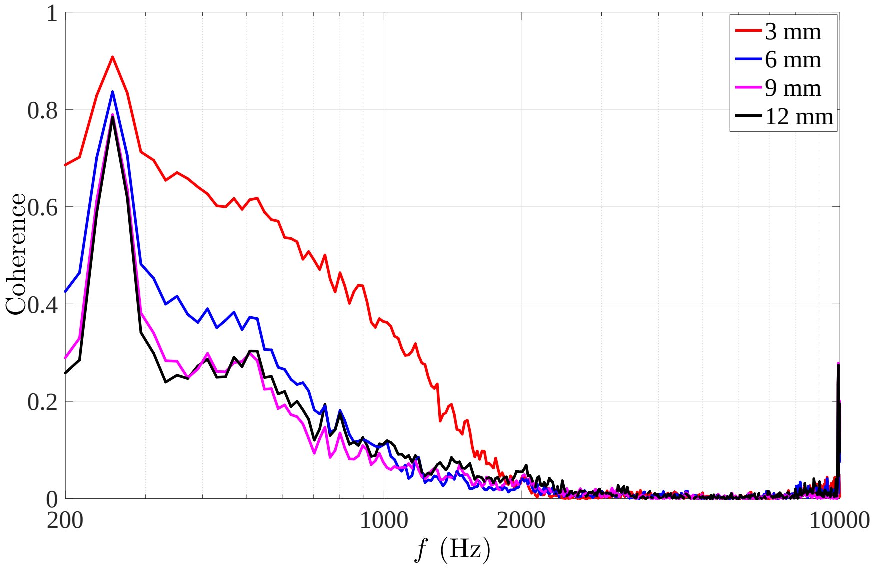

(b) The coherence along the radial direction.

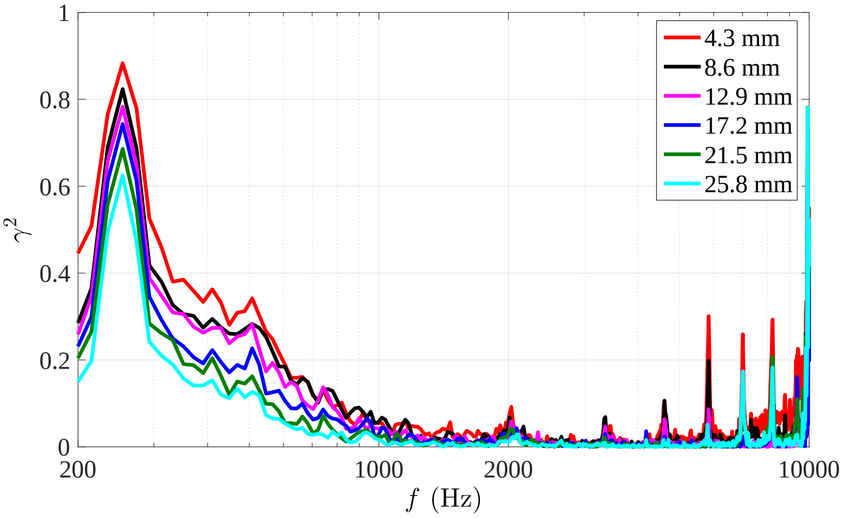

(c) The coherence along the circumferential direction.

FIGURE 5.13: Coherence of the surface pressure upstream of the restrictor d=65 mm with ring1 installed 11 cm upstream under a mean flow speed of 10.8 m/s. For radial direction, the coherence was between pressure tap T_1 and other pressure taps in radial direction. For circumferential direction, the coherence was between pressure tap T_3 and other pressure taps along circumferential direction.

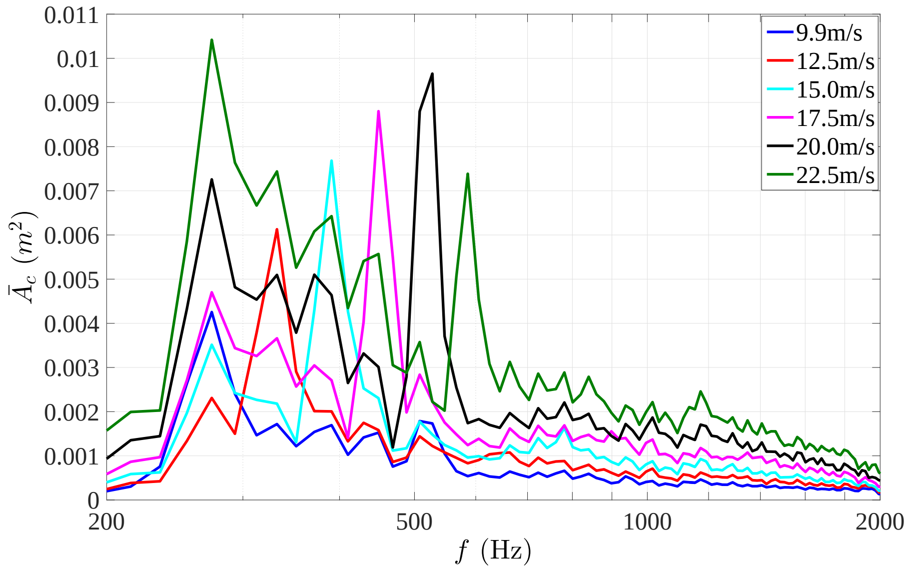

FIGURE 5.14: Correlation area of the surface pressure of the restrictor d=65 with ring1 installed 11 cm upstream under a mean flow speed of 10.8 m/s.

The comparison between the sound power based on the surface pressure measurement and the directly measured sound power in the plane wave frequency range is shown in Figure 5.15 at five different flow speeds between 9.9 m/s and 22.5 m/s at the two ring - restrictor separation distances of 11cm and 29cm. Agreement between the two power estimates at both separation distances is generally better than 2 dB across the frequency range, except at frequencies close to the two vortex shedding peaks of 250Hz and 500Hz. The presence of a turbulence generator in the duct therefore appears to gives rise to an increase in surface pressure and higher levels of coherence on the surface of the restrictor. This surface pressure PSD variation and coherence, as shown previously for self-noise generation, is entirely consistent with the increase in transmitted sound power.

To further investigate the relationship between the surface pressure and the interaction noise generation, the comparison of the surface pressure spectra with and without the ring installed upstream of the restrictor is investigated in this section. Figure 5.16 presents the difference between the surface pressure spectra in dB without and with ring 1 installed upstream of the restrictor d=65 mm with different separation distances L. The mean flow speed in the duct are 15.0 m/s for all the three cases. The selected three distances are $L = 11cm$, $29cm$, and $80cm$, corresponding to the interaction noise generation in all frequencies, plane wave frequencies, and negligible interaction noise. When $L = 11cm$, compared to the surface pressure without the ring, the surface pressure increases about 10 dB in the plane wave frequency range on both sides of the restrictor. In the frequency range above the first cut-on frequency range, the surface pressure increases about 5 dB on the upstream side and about 2 dB on the downstream side. When the separation distance between the ring and the restrictor is $29cm$, the surface pressure increases about 5 dB only in the plane wave frequency range, an the above the

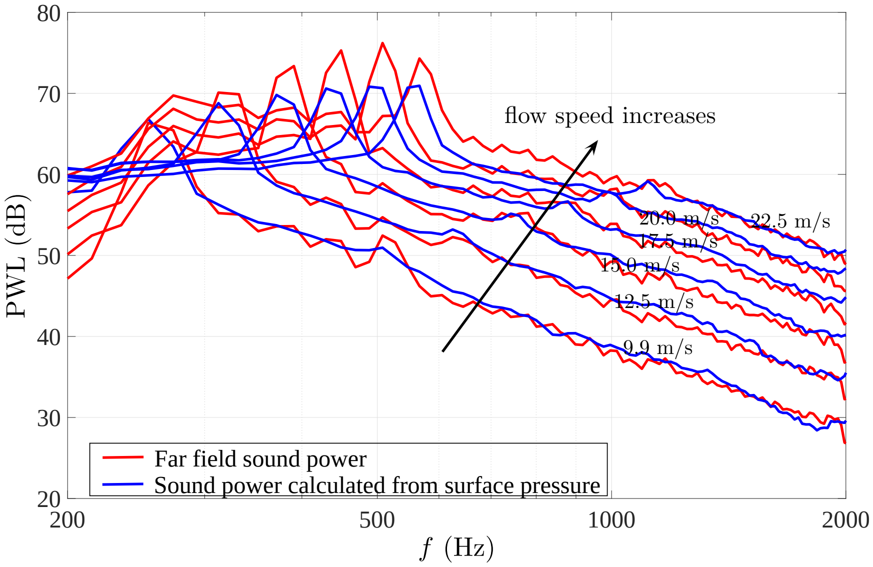

(a) The d=65mm restrictor with ring1 installed 11cm upstream.

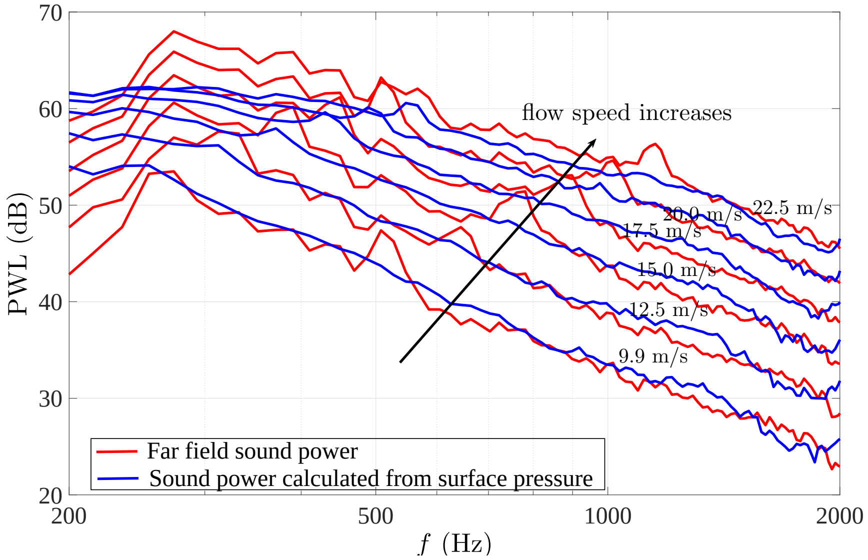

(b) The d=65mm restrictor with ring1 installed 29cm upstream.

FIGURE 5.15: Comparison of the sound power from far field sound measurements and surface pressure measurement.

first cut-on frequency, the increase in the surface pressure is negligible. When $L = 80cm$, the surface pressure is only slightly (about 1 dB) higher than that without the ring in all frequency range. Thus, the changing in the surface pressure due to the turbulence wake of the ring is consistent with the changing of the radiated sound power as shown in Figure 5.7.

Figure 5.17 presents the difference between the surface pressure spectra in dB with and without ring1 installed upstream of the restrictors with different internal diameters. The mean flow speeds in the duct are both 15.0 m/s for the two cases. Together with the surface pressure difference shown in Figure 5.16(a), the increased surface pressure on the upstream side for the three restrictors is roughly similar, which is around 8 dB increase at all frequencies. This suggests that the upstream turbulence induced by the ring has a similar effect on the surface pressure of the upstream side. For the downstream side, the surface pressure of the restrictor with smaller internal diameter is seen to have a smaller increase. For the restrictor d=75 mm, the surface pressure increases about 10 dB in the plane wave frequency range and about 5 dB above the first cut-on frequency. The corresponding increases are 7 dB and 3 dB for the restrictor d=65 mm and 5 dB and 2 dB for the restrictor d=55 mm. The reasons may be that the upstream turbulence is easy to pass through the restrictor with a larger internal diameter and affect the surface pressure on the downstream side.

5.6 The relationship between flow fluctuation and interaction noise

5.6.1 Turbulence flow measurement upstream of the restrictor

In this section the flow velocity spectra distribution along the radial direction at 3 cm upstream and 3 cm downstream of the restrictor were measured with the ring installed upstream. The velocity spectra for different separation distances between the ring and the restrictor were measured using a CTA to investigate the effect of velocity fluctuations on interaction noise generation. The separation distances in this section were chosen to correspond to the ‘critical distances’ defined above for different-sized restrictors described in Table 5.3. A schematic of the experimental arrangement for the velocity spectra measurements upstream of the restrictor is shown in Figure 5.18. For the downstream measurement, the experimental arrangement is similar to the upstream measurement apart from the axial position of the hot-wire probe. Due to the size of the hot-wire probe holder and the flange for the installation of the restrictor, the velocity spectra measurements cannot be conducted immediately upstream and downstream of the restrictor. The distances between the hot-wire probe and the upstream and downstream surface of the restrictor are both 3 cm. A single-wire hot-wire probe was used to perform the measurements. The probe was traversed automatically along the radial direction of the duct in 16 equal steps. The traversing distance of each step was 6.25 mm. The distance covered was from 4.25 mm to the bottom duct wall and covered a 96 mm distance stopping a distance 2 mm from the duct wall of the other side. The velocity spectra are compared with the velocity spectra without the ring installed upstream of the restrictor to deduce the contribution to overall turbulence by the ring.

Colour maps of the difference in the velocity spectra in dB versus frequency and radial positions, with and without ring1 installed upstream of the restrictors for three different restrictors of internal diameters 55 mm, 65 mm and 75 mm, are shown in Figures 5.19, 5.20 and 5.21. The positions of the restrictor surfaces are marked in these figures to

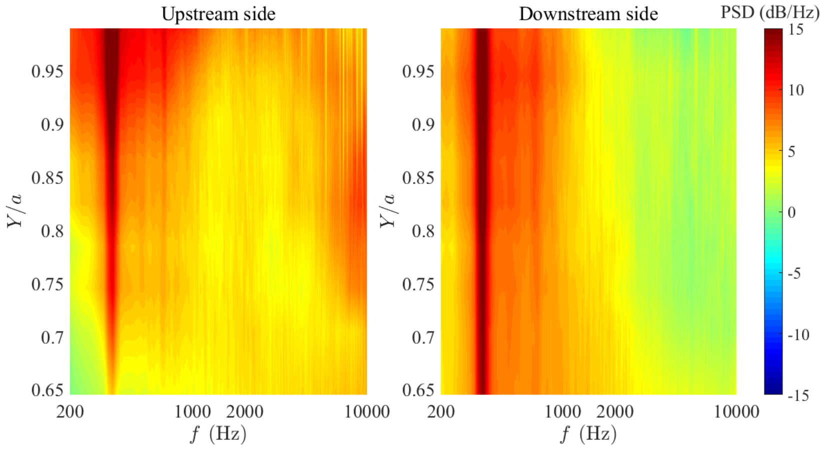

(a) L=11cm.

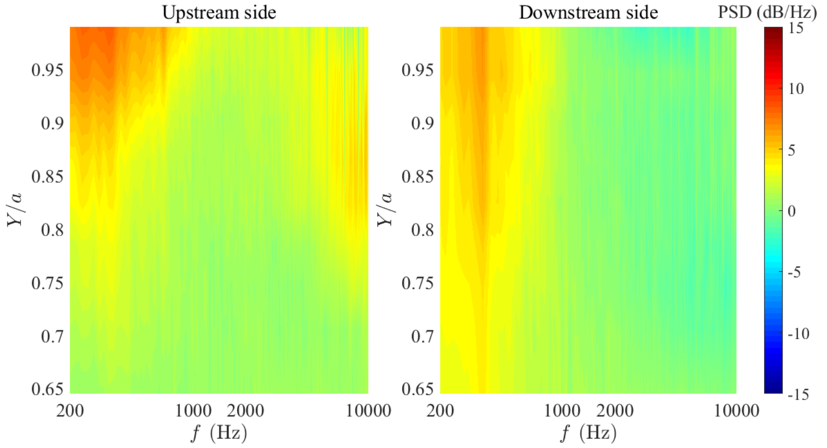

(b) L=29mm.

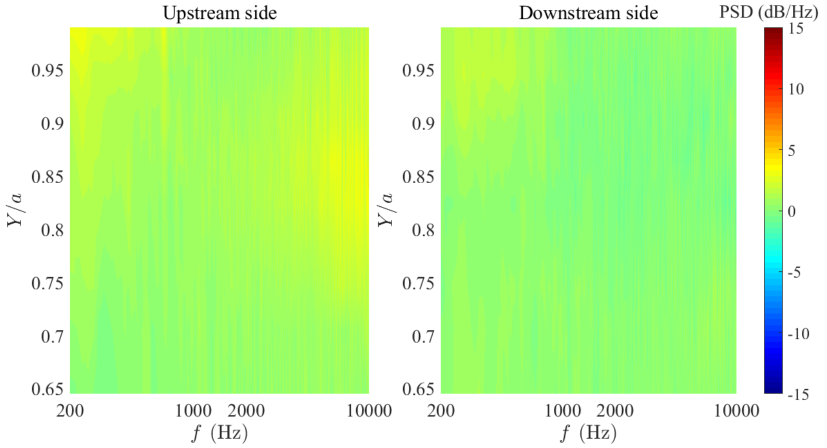

(c) L=80mm.

Figure 5.16: Comparison of the difference in surface pressure on the upstream and downstream side of the restrictor d=65 mm with and without ring1 installed 11 cm upstream of it with different distances under a mean flow velocity of 15.0 m/s.

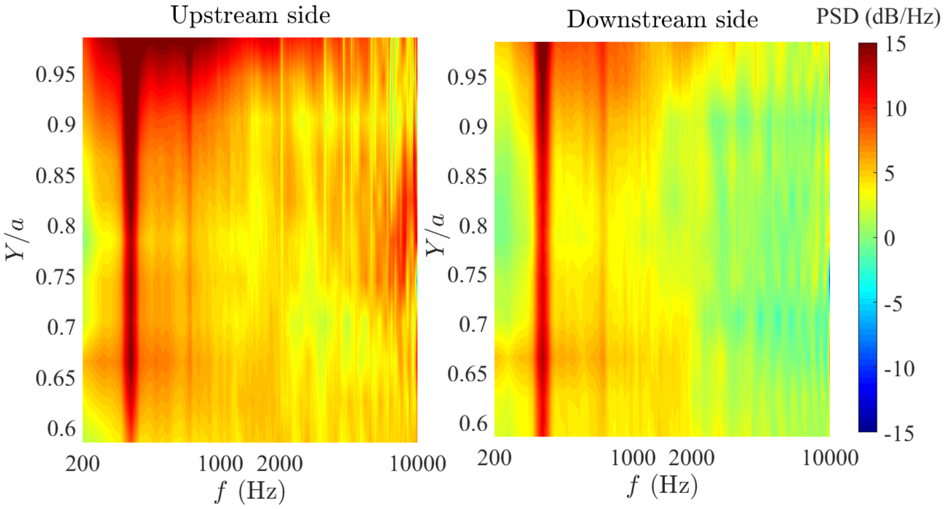

(a) d=55mm.

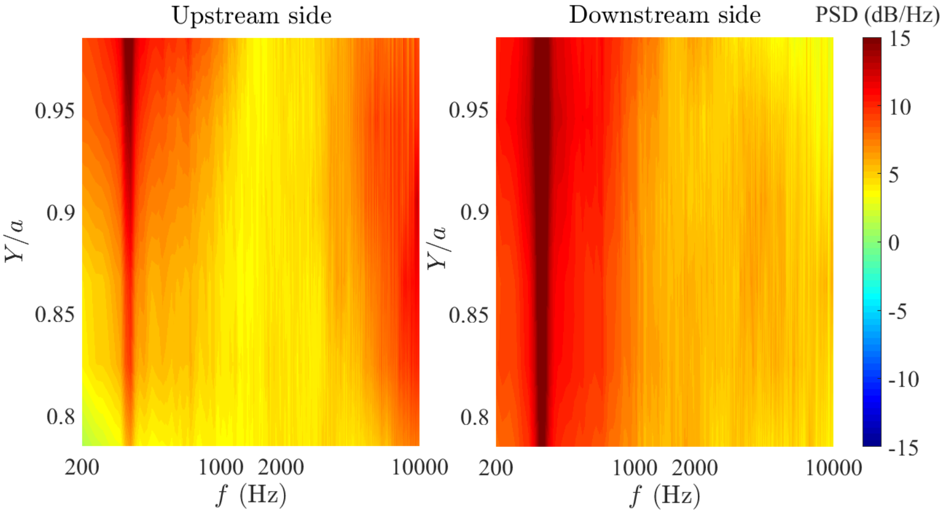

(b) d=75mm.

FIGURE 5.17: Comparison of the difference in surface pressure on the upstream and downstream side of the restrictors with and without ring1 installed 11 cm upstream of them under a mean flow velocity of 15.0 m/s.

identify the behaviour of the turbulent flow on the restrictor surface. For all test cases, the mean flow speed in the duct was 15.0 m/s. On the upstream side of restrictor d=55 mm, at the separation distance of 11 cm, the velocity spectra show a large increase in level compared to the velocity spectra without the ring. In the wake of the ring, the velocity spectra increase by more than 15 dB at all frequencies. Due to the vortex shedding from the ring, a narrow band peak appears at the frequency of about 250 Hz. Outside of the wake region, the velocity spectra increase by about 10 dB. The velocity spectra in front of the restrictor surface, which directly impinges on the restrictor increases by more than 10 dB. When the separation distance is increased to 36 cm, the increase in the velocity spectra in the wake is about 10 dB in the frequency range up to about 6000 Hz. Above 6000 Hz, the velocity spectra increase by about 15 dB. However,

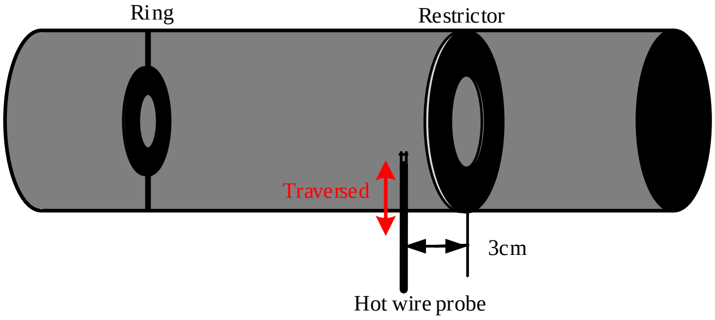

Figure 5.18: Experimental arrangement of turbulence flow measurement upstream of the restrictor with a ring installed.

in front of the restrictor, the velocity spectra only increases by about 4 dB. At the separation distance of 92 cm, the increase in the velocity in the wake is about 5 dB in the frequency range up to 6000 Hz. Above 6000 Hz, the velocity spectra increase by about 10 dB. For the flow in front of the surface of the restrictor, the velocity spectra increase by less than 1 dB.

On the downstream side of the restrictor d=55 mm, the difference in the velocity spectra mainly occurs in the 'jet flow' of the restrictor. At the separation distance of 11 cm, the level of the velocity spectra increases by about 8 dB in the plane wave frequency range. Above 2000 Hz, the level of the velocity spectra increases by more than 15 dB. At the larger separation distances, the velocity spectra of the 'jet flow' shows a similar increase, only with smaller levels. However, at all three separation distances the difference in velocity spectra behind the restrictor is similar and approximately 2 dB.

The difference in the velocity spectra at the critical separation distances shown in Table 5.3 is different for the restrictor with different internal diameters, especially in the wake of the ring. However, the difference in the velocity spectra in front of, or behind the restrictor surface, is similar. Considering interaction noise generation at the critical separation distances, we assume that only the turbulence impinging on the surface of the restrictor is important for the generation of interaction noise. Since we cannot be certain which regions of the restrictor are most efficient in noise radiation we compute the velocity spectra averaged over the restrictor surface area A_r. This area averaged velocity spectrum $\phi_{uu}^{A_r}(f)$ can be obtained from the radial variation of velocity spectra from the area-weighted sum given by

$$\phi_{uu}^{A_r}(f) = \frac{1}{A_r}\sum_{i=1}^{N}\phi_{uu}(r_i,f)A(r_i), \tag{5.3}$$

where N is the total number of measurement points, $A(r_i)$ is the annular surface area of the restrictor at measured position r_i.

In this section the area-averaged velocity spectra is used to collapse the sound power spectra of the interaction noise for the different rings installed upstream of the same

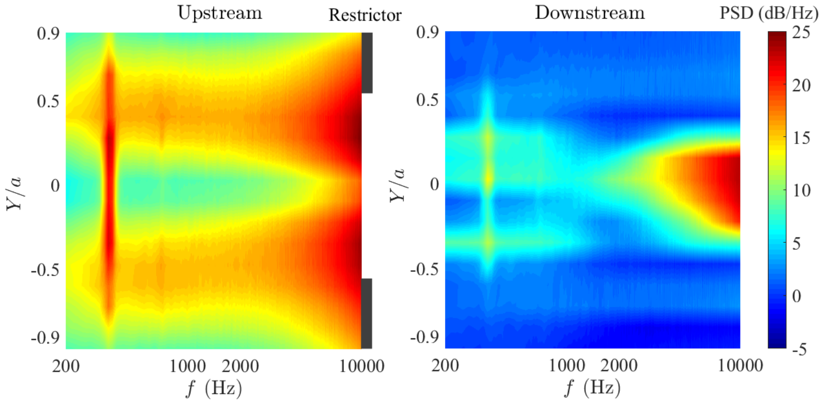

(a) L=11cm.

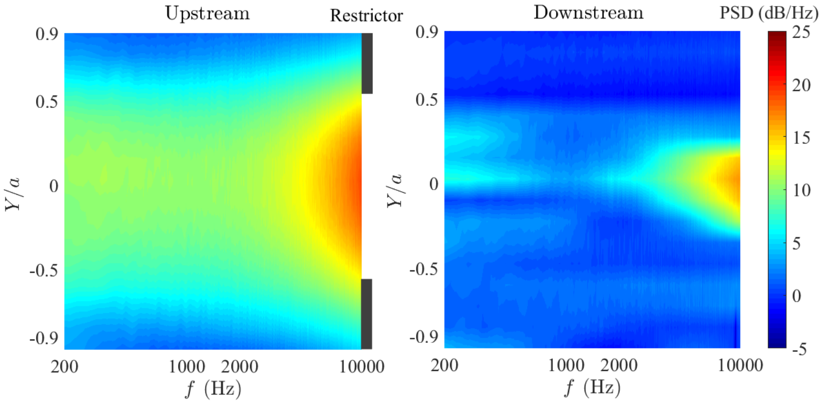

(b) L=36cm.

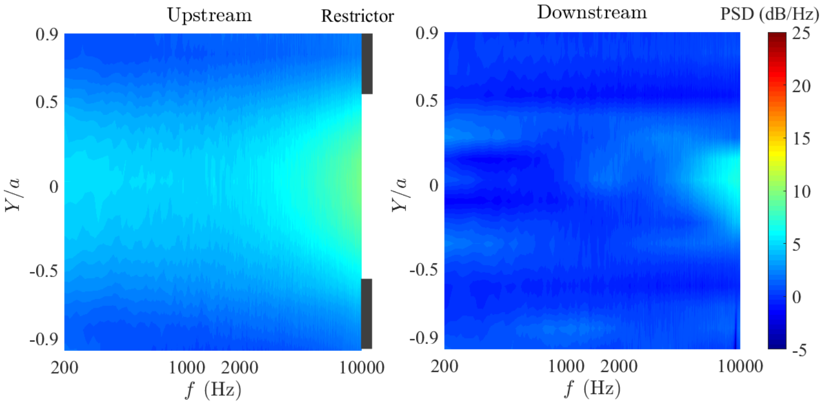

(c) L=92cm.

FIGURE 5.19: Difference of the velocity spectra with and without ring in front of the restrictor d=55mm in dB under a mean flow speed of 15.0 m/s.

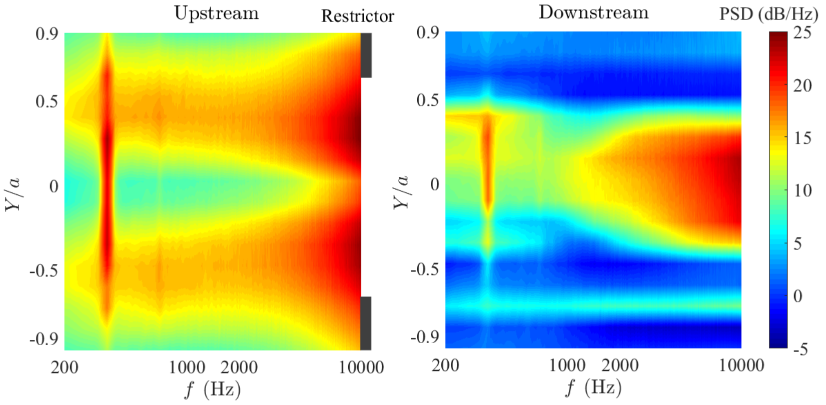

(a) L=11cm.

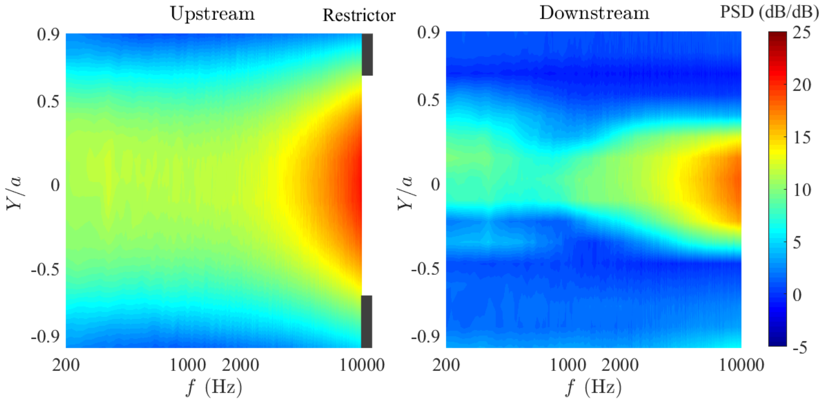

(b) L=29cm.

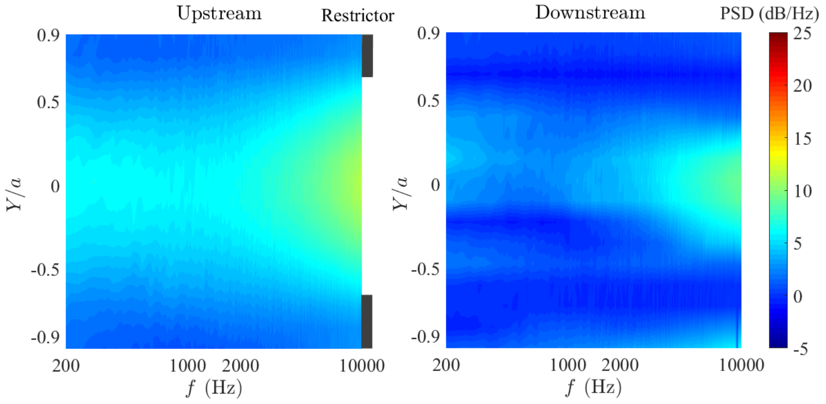

(c) L=80cm.

FIGURE 5.20: Difference of the velocity spectra with and without ring in front of the restrictor d=65mm in dB under a mean flow speed of 15.0 m/s.

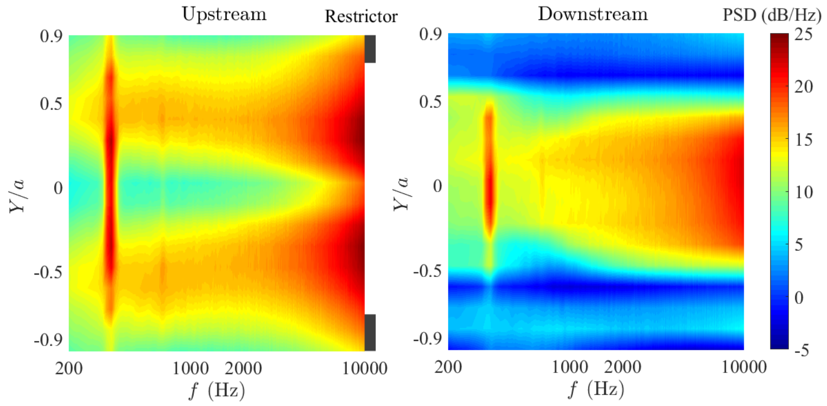

(a) L=11cm.

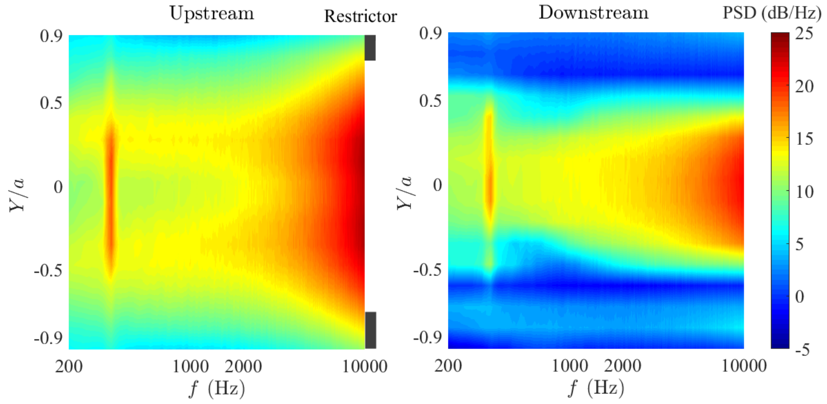

(b) L=17cm.

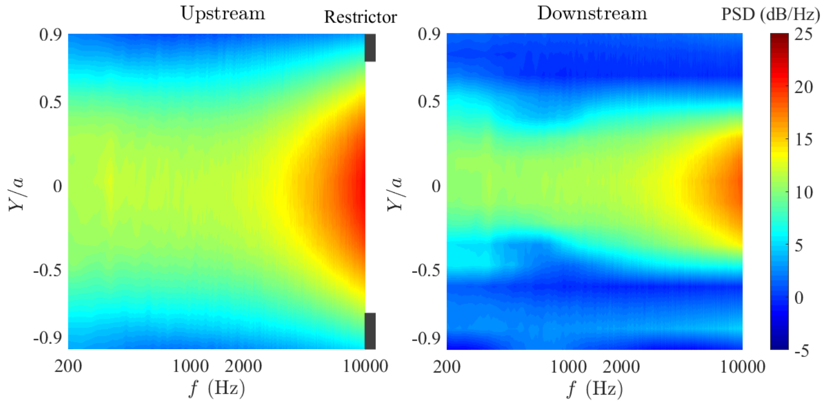

(c) L=29cm.

FIGURE 5.21: Difference of the velocity spectra with and without ring in front of the restrictor d=75mm in dB under a mean flow speed of 15.0 m/s.

restrictor. A representative result is shown in Figure 5.22 at a mean flow speed of 10.8 m/s. Figure 5.22(a) presents the PWL spectra of interaction noise W_i of the d=55 mm restrictor with four rings 1,2, 3 and 4 installed 11 cm upstream. The corresponding area-averaged velocity spectra are plotted in Figure 5.22(b). In both these figures the spectra can be seen to be reasonably parallel in the plane wave frequency range but diverge very slightly at higher frequencies. This suggests that the influence of the ring is simply to alter the mean square velocity without a significant change in turbulence integral length-scale, which will have the effect of altering the rate of decay of the turbulence spectra.

Figure 5.22(c) shows the result of dividing the noise spectra of Figure 5.22(a) with the velocity spectra of Figure 5.22(b). Note that no attempt has been made to non-dimensionalise this result as the purpose here is just to establish the proportionality between the noise and velocity spectra. Reasonably good collapse of the spectra to within about 3 dB is obtained in the plane wave frequency range for the four rings with the same restrictor. Above the first cut-on frequency, interaction noise collapses within 5 dB. One exception is ring 4 which presents the largest blockage to the flow. The reason for this is not clear but may be due to contamination by jet noise.

In this section the relationship between the turbulence velocity spectra generated by the ring and the mean flow speed in the duct is investigated in an attempt to be able to predict interaction noise at any arbitrary flow speed. Our data suggests that the velocity PSD is proportional to the square of the mean flow speed, as shown in Figure 5.23. Figure 5.23(a) shows the area-weighted velocity spectra measured at the two mean flow speeds of 10.0 and 15.0 m/s. The difference between the two spectra is about 5 dB across the frequency range. Good collapse of the area-weighted velocity spectra is obtained in Figure 5.24(b) by dividing by the mean flow velocity thererby confirming that $\bar{u}^2 \propto U^2$, except in the higher frequency range where deviation between the spectra of up to 3 dB is observed.

The analysis above has suggested that the interaction noise is proportional to the area-weighted velocity spectrum, whose spectral shape for the same wake generator is independent of mean flow speed. Moreover, it has been found that the influence of the restrictor to the interaction noise can be accounted for by the square of the drag coefficient. A semi-empirical model is therefore proposed for the interaction noise sound power spectrum $W_i(f)$ in a unit frequency bandwidth that is analogous to the model of Equation 4.22 developed in Section 4.2 for the self-noise spectrum of the form

$$W_i(f) = K_{Gi}(f)\frac{\rho A_r}{4{c_0}^3}C_d^2 U^4 \phi_{uu}(f). \tag{5.4}$$

where $K_{Gi}(f)$ is defined similarly to Equation 4.22 for the self-noise radiation and is a non-dimensional factor that describes the spectral shape of interaction noise.

Equation 5.4 was used to attempt to collapse the data for eighteen different interaction

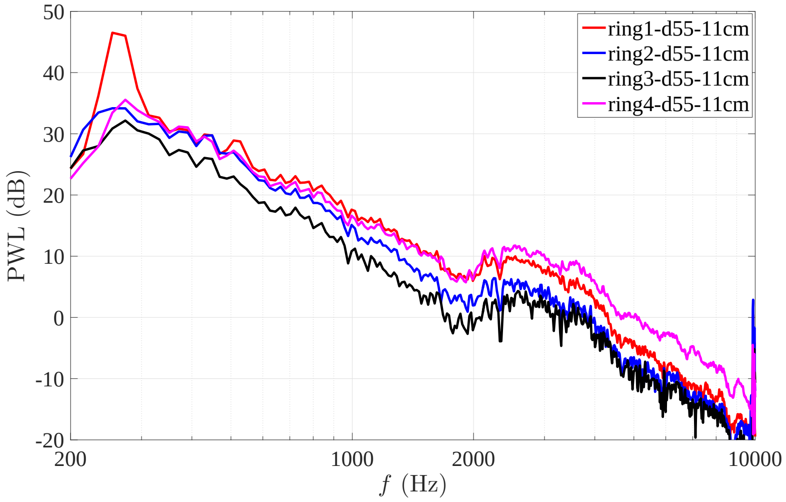

(a) Spectra of interaction noise.

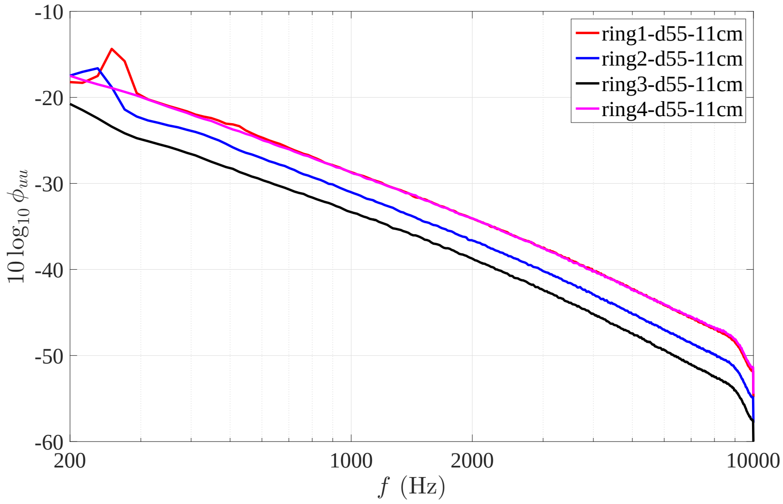

(b) Spectra of area weighted velocity spectra.

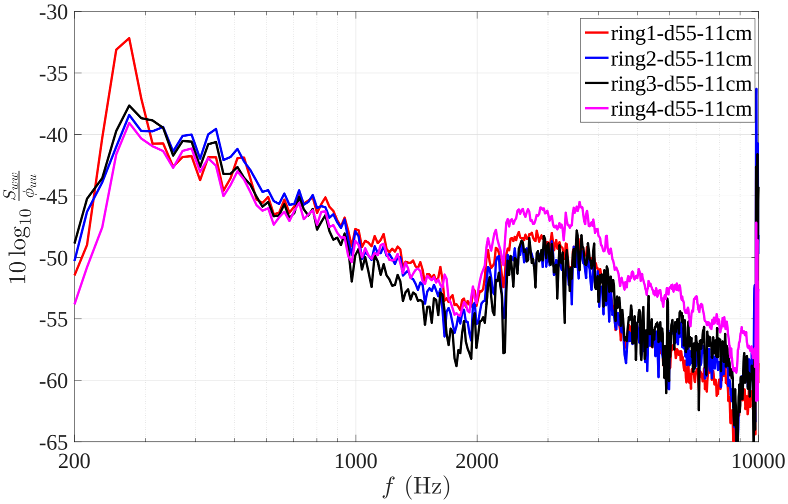

(c) Interaction noise spectra divided by the area weighted velocity spectra.

FIGURE 5.22: Interaction noise spectra divided by the area weighted velocity spectra for the case of different rings installed 11 cm upstream of d=55 mm restrictor with a mean flow velocity of 10.8 m/s.

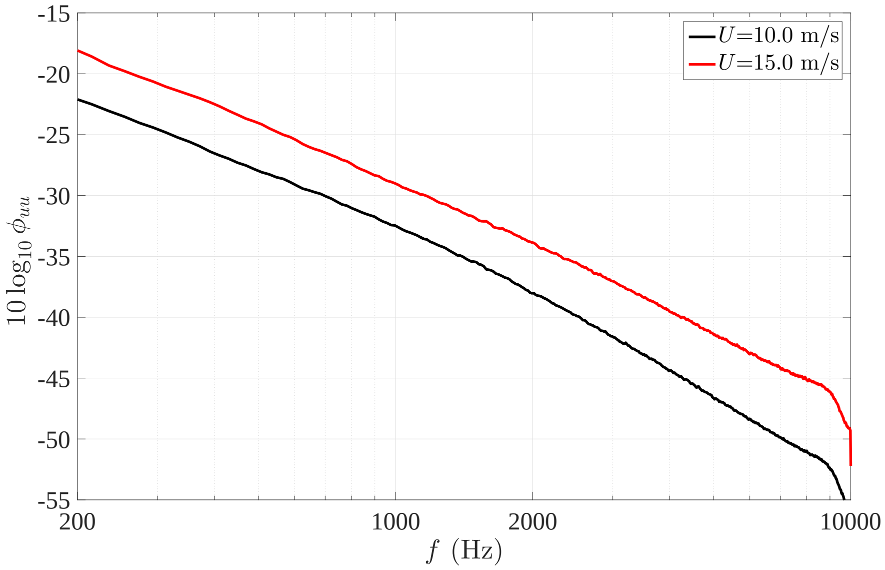

(a) Area weighted velocity spectra under different mean flow speeds.

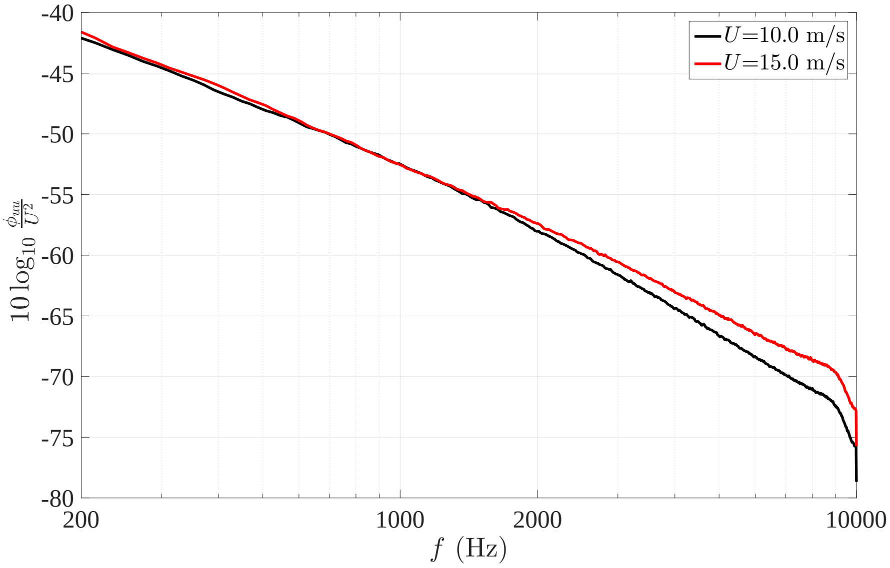

(b) The collapse of the area weighted velocity spectra.

FIGURE 5.23: Collapse of the averaged velocity spectra using the mean flow speed in the duct.

noise sound power spectra obtained for different combinations of the four rings, 1, 2, 3, 4, installed 11 cm upstream of the three different restrictors, d=55 mm, d=65 mm and d=75 mm at the two mean flow speeds of 10.0 m/s and 15.0 m/s. Without normalisation the interaction noise spectra varies by up to 30 dB. After computing the non-dimensional spectral density $K_{Gi}(f)$ from Equation 5.4, good collapse is now obtained within 5 dB in the frequency range between about 700 Hz and 3500 Hz. Below 700 Hz, the data is affected by vortex shedding noise due to the ring. Above 3500 Hz, the curves deviate for which there are two main reasons. First, in the high frequency range, the interaction noise is negligible compared to the self-noise for some cases, as seen from the large fluctuations in the spectra. Second, the collapse of the averaged velocity spectra using the mean flow speed in the duct is not satisfactory in this frequency range, as shown in Figure 5.23.

It is also found from Figure 5.24(b) that the normalised spectra $K_{Gi}(f)$, which may be interpreted as being due to the restrictor response, has an identical frequency power law of f^{-2} as the non-dimensional self-noise spectra K_τ in the plane wave frequency range.

5.7 Turbulence decay in the duct

The previous section shows that the interaction noise is strongly related to the turbulent velocity spectra averaged over the restrictor surface area. As shown in Section 5.6.1, the turbulence level at the restrictor is determined by the characteristics of the upstream turbulence generator, in this case the ring, and the separation distance between the element and the restrictor due to the decay of turbulence as it convects down the duct. In this section, the effects on the turbulent velocity spectra of the ring and its separation distance from the restrictor are investigated.

The development of turbulence downstream of ring 4 was measured to investigate the turbulence decay rate along the duct. Colour maps of the velocity spectra versus frequency and radial positions for ring 4 is shown in Figure 5.25. Velocity colour maps are presented for 7 different axial separation distances at a mean flow speed of 15.0 m/s. For comparison, the colour maps of the velocity spectra of the empty duct are also plotted in Figure 5.25(h).

The colour maps of the velocity spectra shown below for ring 4 can be seen to be different to the colour maps obtained from ring 1 shown in Figure 5.3. The two velocity maps are most different at separation distances less than 52 cm, suggesting that the flow state within this separation distance is mainly determined by the ring geometry. At larger separation distances of 72 cm and 92 cm, the velocity spectra for both rings become comparable to the turbulence levels of the empty duct and hence interaction noise levels are weak. Turbulence is therefore observed to decay slowly along the duct and the separation distances were insufficiently large to observe the fully developed

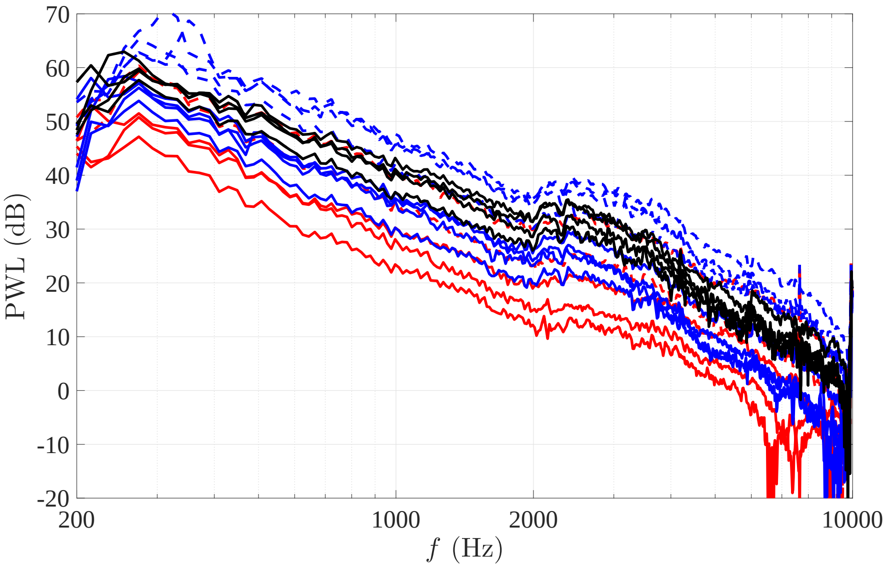

(a) Spectra of interaction noise.

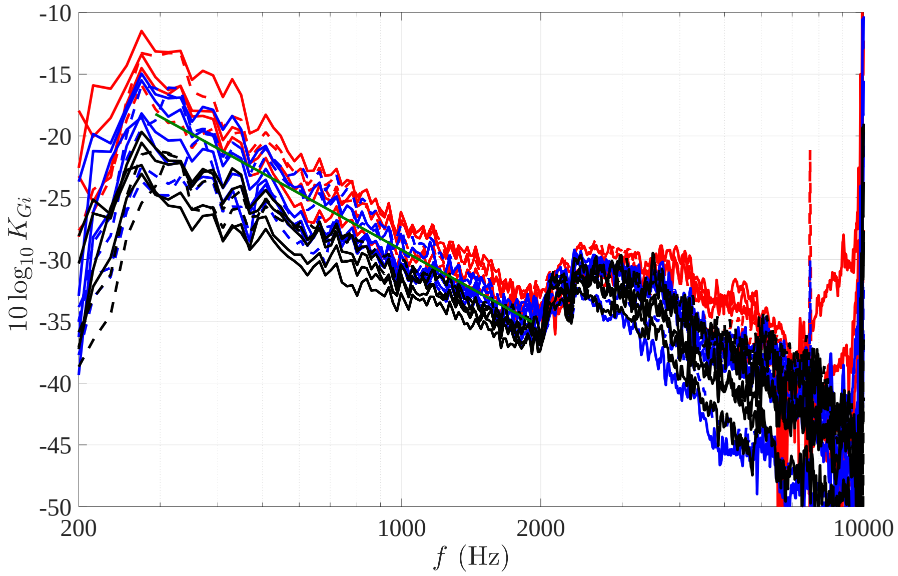

(b) The collapse of the interaction noise spectra.

FIGURE 5.24: The overall collapse of the interaction noise using Equation 5.4.

state. However, at these large separation distances, interaction noise is comparatively weak compared to the self-noise.

The decay of wake turbulence down the duct is seen more clearly in Figure 5.26 in which the variation in mean square velocity is plotted in dB against separation distance for two rings ring1 and ring4. Very different rates of decay are observed with the turbulence from ring 1 decaying at a much faster decay rate than ring 4 until about 65 cm downstream. It is therefore not possible to generalise the behavior of the wake turbulent decay as the restrictor is generally located in the near wake of the in-duct element where a fully developed state is not established. Above a certain distance the turbulence is approaching the levels of the background turbulence, as shown in Figure 5.26 by the dash line.

Another complication in trying to predict the turbulence generated by the ring is that it is affected by the presence of the downstream restrictor. The effect on the turbulence by the restrictor is shown in colour maps of the difference in the velocity spectra in dB versus frequency and radial positions. Results plotted in 5.27 for ring 1 installed 11 cm upstream of the restrictors d=55 mm, 65 mm and 75 mm at a mean flow speed of 15.0 m/s. The velocity spectra due to the different restrictors near the duct centre line is observed to be more than 2 dB, which can be attributed to the different flow speeds due to the different restrictor blockages. This is clearly shown in the different frequencies of the narrow band peaks due to the vortex shedding of the ring. The difference of the velocity spectra for other frequencies is smaller than 1 dB, suggesting that over most of the frequency range the restrictor size has negligible effect on turbulence generation by upstream elements.

5.8 The relationship between the self-noise model and the interaction model

In this section, the self-noise model as shown in Equation 4.22 and the interaction noise model as shown in Equation 5.4 are compared to investigate the relationship between the self-noise and interaction noise. The ratio between the self-noise and the interaction noise can be expressed as

$$\frac{W_i(f)}{W(f)} = \frac{K_{Gi}(f)}{K_G(f)} \frac{(1-\beta)^2 \beta^4 A_r \phi_{uu}(f)}{\pi^2 a^2 U^2}. \tag{5.5}$$

Figures 4.11(a) and 5.24 show that in the plane wave frequency range, both non-dimensional self-noise spectra K_G and non-dimensional interaction noise spectra K_{Gi} follow a f^{-2} scaling law. Therefore, in Equation 5.5, $\frac{K_{Gi}(f)}{K_G(f)}$ is frequency independent in the plane wave frequency range. Together with the definition of the turbulence intensity Tu shown in Equation 2.11, Equation 5.5 can be simplified to

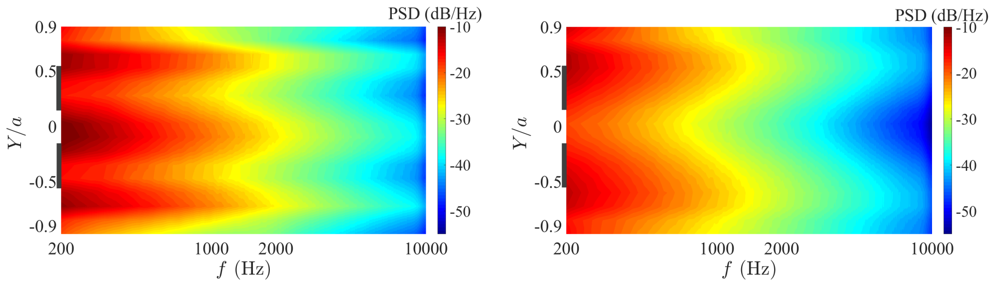

(a) L=7 cm. (b) L=12 cm.

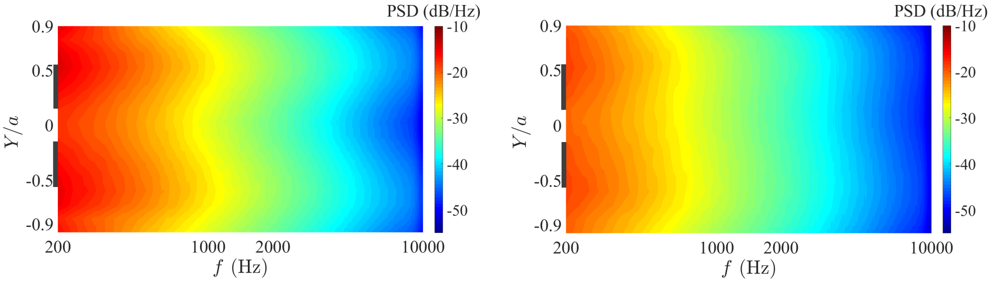

(c) L=17 cm. (d) L=27 cm.

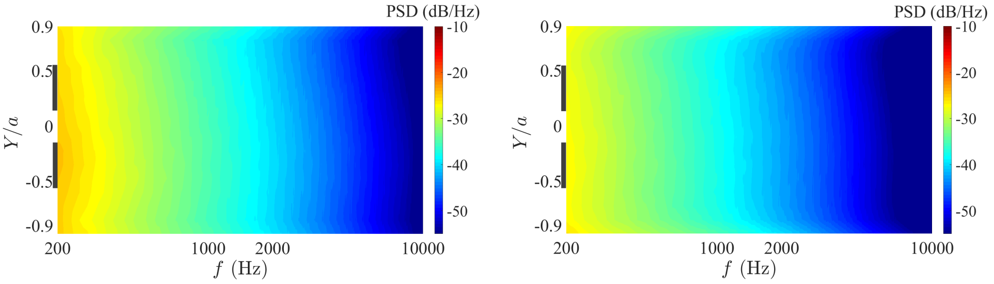

(e) L=52 cm. (f) L=72 cm.

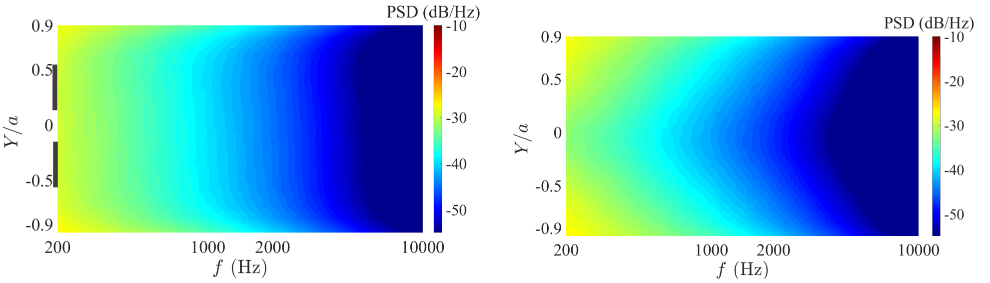

(g) L=92 cm. (h) Empty duct

FIGURE 5.25: Velocity spectra downstream of the ring 4 and the velocity spectrum of the empty duct under a mean flow speed of 15.0 m/s.

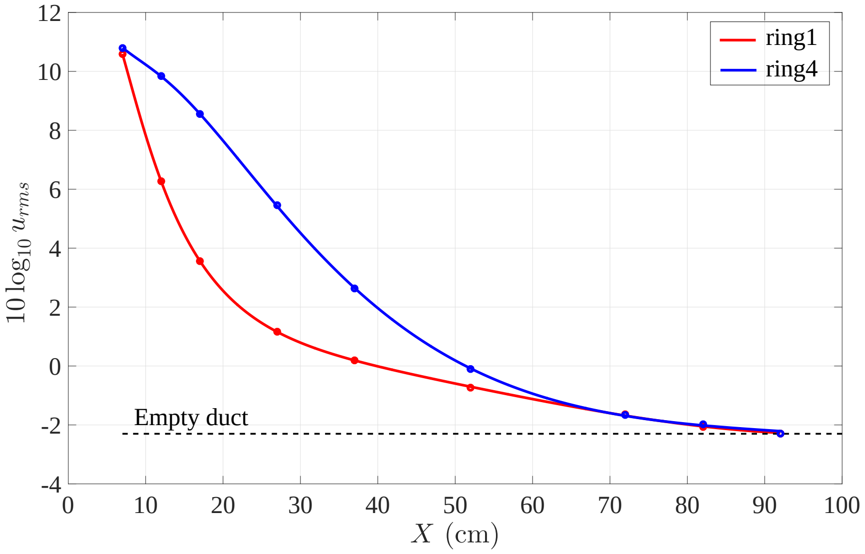

FIGURE 5.26: Turbulence decay downstream of ring 1 and ring 4. X is the distance downstream of the ring. The level of u_{rms} in the empty duct was plot as the background turbulence level.

$$\frac{W_i(f)}{W(f)} = \frac{K_{Gi}}{K_G} \frac{(1-\beta)^2\beta^4(1-\beta^2)Tu(f)^2}{\pi}. \tag{5.6}$$

Equation 5.6 represents the effects of the turbulence intensity and diameter ratio on the relative level of the interaction noise and self-noise. Figure 5.28 represents the PWL difference between the interaction and self-noise in the plane wave frequency range under different turbulence intensity ranging from 0.01 to 0.7. The range of the diameter ratio of the restrictor is 0.5< β <0.8. It shows that when the turbulence intensity is lower than 0.2, the interaction noise generation is negligible. When the diameter ratio is 0.6, the relative level of the interaction noise is highest compared to the self-noise. This is consistent with the results shown in Figure 5.9(a).

5.9 Summary

The noise generated due to upstream turbulence interacting with the restrictors of various internal diameters has been investigated experimentally. The effects of mean flow speed, restrictor dimensions, and the turbulence spectrum on interaction noise have been investigated. A semi-empirical model for the prediction of interaction noise has been developed and shown to be in good agreement with measured noise spectra over a range of parameters. Finally, the development of the turbulence flow in the duct has been discussed. The principle findings in this chapter are:

- Interaction noise is generated by an increase in surface pressure over the restrictor due to turbulent flow impinging on the restrictor. Upstream turbulence was found

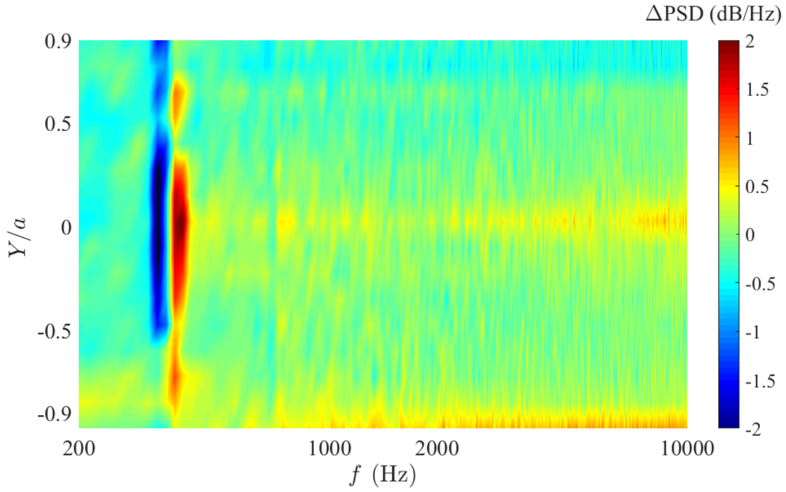

(a) d=55 cm and d=65 cm restrictor.

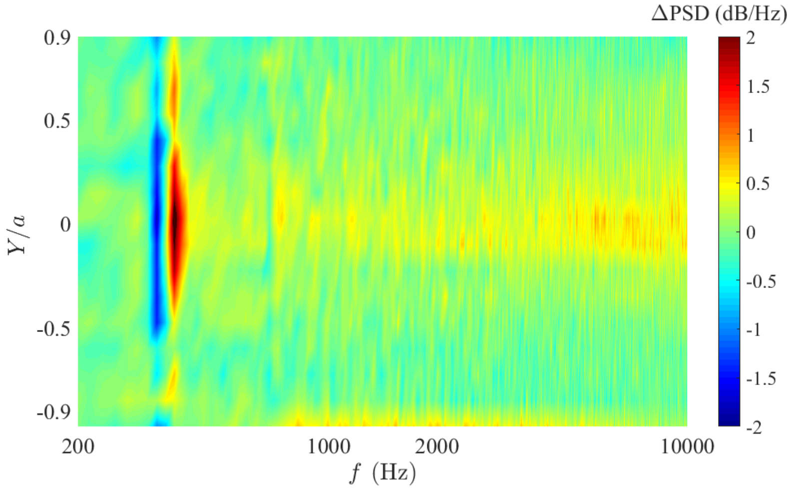

(b) d=65 cm and d=75 cm restrictor..

Figure 5.27: Velocity spectra difference between two different sized restrictor with the same ring installed 11 cm upstream.

to cause an increase in surface pressure on both sides of the restrictor, and has a greater effect on the upstream surface than the downstream surface.

- Interaction generation is found to be most prominent in the plane wave frequency range, which we have shown is directly related to the upstream turbulence spectrum.

- Unlike restrictor self-noise, the velocity scaling law for interaction noise does not deviate too far from U^6 . This scaling comprises two factors, one from the turbulence velocity scaling $u_{rms}^2 \propto U^2$, the second from the velocity scaling of the restrictor response U^4.

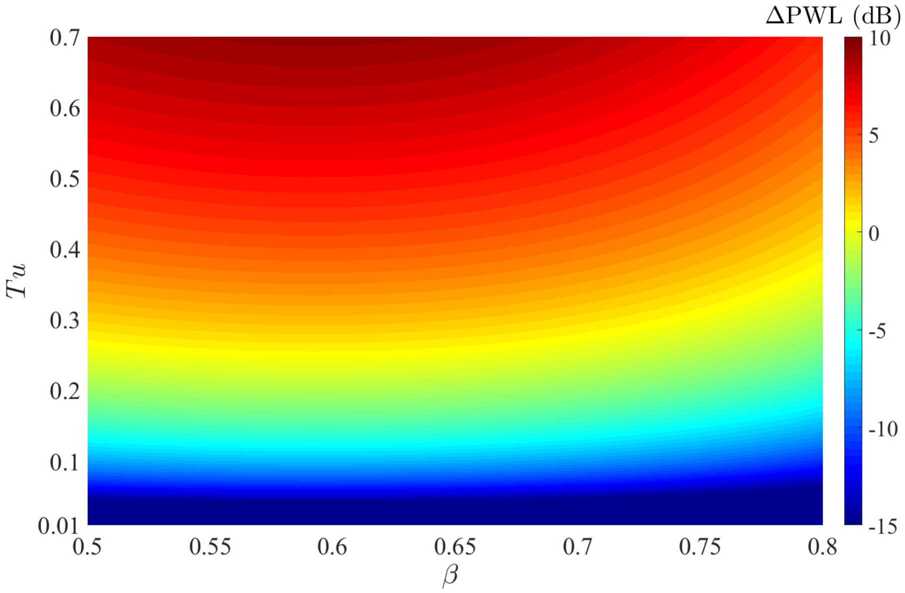

FIGURE 5.28: Difference of interaction noise PWL and self-noise PWL in the plane wave frequency range for different restrictors under different turbulence intensity.

- The restrictors with the smallest internal diameters generate highest levels of interaction noise. It has been found that, like the self-noise, interaction noise also scales with the restrictor drag coefficient as C_d^2 .
- Within a certain downstream distance the decay of the turbulence velocity in the duct is determined by the characteristics of the in-duct element. Downstream of this distance, the decay of the turbulence is independent of the in-duct element where a self preserving state is approached. However, the restrictor has little effect on the upstream turbulence level at these separation distances.

It is found in this chapter that the separation distance between the restrictor and the turbulence generating in-duct elements is important for determining interaction noise generation. A semi-empirical expression has been derived that allow the turbulence intensity over the restrictor surface to be determined whereby interaction noise is comparable to the self-noise.

The main limitation of the model for interaction noise prediction developed in this chapter is that the turbulence velocity fluctuations are not easy to measure or predict for realistic in-duct elements.

Chapter 6

Reduction of noise generation by the restrictor

6.1 Introduction

In previous chapters, the mechanisms and characteristics of self-noise generation and interaction noise generation by single-hole restrictors were presented. It was concluded that the pressure fluctuations on the surface of the restrictor due to interaction with turbulent flow is the main noise source. In this chapter some simple measurements are made to investigate the possibility of reducing the noise generated by the restrictor by introducing roughness onto the surface of the restrictor to reduce the surface pressure fluctuations. The experimental results in this chapter also verify the conclusions made in the previous chapters about the noise generation mechanisms.

6.2 Effects of the surface roughness on restrictor self-noise

Surface roughness was introduced onto the restrictor surface by glueing to the surface of the restrictor carborundum grit with an average diameter of about 0.3 mm, as shown in Figure 6.1. Note that the area not covered in grid is sandwiched in between the two flanges of the connecting pipes. To investigate which side of the restrictor is most important for overall noise generation, surface roughness was introduced separately on the upstream and downstream sides and its effects on noise generation were measured through the sound power measurements.

The difference of the PWL spectra between the self-noise of the restrictor without grit and with grit on the upstream surface or downstream surface is shown in Figure 6.2 for the restrictor with an internal diameter of 65 mm under a mean flow speed of 10.0 m/s. It shows that introducing grit on the downstream side makes no significant difference to the total radiated self-noise.

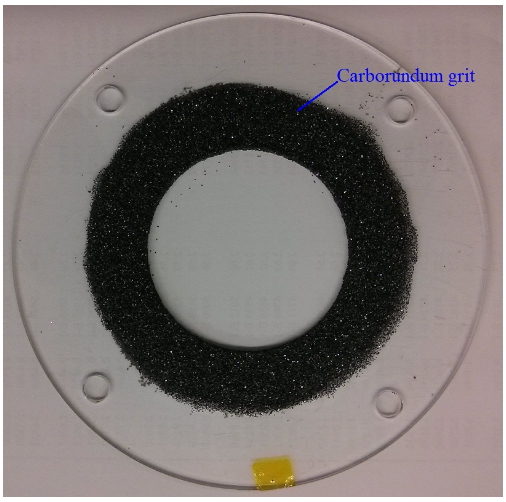

FIGURE 6.1: Picture of the restrictor with rough surface.

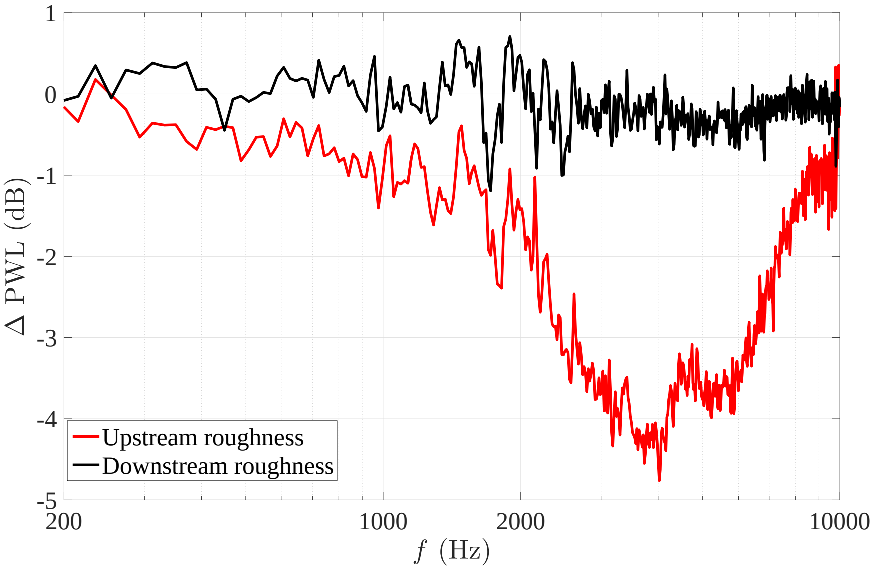

FIGURE 6.2: Reduction of the radiated sound power with upstream rough surface and downstream rough surface. The internal diameter of the restrictor in the test case is 65 mm and the mean flow speed is 10.0 m/s.

However, increasing the roughness on the upstream surface of the restrictor is seen to reduce self-noise generation. Figure 6.2 shows that the radiated sound power in the plane wave frequency range decreases by less than 1 dB for the restrictor with rough upstream surface. At the frequencies between 2500 Hz and 6500 Hz, the noise decreases more than 3 dB. At other frequencies above the first cut-on frequency, the noise decreases more than 1 dB. It is therefore concluded that increasing the roughness of the upstream surface of the restrictor leads to noise reductions only above the first cut-on frequency.

According to the results in section 3.6.2.5, the main noise source above the first cut-on frequency is the surface pressure fluctuations near the upstream inner edge of the restrictor. As increasing the restrictor surface roughness mainly leads to noise reductions

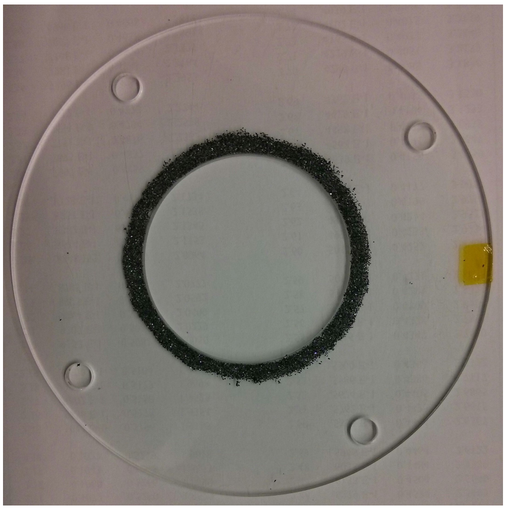

FIGURE 6.3: Picture of the restrictor with rough surface near the inner edge.

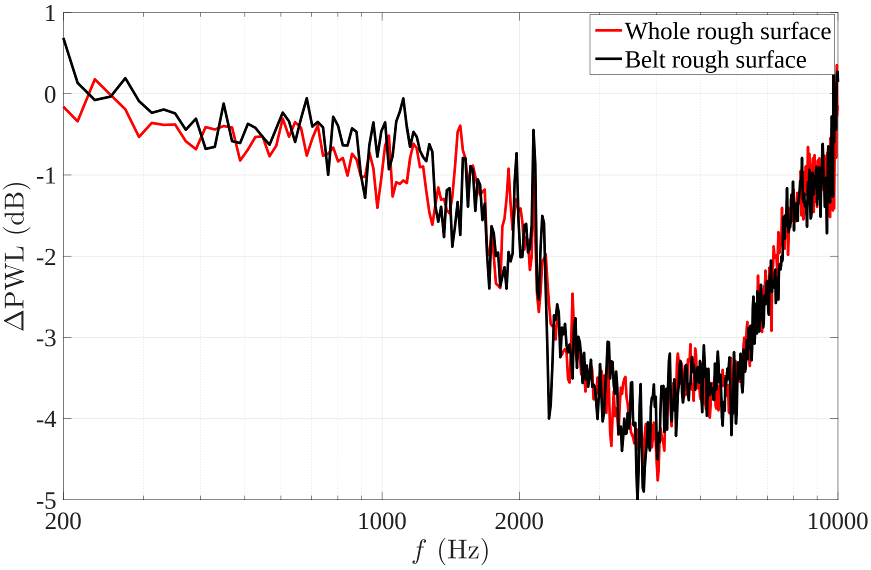

FIGURE 6.4: Comparison of the radiated sound power between the restrictor with a rough surface and a rough belt near the inner edge. The internal diameter of the restrictor in the test case is 65 mm and the mean flow speed is 10.0 m/s.

above the first cut-on frequency, another test was undertaken in which grit was only included near the inner edge of the restrictor on the upstream side, as shown in Figure 6.3. The difference of the power spectra between the restrictor without grit and the restrictor with grit near the upstream inner edge is shown in Figure 6.4. Similar noise reductions are obtained to those when the entire restrictor area was covered with grit.

It will be shown below that increasing the upstream surface roughness leads to a reduction in the drag coefficient of the restrictor. As a result, at the same mean flow speed, the pressure drop across the restrictor with rough upstream surface is smaller than the restrictor with smooth surface. As the purpose of the restrictor is to obtain a pressure drop in the ADS, no reduction in pressure drop due to the restrictor is desirable. In

Table 6.1: The pressure drop of different restrictors under a mean flow speed of 10.0 m/s

Test cases	Pressure drop (Pa)
Restrictor d=65 mm, smooth surface	314
Restrictor d=65 mm, grit surface	304
Restrictor d=63 mm, grit surface	319

chapter 4, it was shown that noise generation of the restrictor is strongly related to the pressure drop across it. To ensure that the noise reductions reported above is not accompanied by a decrease in pressure drop, a restrictor with a rough upstream surface and an internal diameter of 63 mm was manufactured to maintain the same pressure drop as the restrictor with 65 mm internal diameter but with a smooth upstream surface.

A comparison of the pressure drops across the 65 mm diameter restrictors with and without surface roughness and a restrictor with rough surface of 63 mm internal diameter at a mean flow speed of 10.0 m/s is shown in Table 6.1. The pressure drop across the restrictor d=63 mm with rough upstream surface is measured to be 5 Pa (1.6%) higher than the restrictor with smooth upstream surface with an internal diameter of 65 mm. The corresponding reductions in sound power for the restrictors d=63 mm and d=65 mm with rough upstream surface are shown in Figure 6.5. In both cases the radiated sound power are compared to the radiated sound power of restrictor d=65 mm with a smooth upstream surface. The rough-surface restrictor of d=63 mm is observed to have very similar noise reductions to the rough surface restrictor of d=65 mm. It is therefore concluded that increasing the upstream surface roughness of the restrictor can reduce the restrictor self-noise above the first cut-on frequency whilst maintaining the pressure drop.

6.3 Effects of the surface roughness on interaction noise generation

In this section the effects of surface roughness on the interaction noise generation is investigated. Figure 6.6 presents a comparison of the total noise reduction between the smooth surface restrictor and the rough surface restrictor with ring 1 installed 11 cm upstream of two restrictors. The mean flow speeds in the two test cases were both 10.0 m/s. The reduction in the self-noise obtained by increasing the restrictor surface roughness is also plotted to allow comparison. It shows that the total noise reduction has a similar frequency dependence to that for the self-noise reduction shown in Figure 6.2 but is about 1 dB lower. The reduction in total noise generation is therefore most likely due to reductions in the self-noise reduction suggesting that introducing roughness has negligible effect on the interaction noise. In Chapter 5, it is concluded that interaction noise generation is consistent with an increase in the surface pressure over the restrictor,

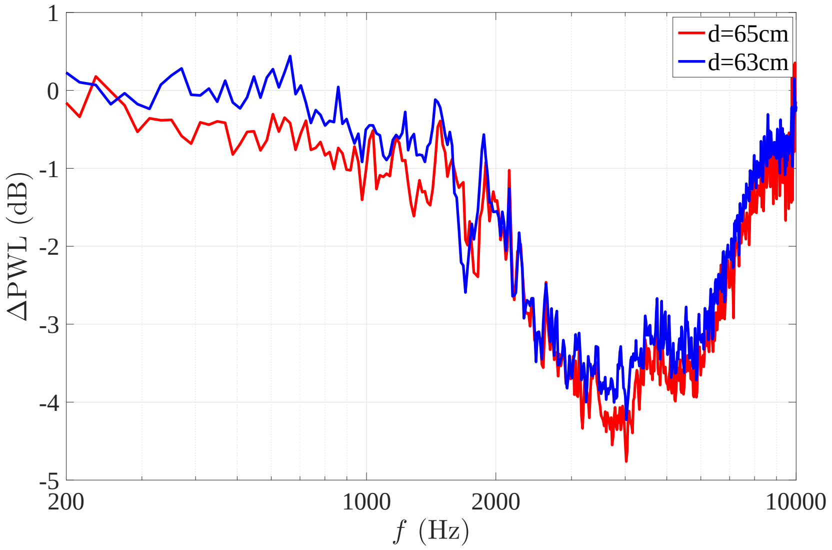

FIGURE 6.5: Reduction of the radiated sound power after the adjustment of the internal diameter. The mean flow speed was 10.0 m/s.

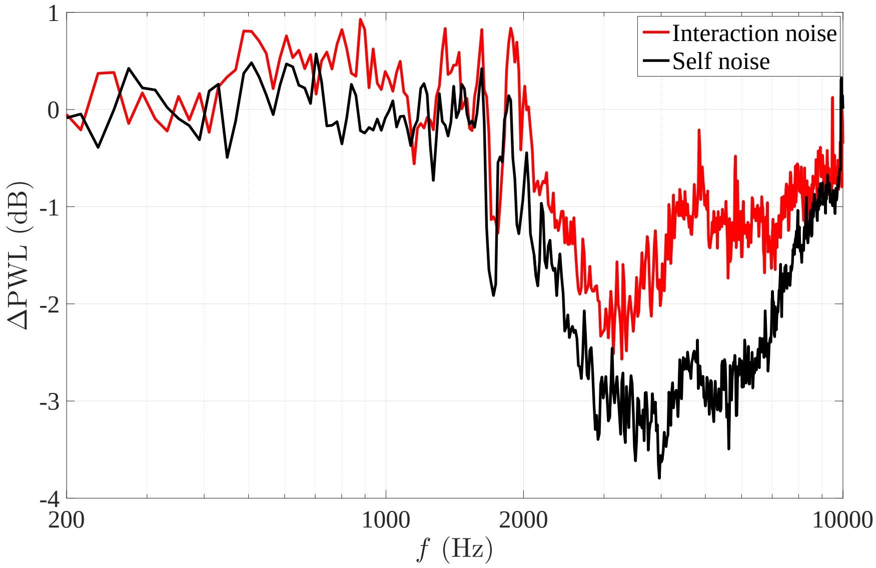

FIGURE 6.6: Reduction of the radiated sound power of interaction noise. In this test cases, ring1 was installed 11 cm upstream of the restrictor with an internal diameter of 65 mm . The mean flow speed was 10.0 m/s.

which is determined by the upstream turbulence. Therefore, for the restrictor with rough and smooth surfaces, the increase in surface pressure should be identical in both cases for the same level of upstream turbulence, which is investigated in the next section.

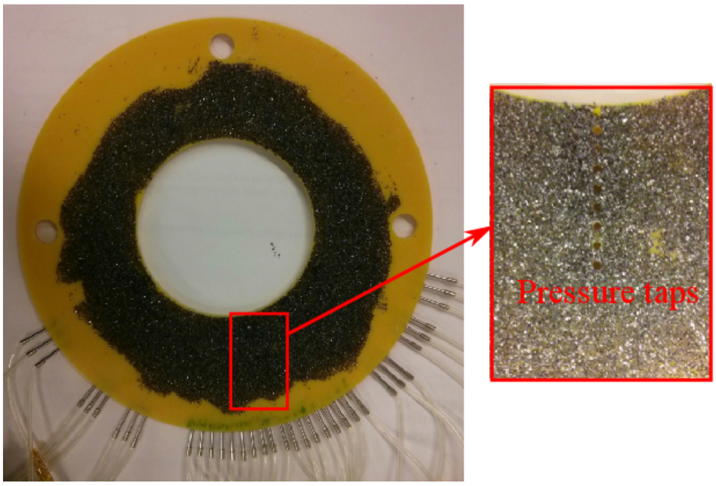

Figure 6.7: Restrictor with grit surface for the surface pressure measurement.

6.4 The surface pressure variation with grit surface

In this section, the surface pressure of the restrictor with rough upstream surface is measured to investigate the mechanisms of noise reduction for both self-noise and interaction noise. A photograph of the restrictor used in the surface pressure measurement is shown in Figure 6.7. It should be noted that due to the glueing of the grit on the surface, the surface pressure measurement may be slightly affected due to the location of the pressure tap below the grit.

Figure 6.8 presents colour maps of the difference in the surface pressure spectral level between the restrictor with smooth and rough upstream surfaces versus frequency and radial positions. As before, the difference in the spectra mostly occurs above the first cut-on frequency, with about a 6 dB reduction in the surface pressure except near the inner edge of the restrictor. In this inner wall region, the reduction in surface pressure is about 3 dB. This surface pressure reduction is consistent with the radiated sound power reduction shown in Figure 6.2.

Figure 6.9 presents the difference in the surface pressure spectral level between the restrictor with smooth upstream surface and the restrictor with grit located near the upstream inner edge. As before when the entire surface was covered with grit the difference in the spectra also mainly occurs above the first cut-on frequency. The variation of the surface pressure shows a similar behaviour to the restrictor whose total upstream surface is made rough. This might be the reason for the similar noise reductions of the two restrictors.

Figure 6.10 presents the difference in the surface pressure variation with frequency and radial positions with ring 1 installed 11 cm upstream between the restrictor with smooth upstream surface and rough upstream surface. The difference in increased surface pressure is within 1 dB between the two cases. This may explain why introducing grit on the upstream surface is not effective in reducing interaction noise.

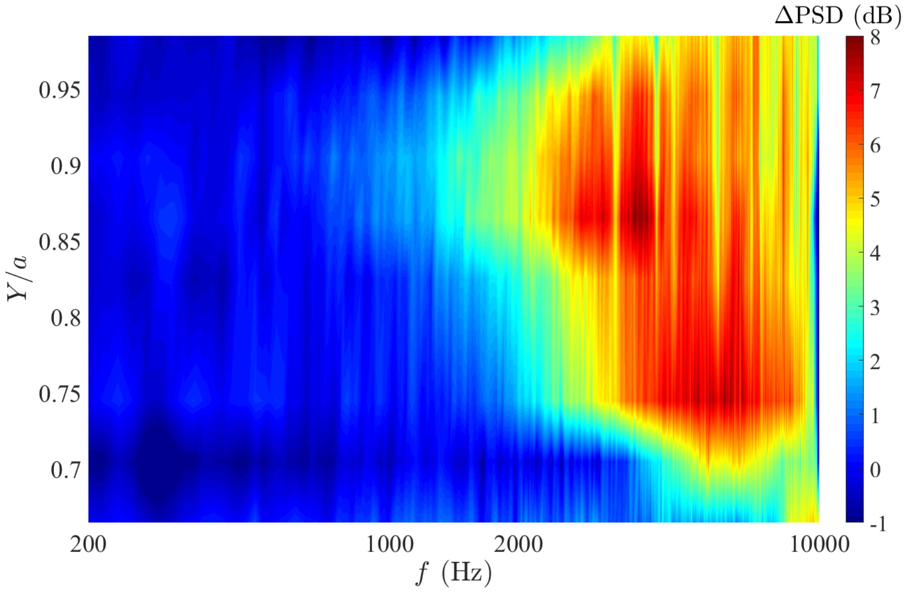

FIGURE 6.8: Difference of the surface pressure spectra between the restrictor with smooth upstream surface and the restrictor with whole grit upstream surface. The internal diameter of the restrictor was 65 mm and the mean flow speed was 10.0 m/s.

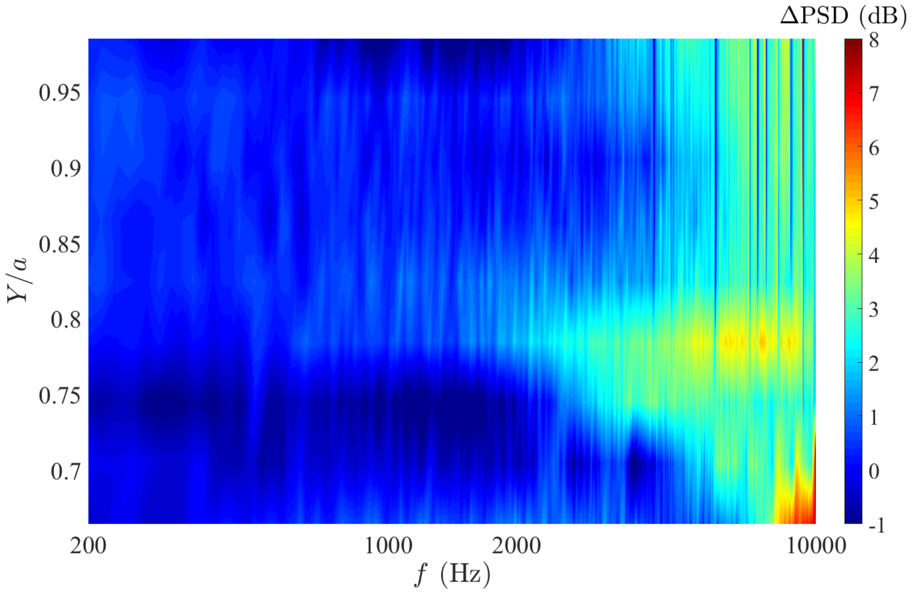

FIGURE 6.9: Difference of the surface pressure spectra between the restrictor with smooth upstream surface and the restrictor with belt grit upstream surface. The internal diameter of the restrictor was 65 mm and the mean flow speed was 10.0 m/s.

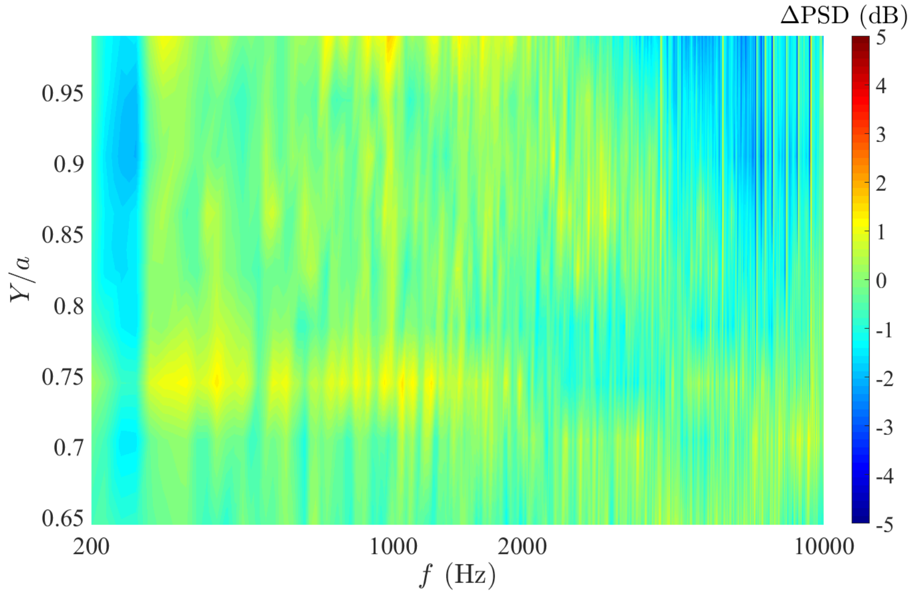

FIGURE 6.10: Difference of the surface pressure variation with ring 1 installed 11 cm upstream the smooth upstream surface restrictor and grit upstream surface restrictor. The mean flow speed was 10.0 m/s.

6.5 Summary

The noise generated by single-hole restrictors has been reduced by introducing roughness onto the upstream surface of the restrictor. This method is shown only to be effective in reducing noise above the first cut-on frequency, where 3 dB noise reductions are obtained. Surface pressure measurements were made to explain the noise reduction mechanisms. The principle findings of this chapter are:

- With increasing upstream surface roughness, single-hole restrictor self-noise is reduced by about 3 dB at frequencies above the first cut-on frequency. The increased roughness has little effect on the noise generation in the plane wave frequency range.
- The drag coefficient of the restrictor is reduced due to the introduction of surface roughness, leading to a smaller pressure drop across the restrictor. To reduce the noise but maintain the same pressure drop, the internal diameter of the restrictor should be reduced slightly. The noise generated by the restrictor with smaller internal diameter and rough surface is lower than the restrictor with larger internal diameter and smooth surface.
- The restrictor with rough surface near the upstream inner edge has a similar effect on noise generation as the restrictor whose entire surface is made rough. The increasing roughness on the upstream surface leads to a reduction in the surface pressure above the first cut-on frequency.

- Increasing the upstream roughness of the restrictor has little effect on interaction noise generation. However total noise is reduced through the reduction in self-noise.
- Introducing roughness on the downstream surface of the restrictor has little effect on the noise generation suggesting that the upstream surface is mostly responsible for self-noise generation.

Chapter 7

Conclusions and future work

This thesis describes the development and construction of an experimental rig to investigate the noise from single hole restrictors commonly used to control the flow rate in ventilation systems. The rig is used to perform an experimental study into the broadband self-noise generated when a restrictor is installed in an aircraft ventilation system. The thesis also deals with the interaction noise generated by the turbulent wake produced by in-duct elements installed in the duct and impinging on the restrictor. The thesis shows that interaction noise only exceeds the self-noise when the element is located within a certain separation distance of the restrictor, which is dependent on the upstream element and the internal diameter of the restrictor. The restrictor self-noise and the interaction noise are both investigated experimentally to improve the current understanding of the noise generation mechanisms and prediction accuracy.

Aeroacoustic measurements of the restrictor self-noise were made both inside and in the far field of the duct. The data has been used to develop two models of the restrictor self-noise sound power radiation. One is based on the surface pressure cross spectrum to compute the effective axial dipole distribution. The other is an extension of previous work and based on the static pressure drop across the restrictor. For the interaction noise the important parameters that determine the sound power radiation spectrum are studied. A semi-empirical model has been developed to predict the sound power spectrum due to interaction noise. The thesis concludes with a short study into the use of surface roughness on the upstream side of the restrictor to reduce the noise generation whilst maintaining the pressure drop across it.

The main conclusions of this thesis are now presented.

7.1 Conclusions

7.1.1 Restrictor self-noise

- In an empty duct with fully developed flow, aerodynamic noise is generated which forms the background noise levels in the duct system. These noise levels are shown to be negligible compared to the restrictor self-noise.

- In this thesis it is shown that the restrictor the drag coefficient C_d is one of the main factors that controls its self-noise sound radiation. The drag coefficient of the restrictor has been shown to be weakly dependent on the mean flow speed due to the high Reynolds number in this work and in real aircraft ventilation systems.

- The restrictor self-noise is consistent with the cross spectrum of the surface pressure difference across the restrictors. This confirms that the basic sources are axial dipoles distributed over the restrictor surface. The highest surface pressure fluctuations are observed to occur near the upstream inner corner of the restrictor.

- The surface pressure fluctuations obey a U^4 velocity scaling law whilst the radiated sound power follows a U^6 velocity scaling law. This suggests that area of the surface pressure over which is it highly correlated follows an U^2 velocity scaling law. This has been confirmed by independent measurement.

- The self-noise power spectrum is observed to follow a different shape below and above the first cut-off frequency in the duct of about 2010 Hz. Below this frequency the spectrum decays as f^{-2}. Above the first cut-on frequency the spectra are more complex as higher order modes modes contribute to the sound power radiation.

- Both radial modes and circumferential modes can be excited in the duct by the restrictor generated noise. The modal amplitudes of the sound field from restrictors with smaller internal diameter are higher than that with larger internal diameter.

- The wall pressure fluctuations are found to be about 10 dB higher in the downstream recirculation zone compared to the surface pressure on the restrictor surface. However, despite being of highest level the thesis argues that the wall pressure does not contribute to the sound field in the hard wall duct.

- The thesis has investigated the effect of the size of the restrictor on self-noise. It has been shown that noise generation is highly sensitive to the diameter ratio β. In this study β varied between 0.5 and 0.8 where the corresponding change in overall sound power was up to about 16 dB. The restrictors with smaller internal diameter radiate most noise.

7.1.2 Interaction noise generation

- Interaction noise is generated by an increased restrictor surface pressure due to turbulent flow impinging on its surface. Turbulence arriving from upstream is shown to increase the surface pressure on both sides of the restrictor but has greatest effect on the upstream surface.

- For the narrow range of in-duct elements investigated in this thesis, interaction noise power spectrum was found to be very closely proportional to the area-averaged velocity spectra of the incoming turbulent flow. The area used to average the velocity spectra is the surface area of the restrictor.

- The effect of increasing mean flow speed is to increase interaction noise generation. Similar to the restrictor self-noise, interaction noise also obeys a U^6 velocity scaling law. As the mean square velocity fluctuations are proportional to the mean flow speed, say $u \propto U$, interaction noise at different mean flow speed scales $U^4\bar{u^2}$.

- The restrictors with smallest internal diameters radiate higher levels of interaction noise and has been shown, identical to self-noise generation, to be strongly related to the square of the restrictor drag coefficient.

- Within a certain downstream distance of the in-duct element, the rate of decay of the turbulence level in the duct is determined by the charcateristics of the in-duct element. At distances beyond this near-wake distance, the decay of the turbulence is independent of the in-duct element. The restrictor has little effect on the upstream turbulence level.

7.1.3 Restrictor noise reduction

- Introducing upstream surface roughness on the restrictor has been shown to reduce the self-noise of single-hole restrictors above the first cut-on frequency by about 3 dB. Roughness has little effect on the noise generation in the plane wave frequency range.

- The restrictor drag coefficient is reduced due to the introduction of roughness on the upstream surface, leading to a smaller pressure drop across the restrictor. To reduce the noise but maintain the same pressure drop the internal restrictor diameter should be slightly reduced. The noise generated by the restrictor with smaller internal diameters and rough upstream surface remains smaller than the restrictor with larger internal diameter and smooth surface.

- The restrictor with rough surface introduced only on the upstream inner edge has a similar effect on the noise generation as the restrictor whose whole upstream surface is made rough. Introducing inner wall roughness has the effect of reducing the surface pressure above the first cut-on frequency, consistent with the reduction in radiated noise.

- Increasing the roughness on the upstream restrictor surface has little effect on interaction noise generation. However, total is reduced due to reduction in the self-noise contribution.
- The effect of downstream surface roughness of the restrictor on self-noise generation and interaction noise generation is negligible.

7.2 Future work

This section suggests possible topics for future work:

- Particle image velocimetry (PIV) measurements

  In this work, most of the aerodynamic measurements were conducted by the CTA. However, the aerodynamic measurements over the whole flow field near the restrictor using a PIV system may provide more detailed information about the flow state near the restrictor, to establish more clearly the link between the unsteady flow field and the radiated noise. For interaction noise, PIV measurement may provide better information about flow development in the duct, which may be useful for understanding the relationship between the incoming turbulence flow and surface pressure.

- Numerical simulation

  This thesis is mostly an experimental investigation into restrictor noise radiation. Computational Fluid Dynamic (CFD) may provide greater insight into restrictor noise generation mechanisms. Numerical methods can provide detailed flow field information to better understand the mechanisms of sound generation. The conclusions presented in this thesis can also be verified independently from numerical simulations.

- Improvement of the pressure drop model

  The restrictor self-noise based sound power prediction model based on the pressure drop across the restrictor presented in Chapter 4 has shown that a frequency-independent constant may be used to collapse measured sound power spectra. In the frequency range above about 5000 Hz, the collapse is poorer than in the low frequency range. A frequency-dependent constant may provide better collapse of the high frequency noise data.

- Extensive parametric study on interaction noise

  For the interaction noise investigation in this thesis, the effects of mean flow speeds, turbulence level and restrictor size on the interaction have been studied. For the turbulence level, only the size of the ring and the separation distance are used to change the turbulence level. More turbulence parameters, such as characteristic length scale, can be investigated.

- Noise reduction

  The final chapter of this thesis presents a simple investigation into noise reductions by the use of rough surfaces. A more detailed investigation is required that explores more roughness parameters such as the grit size and the internal diameter of the restrictor. Other methods could also be explored to reduce the restrictor surface pressure such as the construction of restrictors from perforated plates.

Appendix A

Normalised mode shape functions

The eigenfunctions of a cylindrical duct with hard wall is given by

$$\psi_{mn}(r,\theta) = \mathbf{J}_m(k_{rmn}r)e^{-im\theta}. \tag{A.1}$$

As the eigenfunctions defined by Equation A.1 are not unique, it is normalised as

$$\Psi_{mn}(r,\theta) = \frac{\psi_{mn}}{N_{mn}}, \tag{A.2}$$

where N_{mn} is defined such that

$$\int_A |\Psi_{mn}(r,\theta)|^2 dA = 1, \tag{A.3}$$

where $A = \pi a^2$ is the cross-sectional area of the duct. Substituting Equation A.2 into Equation A.3 gives

$$\frac{1}{N_{mn}^2}\int_A |\psi_{mn}(r,\theta)|^2 dA = 1, \tag{A.4}$$

Solving Equation A.4 gives the value of N_{mn} as

$$N_{mn}^2 = \begin{cases} A\mathbf{J}_m^2(k_{rmn}a) & \text{for} \quad m = 0, n = 0 \\ A\left(1 - \frac{m^2}{(k_{rmn}a)^2}\right)\mathbf{J}_m^2(k_{rmn}a) & \text{for} \quad m \neq 0, n \neq 0. \end{cases} \tag{A.5}$$

Bibliography

[1] ISO 5167-1: 2003. Measurement of fluid flow by means of pressure differential devices inserted in circular cross-section conduits running full– part 1: General principles and requirements.

[2] N. K. Agarwal. Identification of higher order acoustic modes in distributed pipe flow. *Journal of Sound and Vibration*, 129(1):166–167, 1989.

[3] N. K. Agarwal. Mean separation and reattachment in turbulent pipe flow due to an orifice plate. *Journal of Fluids Engineering*, 116(2):373–376, 1994.

[4] N. K. Agarwal. The sound field in fully developed turbulent pipe flow due to internal flow separation, part 2: Modal amplitude and cut-off frequencies. *Journal of Sound and Vibration*, 175(1):65–76, 1994.

[5] N. K. Agarwal. The sound field in fully developed turbulent pipe flow due to internal flow separation, part i: Wall-pressure fluctuations. *Journal of Sound and Vibration*, 169(1):89–109, 1994.

[6] N. K. Agarwal and M. K. Bull. Characteristics of the flow separation due to an orifice plate in fully-developed turbulent pipe-flow. *Eighth Australasian Fluid Mechanics Conference*, 1983.

[7] N. K. Agarwal and M. K. Bull. Acoustic wave propagation in a pipe with fully developed turbulent flow. *Journal of Sound and Vibration*, 132(2):275–298, 1989.

[8] A. Belanger, M. Meskine, B. Caruelle, and K. Debatin. Aero-acoustic simulation of a double diaphragm using lattice boltzmann method. 2005.

[9] Lindab company. Acoustic solutions: Circular straight silencer, product specification. page 30.

[10] N. Curle. The influence of solid boundaries upon aerodynamic sound. *Proceedings of the Royal Society of London. Series A, Mathematical and Physical Sciences*, 231 (1187):505–514, 1955.

[11] H. G. Davies and J.E. Ffowcs Williams. Aerodynamic sound generation in a pipe. *Journal of Fluid Mechanics*, 765-778:14, 1968.

[12] D. Davis and E. Patronis Jr. *Sound system engineering (Third edition)*. Focal Press, Burlington, MA, 2006.

[13] F. Durst and A. B. Wang. Experimental and numerical investigations of the axisymmetric, turbulent pipe flow over a wall-mounted thin obstacle. *Procddings of 7th Symposium on Turbulenct Shear Flows*, pages 0.4.1–10.4.6, 1989.

[14] S. Feng, F. Atsushi, T. Tatsuya, and T. Yoshiyuki. Particle image velocimetry measurements of flow field behind a circular square-edged orifice in a round pipe. *Experiments in Fluids*, 54(6):1–18, 2013.

[15] X. Gloerfelt and P. Lafon. Direct computation of the noise induced by a turbulent flow through a diaphragm in a duct at low mach number. *Computers and Fluids*, 37(4):388–401, 2008.

[16] M. Goldstein. Aeroacoustics. *McGraw-Hill*, New York, 1976.

[17] C. G. Gordon. Spoiler generated flow noise. i. the experiment. *Journal of the Acoustical Society of America*, 43(5):1041–1048, 1968.

[18] C. G. Gordon. Spoiler generated flow noise. ii. results. *Journal of the Acoustical Society of America*, 45(1):214–223, 1969.

[19] N. Han, X. J. Qiu, and C. M. Mak. A further study of the prediction method for aerodynamic sound produced by two in-duct elements. *Journal of Sound and Vibration*, 294(12):374–380, 2006.

[20] Health and Safety. The control of noise at work regulations. *The Stationery Office Limited*, 2005.

[21] H. H. Heller and S. E. Widnall. Sound radiation from rigid flow spoilers correlated with fluctuating forces. *The Journal of the Acoustical Society of America*, 47(3B): 924–936, 1970.

[22] F. V. Herpe and D. Crighton. Noise generation by turbulent flow in ducts. *Journal de Physique IV Colloque*, 04(C5):C5–947–C5–950, 1994.

[23] K. R. Holland and P. O. A. L. Davies. The measurement of sound power flux in flow ducts. *Journal of Sound and Vibration*, 230(4):915–932, 2000.

[24] J. Holmgren. Restricor noise in ventilation systems-method for calculating sound power level. *Airbus internal presentation.*

[25] F. Hsiao, Y. Lim, and J. Huang. On evolution of flow structure and vortex dynamics for right-angle and sharp-edged orifice plane jet. *Transactions of the Janpan Society for Aeronautical and Space Sciences*, 53(182):296–306, 2011.

[26] Verein Deutscher Ingenieure. Vdi 2081: Noise generation and noise reduction in air-conditioning systems. 2007.

[27] P. Joseph, C. L. Morfey, and C. R. Lowis. Multi-mode sound transmission in ducts with flow. *Journal of Sound and Vibration*, 264(3):523–544, 2003.

[28] U. Karban, K. Kucukcoskun, G. Ogus, C. Schram, C. Sovardi, and W. Polifke. Noise produced by a tandem diaphragm experimental and numerical investigation. *20th AIAA/CEAS Aeroacoustics Conference*, AIAA 2014-3225, 2014.

[29] E. J. Kerschen and J. P. Johnston. Mode selective transfer of energy from sound propagating inside circular pipes to pipe wall vibration. *The Journal of the Acoustical Society of America*, 67(6):1931–1934, 1980.

[30] E. J. Kerschen and J. P. Johnston. A modal separation measurement technique for broadband noise propagating inside circular ducts. *Journal of Sound and Vibration*, 76(4):499–515, 1981.

[31] E. J. Kerschen and J. P. Johnston. Modal content of noise generated by a coaxial jet in a pipe. *Journal of Sound and Vibration*, 76(1):95–115, 1981.

[32] A. Kierkegaard, S. Allam, G. Efraimsson, and M. Abom. Simulations of whistling and the whistling potentiality of an in-duct orifice with linear aeroacoustics. *Journal of Sound and Vibration*, 331:1084–1096, 2012.

[33] O. Krekull, G. Efraimsson, and M. bom. Prediction model of flow duct constriction noise. *Applied Acoustics*, 82:45–52, 2014.

[34] O. Krekull, G. Efraimsson, and M. bom. Revisiting the nelsonmorfey scaling law for flow noise from duct constrictions. *Journal of Sound and Vibration*, 357:233–244, 2015.

[35] R. Lacombe, S. Foller, G. Jasor, W. Polifke, Y. Auregan, and P. Moussou. Numerical investigations on the whistling ability of a single hole orifice in a flow duct. *10eme Congres Francais d'Acoustique*, 2010.

[36] M. J. Lighthill. On sound generated aerodynamically, i. general theory. *Proceeding of Royal Society, London.Series A.*, 211:564–587, 1952.

[37] C. M. Mak. Development of a prediction method for flow-generated noise produced by duct elements in ventilation systems. *Applied Acoustics*, 63(1):81–93, 2002.

[38] C. M. Mak and W. M. Au. A turbulence-based prediction technique for flow-generated noise produced by in-duct elements in a ventilation system. *Applied Acoustics*, 70(1):11–20, 2009.

[39] C. M. Mak and J. Yang. A prediction method for aerodynamic sound produced by closely spaced elements in air ducts. *Journal of Sound and Vibration*, 229(3): 743–753, 2002.

[40] F. Mathey, O. Morin, B. Caruelle, and K. Debatin. Simulation of aero-acoustic sources in aircraft climate control systems. *12th AIAA/CEAS Aeroacoustics Conference*, AIAA 2006-2493, 2006.

[41] F. Mendonca, A. Read, S. Caro, K. Debatin, and B. Caruelle. Aeroacoustic simulation of double diaphragm orifices in an aircraft climate control system. 2005.

[42] C. L. Morfey. Rotating pressure patterns in ducts: Their generation and transmission. *Journal of Sound and Vibration*, 1(1):60–87, 1964.

[43] C. L. Morfey. Sound transmission and generation in ducts with flow. *Journal of Sound and Vibration*, 14(1):37–55, 1971.

[44] G. L. Morrison, R. E. Deotte, G. H. Nail, and D. L. Panak. Mean velocity and turbulence fields inside a =0.50 orifice flowmeter. *AIChE Journal*, 39(5):745–756, 1993.

[45] B. R. Munson, D. F. Young, and T. H. Okiishi. *Fundamentals of fluid mechanics (Third edition)*. Wiley, New York, 1990.

[46] G. H. Nail. A study of 3-dimensional flow through orifice meters. *PhD Thesis, Texas A& M University*, 1991.

[47] P. A. Nelson and C. L. Morfey. Aerodynamic sound production in low speed flow ducts. *Journal of Sound and Vibration*, 79(2):263–289, 1981.

[48] D. J. Oldham and A. U. Ukpoho. A pressure-based technique for predicting regenerated noise levels in ventilation systems. *Journal of Sound and Vibration*, 140(2): 259–272, 1990.

[49] D. J. Oldham and D. C. Waddington. The prediction of airflow-generated noise in ducts from considerations of similarity. *Journal of Sound and Vibration*, 248(4): 780–787, 2001.

[50] H. K. Ozcan and S. Nemlioglu. In-cabin noise levels during commercial aircraft flights. *Journal of the Canadian Acoustic Association*, 34(4):31–35, 2006.

[51] S. Pennig, J. Quehl, and V. Rolny. Effects of aircraft cabin noise on passenger comfort. *Ergonomics*, 55(10):1252–1265, 2012.

[52] G. Reethof. Turbulence-generated noise in pipe flow. *Annual Review of Fluid Mechanics*, 10:333–367, 1978.

[53] H. S. Ribner. The generation of sound by turbulent jets. *Advances in Applied Mechanics*, 8:103–182, 1964.

[54] E. J. Rice. Multimodal far-field acoustic radiation pattern using mode cutoff ratio. *AIAA Journal*, 16(9):906–911, 1978.

[55] S. Sadhra and C. A. Jackson. Noise exposure and hearing loss among student employees working in university entertainment venues. *The Annals of Occupational Hygiene*, 46(5):455–463, 2002.

[56] A. Sengissen, B. Caruelle, and P. Souchotte. Les of noise induced by flow through a double diaphragm system. *15th AIAA/CEAS Aeroacoustics Conference*, AIAA 2009-3357, 2009.

[57] T. Spangenberg. Numerical and experimental analysis of the turbulence and the noise generated by flow through restrictors in an aircraft cabin air distribution system. page Thesis of Master degree, 2012.

[58] F. Tao, X. Zhang, P. Joseph, O. Stalnov, M. Siercke, and H. Scheel. Experimental study of the mechanisms of sound generation due to an in-duct orifice plate. *21st AIAA/CEAS Aeroacoustics Conference*, AIAA 2015-2231, 2015.

[59] P. Testud, Y. Auregan, P. Moussou, and A. Hirschberg. The whistling potentiality of an orifice in a confined flow using anenergeticcriterion. *Journal of Sound and Vibration*, 325:769–780, 2009.

[60] D. J. Ukpoho and D. J. Oldham. Regenerated noise levels due to closely apaced duct elements. *Proceedings of insitite of acoustics*, 13:461–468, 1991.

[61] D. C. Waddington and D. J. Oldham. Generalized flow noise prediction curves for air duct elements. *Journal of Sound and Vibration*, 222(1):163–169, 1999.

[62] J. F. Wilby. Aircraft interior noise. *Journal of Sound and Vibration*, 190(3):545–564, 1996.